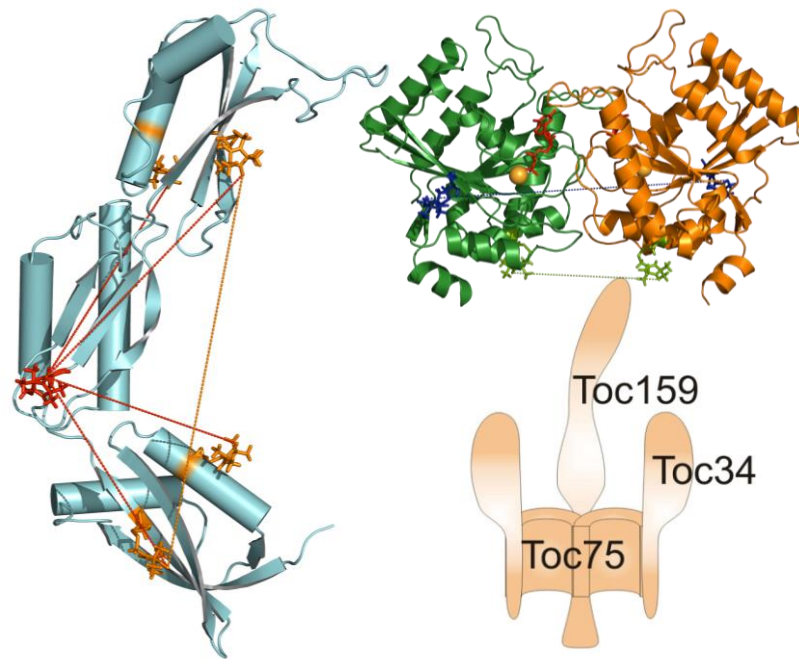# PULSED EPR CHARACTERIZATION OF
MEMBRANE TRANSPORT PROTEIN COMPLEXES

Dissertation

for attaining the PhD degree

of Natural Sciences

Submitted to the Department 14

of the Johann Wolfgang Goethe University

in Frankfurt am Main

by

Reza Dastvan

from Bandar-Abbas, Iran

Frankfurt am Main 2012

(D30)

Accepted by the Department 14: Biochemistry, Chemistry and Pharmacy
of the Johann Wolfgang Goethe University as a dissertation.

Dean: Prof. Dr. Thomas F. Prisner

Expert assessors: Prof. Dr. Thomas F. Prisner
                             Prof. Dr. Clemens Glaubitz

Date of the disputation: …………………………...

This thesis is dedicated to my parents
who have always encouraged me to pursue my dreams
and my wife Khadijeh
for her endless love and support.

Table of Contents

Abstract

Pulsed electron–electron double resonance (PELDOR) spectroscopy is a powerful tool for measuring nanometer distances in spin-labeled systems and recently is increasingly applied to membrane proteins. However, after reconstitution of labeled proteins into liposomes, spin labels often exhibit a much faster transversal relaxation (T_m) than in detergent micelles, thus limiting application of the method in lipid bilayers. In the first part of the thesis, optimization of transversal relaxation in phospholipid membranes was systematically investigated by use of spin-labeled derivatives of stearic acid and phosphatidylcholine as well as spin-labeled derivatives of the channel-forming peptide gramicidin A under the conditions typically employed for PELDOR distance measurements. Our results clearly show that dephasing due to instantaneous diffusion that depends on dipolar interaction among electron spins is an important contributor to the fast echo decay in cases of high local concentrations of spin labels in membranes. The main difference between spin labels in detergent micelles and membranes is their local concentration. Consequently, avoiding spin aggregation and suppressing instantaneous diffusion is the key step for maximizing PELDOR sensitivity in lipid membranes. Even though proton spin diffusion is an important relaxation mechanism, only in samples with low local concentrations does deuteration of acyl chains and buffer significantly prolong T_m. In these cases, values of up to 7 μs have been achieved. Furthermore, our study revealed that membrane composition and labeling position in the membrane can also affect T_m, either by promoting the segregation of spin-labeled species or by altering their exposure to matrix protons. Effects of other experimental parameters including temperature (<50 K), presence of oxygen, and cryoprotectant type are negligible under our experimental conditions.

In the second part of the thesis, inhomogeneous distribution of spin-labels in detergent micelles has been studied. A common approach in PELDOR is measuring the distance between two covalently attached spin labels in a macromolecule or singly-labeled components of an oligomer. This situation has been described as a spin-cluster. The PELDOR signal, however, does not only contain the desired dipolar coupling between the spin-labels of the molecule or cluster under study. In samples of finite concentration the dipolar coupling between the spin-labels of the randomly distributed molecules or spin-clusters also contributes

significantly. In homogeneous frozen solutions or lipid vesicle membranes this second contribution can be considered to be an exponential or stretched exponential decay, respectively. In this study, it is shown that this assumption is not valid in detergent micelles. Spin-labeled fatty acids that are randomly partitioned into different detergent micelles give rise to PELDOR time traces which clearly deviate from stretched exponential decays. As a main conclusion a PELDOR signal deviating from a stretched exponential decay does not necessarily prove the observation of specific distance information on the molecule or cluster. These results are important for the interpretation of PELDOR experiments on membrane proteins or lipophilic peptides solubilized in detergent micelles or small vesicles, which often do not show pronounced dipolar oscillations in their time traces.

In the third part, PELDOR has been utilized to study the structural flexibility of the Toc34 GTPase homodimer, a preprotein receptor of the translocon of the outer envelope of chloroplasts (TOC). Toc34 belongs to GAD subfamily of G-proteins that are regulated and activated by nucleotide-dependent dimerization. However, the function of Toc34 dimerization is not yet fully understood. Previous structural investigations of the Toc34 dimer yielded only marginal structural changes in response to different nucleotide loads. PELDOR revealed a nucleotide-dependent transition of the dimer flexibility from a tight GDP to a flexible GTP-loaded state. Substrate-binding stabilizes the dimer in the transition state mimicked by GDP-AlF$_x$, but induces an opening in the GDP or GTP-loaded state. Thus, the structural dynamics of *bona fide* GTPases induced by GTP hydrolysis is replaced by substrate-dependent dimer flexibility, which represents the regulatory mode for dimerizing GTPases.

In the fourth part of the thesis, conformational flexibility and relative orientation of the N-terminal POTRA domains of a cyanobacterial Omp85 from *Anabaena sp.* PCC 7120, a key component of the outer membrane protein assembly machinery, were investigated by PELDOR spectroscopy. Membrane proteins of the Omp85-TpsB superfamily are composed of a C-terminal β-barrel and a different number of N-terminal POTRA domains, three in the case of cyanobacterial Omp85. It has been suggested that the N-terminal POTRA domains (P1 and P2) might have functions in substrate recognition. Molecular dynamics (MD) simulations predicted a fixed orientation for P2 and P3 and a flexible hinge between P1 and P2. The PELDOR distances measured between the P2 and P3 POTRA domains are in good agreement with the structure determined by X-ray, and compatible with the MD simulations suggesting a fixed orientation between these domains. PELDOR constraints between the P1

and P2 POTRA domains imply a rather rigid structure with a slightly different relative orientation of these domains compared with the X-ray structure. Moreover, the large mobility predicted from MD is not observed in the frozen solution. The PELDOR results further highlight the restricted relative orientation of the POTRA domains of the Omp85-TpsB proteins as a conserved characteristic feature that might be important for the processive sliding of the unfolded substrate towards the membrane.

1. Motivation and Aim

Pulsed electron-electron double resonance (PELDOR) spectroscopy[1-4] is a well-known method for measuring long-range distances and their distribution in spin-labeled macromolecules and thus, provides valuable information on the conformational dynamics[5,6] as well as wide-range distance restraints (1.8 to 6–10 nm in deuterated samples) for structural modeling.[7-14] Therefore, this spectroscopic technique is extremely helpful for studying macromolecular complexes with regard to conformational dynamics as well as relative orientation of their components in different functional states. Therefore in a "bottom-up" approach, the goal of this study was to utilize PELDOR to study the membrane transport complexes such as chloroplast protein import and cyanobacterial outer membrane protein assembly machineries, under the conditions close to their native environments. However, the applicability of PELDOR to membrane proteins in reconstituted systems has been limited because of much shorter spin echo dephasing time (T_m) of spin labels in lipid vesicles. Therefore the main reasons for enhanced transversal relaxation in phospholipid membranes were investigated systematically.

Nonionic detergents are frequently used for solubilization of membrane proteins. Inhomogeneous distribution of spin-labeled fatty acids in these detergent micelles has also been studied. Since, size restriction effects in micelles are sufficient to obtain PELDOR time-traces which strongly deviating from stretched exponential decays. This is important for the interpretation of PELDOR experiments on membrane proteins or lipophilic peptides solubilized in micelles, which often do not show pronounced dipolar oscillations in their time traces.

From chloroplast protein import machinery, structural flexibility of the Toc34 GTPase homodimer and from cyanobacterial outer membrane protein assembly complex, conformational flexibility and relative orientation of the POTRA domains of Omp85, were investigated by PELDOR. The function of Toc34 dimerization is not yet described and X-ray structures of the Toc34 dimer in different nucleotide-loading states revealed only marginal structural changes.[15,16] The X-ray structure of the N-terminal domain of Omp85 protein from *Anabaena sp.* PCC 7120,[17] revealed three tandem POTRA domains (P1-P3). Molecular dynamics simulations predicted a fixed orientation for P2 and P3 and a flexible hinge between

4

P1 and P2.[17] Therefore as it was shown before,[10,13] studying the dynamics within the N-terminal domain of cyanobacterial Omp85 using available spectroscopic techniques such as PELDOR is crucial for evaluation of the previous structural and molecular dynamics analyses. Furthermore, long–distance constraints can be utilized to refine the available X-ray structure. Assuming the individual POTRA domain structures as rigid body will help to overcome the sparsity of distance constraints.

2. Introduction

2.1. Chloroplast Protein Import Machinery

The present section provides a short introduction into the chloroplast import machinery, mainly the TOC core-complex. For a more detailed review, books[18] and articles are recommended.[19-22]

Membrane protein complexes are usually composed of different types of membrane-associated components:

- Polytopic proteins or transmembrane proteins (TMs)
- Monotopic proteins

Transmembrane proteins span the entire biological membrane. Single-pass membrane proteins like Toc34 GTPase, cross the membrane only once, while multi-pass membrane proteins like Toc75, Tic20, and Tic110, weave in and out, crossing several times. Monotopic membrane proteins are membrane proteins that interact with only one leaflet of the lipid bilayer and do not possess transmembrane spanning segments.

According to the endosymbiont theory, present–day chloroplasts evolved through engulfment of a relative of present cyanobacteria by an early eukaryotic cell. The chloroplast progenitor was controlled by the host cell. Many of the genes found originally in the cyanobacterial genome are now present in the cell nucleus. Yet, the chloroplast keeps many of the functions found in cyanobacteria (e.g., photosynthesis, fatty acid and amino acid production). To maintain these functions, many proteins have to be transported back to the chloroplast. An import machinery drives this transport process, and this consists of translocons located in the outer and the inner envelope membranes, called TOC and TIC (Translocon of the Outer/Inner envelope membrane of Chloroplasts; Figure 1). In cyanobacteria, homologues for only a few of the protein components exist; e.g., Toc75, Tic20, Tic22 and Tic55.[23] Interestingly, the related transport system in cyanobacteria (based on a homologue of the Toc75 channel) is proposed to mediate secretion from the cell, which is opposite to the direction of transport during chloroplast import. This directionality change

might be related to the transfer of the Toc75 gene to the nucleus. The transit peptide (TP) (which is needed to bring preproteins to the chloroplast) may be derived from a secretory peptide in the endosymbiont, which was recognized and secreted by the ancestral Toc75.[24]

Interestingly, at least two different TOC/TIC import pathways exist, and it is now clear that TOC/TIC-independent or "non-canonical" protein targeting to chloroplasts also occurs. All proteins that follow the TOC/TIC path have a cleavable, N-terminal TP. This acts as a targeting signal, directing the preprotein exclusively to the chloroplast. In general, TP is enriched in hydroxylated amino acids, which in some cases can be phosphorylated by a cytosolic kinase.[22] It has been suggested that the TP can be divided into three domains: the N-terminus is mainly uncharged and proposed to play a role in recognition; the central part lacks acidic residues and mediates translocation over the envelope; finally, the C-terminus is enriched in arginines and involved in TP cleavage inside the chloroplast.[18] In the TOC/TIC pathway, the binding of the preprotein to the chloroplast outer envelope membrane (OEM) is mediated by the TP. In the absence of an energy source, binding to the import apparatus is reversible and no translocation will occur. This step may also involve interactions between the TP and the outer envelope lipids.[25] In the presence of GTP, and low concentrations of ATP (≤ 100 µM), the binding step is irreversible and an early import intermediate is formed. At this stage, the preprotein has penetrated the OEM and is in contact also with the inner envelope membrane (IEM). For complete translocation, high ATP concentrations (>100 µM) are required in the stroma, and this is thought to be consumed by stromal molecular chaperones. In addition to the essential role of the TP, the mature part of the preprotein has also been reported to influence the interaction between the preprotein and the translocon.[18]

Several hypotheses exist for the transport of nucleus-encoded proteins from the cytosol, where they are synthesized, to the chloroplast surface. One proposal involves a so-called "guidance complex" which brings the preprotein to the TOC components. A second hypothesis involves contact with OEM lipids, which might induce changes in the bilayer to facilitate contact with a nearby TOC complex.[25] Another possibility is direct interaction with the TOC complex, mediated by membrane-associated receptors (Toc34 or Toc159).[20,22] A variation on the latter involves a soluble form of Toc159, which first recognizes the preprotein in the cytosol and, like the guidance complex, brings the preprotein to the TOC machinery.[26] Finally, a putative third TOC component, Toc64, has been suggested to act as a receptor for a subset of proteins pre-bound by Hsp90; however, the relevance of this idea is debated (Figure 1).[18]
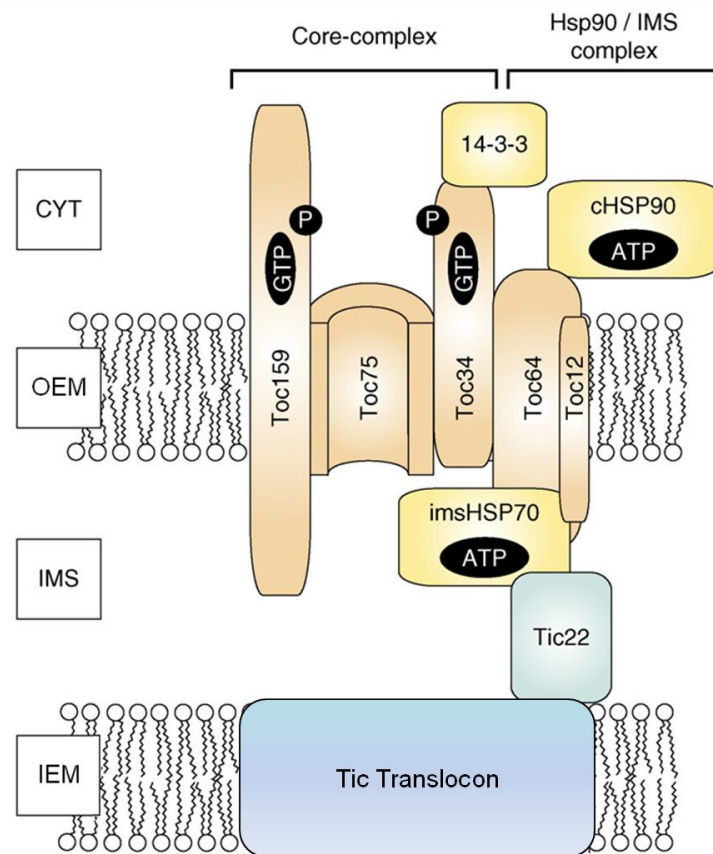
Figure 1. Translocon of the outer envelope of chloroplast; Translocation of precursor proteins across the outer membrane depends on chaperones (yellow), proteins in the outer envelope membrane (orange), the inner envelope membrane (blue) and stroma (not shown). Nucleotide requirements are indicated. The outer membrane localized complex can be divided into a "core complex" composed of Toc159, Tocc34 – which are regulated by phosphorylation – and Toc75. Toc64 and Toc12 form a complex involved in perception of Hsp90 delivered precursor proteins and, together with Tic22 and the intermembrane space localized Hsp70, in the assembly of an intermembrane space (IMS) complex for the transfer across the intermembrane space. The model represents a scheme of participating components not considering stoichiometric relations or organ specific distributions.[20]

The Toc34 and Toc159 components are related GTPases. GTP-binding or G-proteins are molecular switches for the regulation of numerous cellular processes.[27] They serve as transducers of information by their ability to hydrolyze guanosine triphosphate (GTP) and therewith to switch between a GTP-and guanosine diphosphate (GDP-) bound state, which is sensed by G-protein specific effectors.[28] The nucleotide change of *bona fide* GTPases is generally controlled by GTPase-activating proteins (GAPs) and GDP/GTP exchange factors (GEFs).[29,30] GAPs complement or stabilize the catalytic center of the GTPase, thereby

increasing GTP-hydrolysis several orders of magnitude. GEFs promote nucleotide exchange by reducing the nucleotide affinity. In some cases nucleotide release is regulated by GDP dissociation inhibitors (GDIs) and GDI displacement factors (GDFs).[31] The provoked structural change between GTP and GDP state assures high affinity interactions with effectors in the GTP form, in which two dynamic structural elements binding the γ phosphate of the GTP, assigned as switch I and switch II, relax after GTP hydrolysis and release of the anorganic phosphate (Pi).[30] Based on their structural and functional properties, G-proteins have been recently classified according to their mode of function.[28,32] One of the proposed subgroups unifies the G-proteins activated by nucleotide-dependent dimerization (GADs), which are able to form (*pseudo*)homodimers.[28] They reciprocally complement their catalytic sites in the dimeric state, rendering the presence of a classical GAP unnecessary.[28] The high nucleotide exchange rate as consequence of their low nucleotide affinity makes them independent of GEFs as well. GADs are involved in numerous fundamental cellular functions.[27] Important examples are membrane fusion and fission factors like atlastin, dynamin and septin, the conserved tRNA-modifying protein MnmE, the GTPase Xab1, being involved in DNA repair and the signal recognition particle (SRP) and its receptor (SRP receptor, SR),[33] the latter belonging to the Signal recognition GTPases and the MinD and BioD (SIMIBI) superclass. Current knowledge suggests, that both, GTPase and biological reaction, are sometimes stimulated by additional co-GAPs.[27,28] Nevertheless, GADs seem to possess all structural elements for the canonical switch mechanism of *bona fide* G-proteins.[27]

Toc34

A further example of a GAD is Toc34, a member of the Translation Factor-(TRAFAC) related class[34] being closely related to the septin GTPases.[35] So far, only one Toc34 isoform has been identified in pea *(Pisum sativum Toc34, or psToc34)*, but two homologues exist in *Arabidopsis thaliana* (*at*Toc33 and *at*Toc34); both *Arabidopsis* proteins are very similar to *ps*Toc34 (~60% identity). Toc34 consists of a cytosolic GTPase (G) domain and a short, membrane-spanning helix at the C-terminal end (Figure 1). It was thought that binding of GTP is necessary for Toc34 to receive incoming preproteins, and for it to act as a receptor.[36,37] According to one model for preprotein recognition, the structure of Toc34 changes upon GTP hydrolysis and the preprotein is released towards Toc159 and the Toc75 channel. In another model, Toc34 functions as a receptor for an incoming preprotein–Toc 159 complex.

X-ray structures of *ps*Toc34 in the GDP- and GMPPNP-bound state showed that the receptor can dimerize (Figure 2).[15,16] Homodimerization of Toc34 is considered to be important as plants with a Toc34 mutant with reduced homodimerization show reduced import efficiency.[38] The dimerization interface covers the nucleotide-binding site.[15,16,39-41] It was assumed that dimerization provides a reciprocal "GAP" function, as an invariant arginine residue reaches from one protomer into the catalytic center of the other in the position of the β-phosphate of the nucleotides[15] alike the arginine finger of Ras/Rho GAPs.[42] Contradicting, GTP hydrolysis is not accelerated upon homodimer formation and thus, the need for further <u>G</u>TPase <u>c</u>o-<u>r</u>egulators (GCRs) or co-GAPs has been postulated.[39] This GCR should complement the catalytic site to position a water molecule for the nucleophilic attack on the γ-phosphate for GTP hydrolysis.[39] Moreover, these crystal structures did not reveal the expected typical molecular switch thought to be required for G proteins. Because Toc34 and Toc159 share significant homology within their G-domains, it has been suggested that both receptors dimerize, and, even more interestingly, that heterodimerization may be an important component of the import mechanism (Figure 2).[43-46] Assembly of the TOC translocon, as well as precursor transport, is also suggested to be dependent on heterodimerization.[47] However, the consequences of homo-and heterodimer formation for the function and the GTPase cycle of TOC remain elusive.[48] Interestingly, *at*Toc33 was found to have unusual properties, exhibiting affinity for both GTP and XTP in its wild-type state.[49]

The function of Toc34 can be controlled by receptor phosphorylation (Figure 2).[50] It has been shown that phosphorylation serves as an inhibitor for the association of Toc34 with other components of the complex. However, it is difficult to understand why the regulation of two orthologues (*ps*Toc34 and *at*Toc33) might be mediated by phosphorylation at very different positions (S113 in *ps*Toc34 and S181 in *at*Toc33, both of which lack conservation in other species), and, presumably, through completely different mechanisms. The function of Toc34 in preprotein recognition is widely accepted, but whether Toc34 or Toc159 is the primary receptor for the preprotein is debated (Figure 2). Two models have been proposed: the "motor model" places Toc34 in this role, while the "targeting model" has Toc159 as the primary receptor.[19] Evidence arguing for Toc34 as the primary receptor includes: preprotein interaction with Toc34 *in vitro*[51-53]; greater quantities of Toc34 (versus Toc159) in the envelope membrane[54]; proposed interaction with the guidance complex; and, the lack of direct input from Toc34 during translocation over the membrane.[55] Whether or not Toc34 is
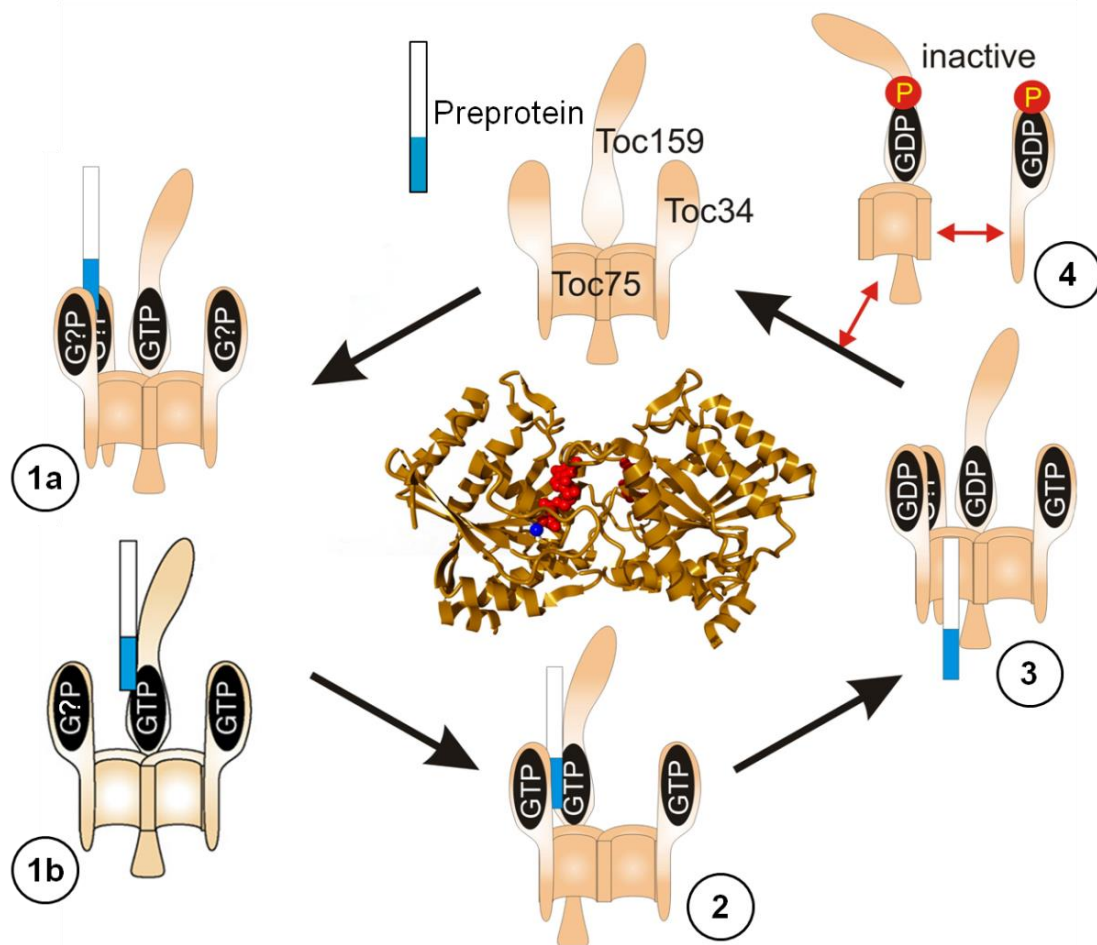
Figure 2. The regulation of the Toc-complex; the isolated Toc complex is composed of four Toc75, four (to five) Toc34 and one Toc159. For simplicity, only half of the translocon is shown. Preproteins (white bar, transit sequence shown in blue) might be recognized by either Toc34 (step 1a) or Toc159 (step 1b). In a GTP-dependent manner the protein is handed over to the main import receptor Toc159 (step 2), which subsequently facilitates the insertion of the protein into Toc75-channel (step 3). By GTP to GDP exchange, the complex is regenerated for a new import cycle (top). Phosphorylation of either Toc34 or Toc159 impedes the complex by dissociation of Toc34 (step 4). The complex can be reactivated by dephosphorylation of Toc34. Center: crystal structure of the Toc34 GTPase domain.[16,20]

the primary receptor, it seems that different Toc34 isoforms have specific preferences for certain preproteins. Proteomic studies on an *at*Toc33 null mutant, named *ppi1* (*plastid protein import 1*), showed that photosynthetic proteins are specifically deficient in the mutant, whereas non-photosynthetic, housekeeping proteins are rather stable. The same is true for an *at*Toc159 mutant, termed *ppi2*,[56] and so import into *Arabidopsis* chloroplasts is proposed to follow two different pathways: *at*Toc33 and *at*Toc159 preferentially import photosynthetic proteins; *at*Toc34 and *at*Toc132/*at*Toc120 import housekeeping proteins. Nevertheless, "cross-talk" between the pathways seems to occur. Multiple Toc34 isoforms also exist in

moss (*Physcomitrella patens*), maize and spinach, and in the latter case evidence suggests that the isoforms exhibit functional specialization.[18,57]

Toc159

Initially, Toc159 was observed as a fragment of 86 kDa, and so the name Toc86 was used. However, due to the identification of a larger homologue in *Arabidopsis*, the pea Toc86 protein was further examined and shown to have a native size comparable to the *Arabidopsis* protein. The Toc159 family consists of four members in *Arabidopsis* − *at*Toc159, *at*Toc132, *at*Toc120 and *at*Toc90 − while in pea currently only psToc159 (formerly Toc86) has been identified.[18] The *ps*Toc159 protein is most similar to *at*Toc159 (48% identity), and so these two are believed to be functional orthologues.[56] Toc159 proteins have three domains: an N-terminal acidic (A) domain which is very sensitive to proteolysis, giving rise to the 86-kDa fragment[58-60]; a central GTPase (G) domain related to the Toc34 G-domain; and, a hydrophilic M-domain that anchors *at*Toc159 in the membrane.[61] The M-domain is a 52-kDa protease-resistant region that does not carry typical hydrophobic, transmembrane helices, and so is unusual.[56,58,60] In the "targeting model" of preprotein recognition, Toc159 acts as the primary receptor (Figure 2). Detection of an abundant form of *at*Tocl59 in the cytosol gave this model another dimension.[26] It was proposed that Toc159 recognizes the preprotein in the cytosol, and then brings it to the TOC complex; in fact, soluble Toc159 was shown to interact exclusively with the TP of preproteins. This implies that Toc159 cycles between its soluble, cytosolic form and its membrane-integrated form. The atypical hydrophilic M-domain of Toc159 may play a critical role in this integration/de-integration process. However, the significance of cytosolic Toc159 has been questioned, and attributed to partial disruption of membranes due to the experimental procedures.[52] The "targeting model" is comparable to the co-translational translocation of proteins into the ER by the signal recognition particle (SRP) system, The latter starts with recognition of a nascent signal peptide, protruding from a ribosome, by the SRP (a GAD GTPase). This complex carries the preprotein to the SR (another GTPase) where GTP hydrolysis ensures preprotein transfer to the Sec translocase for transport over the membrane.[33] Toc159 is proposed to play a role analogous to that of SRP, while Toc34 may be analogous to the SRP-receptor. Interestingly, a distant homology between TOC GTPases and chloroplastic SRP and SRP-receptors has been proposed.[62] The Toc34 protein is believed to mediate the insertion of Toc159 in a GTPase−regulated

fashion.[47] Hence, the initial binding to the membrane could occur by a heterodimerization between Toc34 and Toc159, both in the GTP state.

In the "motor model", where Toc34 is assumed as the primary receptor, Toc159 is permanently associated with the membrane and acts as a motor by driving the preprotein forward through the Toc75 channel (Figure 2). The Toc159 motor action is powered by multiple cycles of GTP hydrolysis, each one pushing a new part of the preprotein into the channel.[52,55] The model is based on several lines of evidence. Firstly, a minimal TOC complex consisting of a Toc159 fragment and Toc75 was able to mediate transport of preproteins into proteoliposomes at the expense of GTP hydrolysis. Secondly, in isolated TOC core-complexes (whose stoichiometry was estimated to be 4:4:1 for Toc34:Toc75:Toc159), Toc34 and Toc75 were found in almost equal amounts. Also, crosslinking studies revealed that Toc159 is in close association with the preprotein throughout OEM translocation. Studies using proteoliposomes containing the TOC core-complex showed that precursor binding could only be inhibited when Toc34 was blocked using a competitive TP fragment; similar inhibition of Toc159 did not interfere with binding.[52] This again supported the proposed role of Toc34 as the primary receptor. Recently it has been demonstrated that the homodimeric state of atToc33 displays the inactive ground state of the receptor, which opens after preprotein binding.[63] This is believed to be a prerequisite for Toc33/Toc159 heterodimer formation, leading to activation of the GTPases and a passing over of the preprotein to atToc75-III (Figure 2).[48] In this model, Toc159 remains in close association with Toc75 via an interaction that is nucleotide-insensitive.[52] Following GTP hydrolysis, the association of Toc34 with the TOC complex is weakened. Further experimentation is required to determine which elements of the "targeting" and "motor" models most closely reflect the *in vivo* situation.

Following recognition, preproteins are transferred to the OEM channel, of which Toc75 is the main component. Following OEM translocation, preproteins enter the intermembrane space (IMS) prior to their association with the IEM. Contact sites between the OEM and the IEM are established to enable efficient translocation from TOC to TIC.[64] Several components, including Toc12, an IMS Hsp70 and Tic22, are proposed to facilitate translocation across the IMS (Figure 1). On arrival at the IEM, the preprotein may contact Tic110 and/or Tic20, since both have been proposed to mediate channel formation in the IEM.

Toc75

Toc75, a member of Omp85 protein family, is one of the most abundant proteins in the OEM, and can act as an aqueous ion channel in vitro, strongly suggesting that it forms the translocation pore (Figure 1). All members of this family exhibit a characteristic N-terminal polypeptide–transport–associated (POTRA) and a C-terminal 16-stranded β-barrel domain.[54] The channel is estimated to be ~14Å in diameter, which is sufficient only for largely unfolded proteins to pass. However, a degree of elasticity has been observed in the import of a tightly folded substrate with ~23Å in diameter.[18] Interestingly, *ps*Toc75 shares 22% amino acid sequence identity with a cyanobacterial (*Synechocystis*) homologue, SynToc75.[24] This homologue behaves as a channel protein with features similar to those of *ps*Toc75. In pea, a second Toc75-related protein was identified on the basis of its similarity to *Syn*Toc75. This protein shares 31% identity with *ps*Toc75, is also assumed to be a channel, and was named *ps*Toc75-V. On the basis of phylogenetic studies, *at*Toc75-V was proposed to be the most primitive form of the Toc75 channel.[65] However, this was challenged by an idea that the two pea Toc75-like proteins each derived independently from cyanobacterial sequences.[66] Using self-assembly GFP-based *in vivo* experiments and in situ topology studies by electron cryotomography, Sommer et al. (2011)[67] showed that the POTRA domains of both *at*Toc75-III and *at*Toc75-V are exposed to the cytoplasm. Thus, the cytoplasmic exposure of the POTRA domains of *at*Toc75-III introduces an additional functional domain on the cytoplasmic side of the TOC complex, where it is in close proximity to *at*Toc33. Thus, the POTRA domain might regulate the GTPase activity of the TOC receptors, because this domain provides a Toc33 binding site. This would also explain why *at*Toc33 has to be released from the complex after phosphorylation, which is thought to inactivate the receptor.[50] Alternatively or in addition, the POTRA domains with their affinity for precursor proteins could interact with the two known receptors in the perception of the targeting signal in general.[18,68]

Various evidences indicate that there is a motor activity at the OEM, and that TOC translocation is not simply driven by TIC-associated machinery. Different hypotheses exist for the mechanism of translocation through Toc75. One of these is the Toc159 "motor model", in which the receptor acts like a sewing machine to push the preprotein through the channel in cycles of GTP hydrolysis.[54] However, this model is inconsistent with data indicating that import can still proceed in the presence of non-hydrolyzable GTP analogues,

or following removal of the Toc159 G-domain.[60] The G-domain may instead function to place the M-domain of Toc159 in a position suitable for translocation; this idea is supported by the partial complementation of *ppi2* using the M-domain only.[69] Another possibility involves ATP hydrolysis and may be called the "chaperone model". Initial studies on import showed that formation of early import intermediates is ATP dependent. Moreover, an Hsp70 chaperone has been identified in the IMS in close association with the TOC complex.[59] In this model, Hsp70 acts as a molecular ratchet to ensure the unidirectional movement of the preprotein. Toc12 may also act as a co-chaperone by controlling the ATPase activity of the IMS Hsp70 (Figure 1).[44] In contrast with mitochondrial import, Hsp70 is proposed to mediate translocation over the OEM only; full transport into the stroma over the IEM seems to involve other chaperones.[18]

2.2. POTRA Domains in Outer Membrane Protein Assembly and Two-Partner Secretion Machineries

Proteins of the outer membrane protein 85–two-partner secretion B (Omp85-TpsB) superfamily are composed of a C-terminal transmembrane β-barrel and one or more N-terminal polypeptide transport-associated (POTRA) domains. The complete structure of FhaC from *Bordetella pertussis*, the TpsB family member that mediates the secretion of filamentous hemagglutinin (FHA), revealed a 16-stranded β-barrel domain with a conserved long intrinsic loop (Figure 3A).[70] The N-terminal region of Omp85-TPS proteins includes a different number of POTRA domains.[71] For instance, TPS proteins contain two POTRA domains (Figure 3A), while the number of POTRAs of the Omp85 proteins can vary between one in Sam50 up to seven POTRA domains that are predicted for the Omp85 protein of *Myxococcus xanthus* (Figure 4).[71,72] Omp85 proteins are known to catalyze insertion of β-barrel proteins into the outer membrane. Previous structural and spectroscopic studies on proteobacterial POTRA domains of FhaC and BamA from *Escherichia coli* revealed that proteobacterial POTRA domains of the Omp85 family are composed of two rigid parts (in the case of BamA comprising P1–P2 and P3–P5; Figure 3B) that are connected by a flexible linker,[10,70,73-76] whereas TPS members only have two POTRA domains without such a flexible linker.[72,77] As a result, a conformational change upon substrate recognition was proposed for the hinge region in proteobacterial Omp85 proteins.[74] The two POTRA domains of FhaC are essential for its function and they are strongly implicated in the recognition of the FHA.[78,79] *E. coli* is
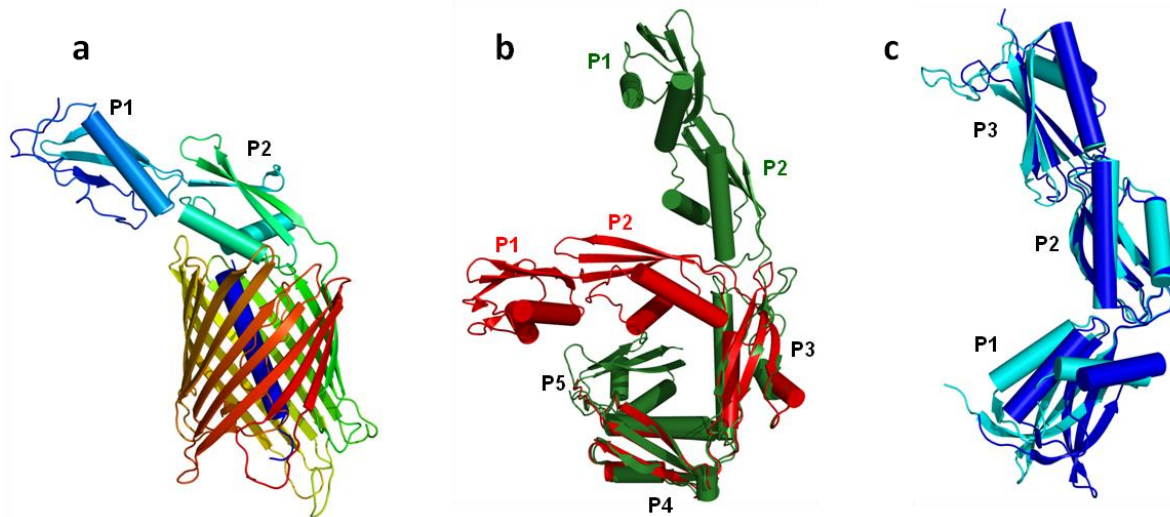
Figure 3. X-ray structures of proteo- and cyanobacterial POTRA domains; (*a*) FhaC from *Bordetella pertussis* (PDB code 2qdz); (*b*) POTRA domains of BamA from *E. coli*, "extended" (green; PDB codes 3efc,3og5) and "bent" (red; PDB code 2qdf); (*c*) POTRA domains of Omp85 proteins from *Anabaena sp.* PCC7120 (cyan; PDB code 3mc8) and *Thermosynechococcus elongates* (blue; PDB code 2x8x); the structures are superimposed at P2.

able to tolerate deletion of P1 and/or P2 but removal of P3, P4, or P5 is lethal even in the presence of P1 and P2. Therefore the minimal BamA is P3–P5 plus the C-terminal membrane domain.[77]

Cyanobacterial and plastidic Omp85 proteins like Toc75 (section 2.1) only contain three POTRA domains (Figure 3C). The structure of the cyanobacterial POTRA domains has been solved for Omp85 proteins from *Anabaena sp.* PCC7120[17] and *Thermosynechococcus elongatus*[71] (Figure 3C). N-terminal POTRA domains (P1 and P2) of *Anabaena* Omp85 might have functions in substrate recognition.[17] In addition to the proposed receptor or chaperone function, the N-terminal domain of *Anabaena* Omp85 was found to be important for the self-assembly into membranes; since full-length *Anabaena* Omp85 forms complexes with a putative trimeric structure but the C-terminal pore-forming domain only forms dimeric complexes.[68,80] Homodimerization of the isolated N-terminal region was also reported. In addition, almost all cyanobacterial Omp85 proteins have a proline-rich (10–40%) region of variable length (residues 145–219 of Omp85 from *Anabaena sp.* PCC7120) downstream of the first POTRA domain (Figure 4).[71] Furthermore, complex assembly does not induce a cooperative gating of the cyanobacterial and proteobacterial channel. This finding supports a chaperone-type function for the insertion of Omps into the outer membrane.[80] Proteo- and

cyanobacterial POTRA domains are also required for the association with other complex components.[68,73]
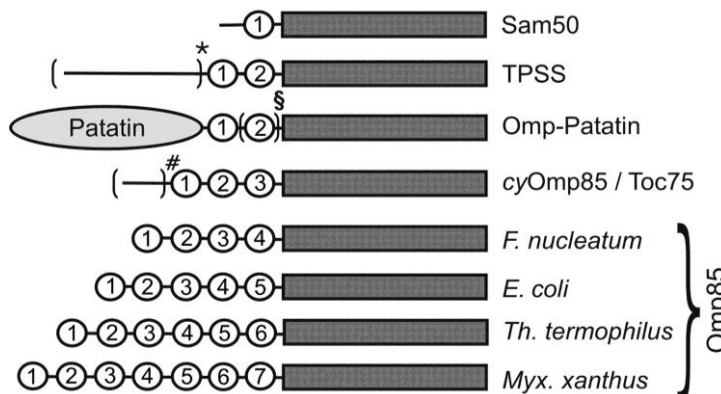
Figure 4. Diversity in the number of POTRA domains; POTRA domains are represented by *open circles* and are numbered starting from the N terminus; *β*-barrel domains are illustrated by a *dark gray box*; #, proline-rich region at the N-terminal of the POTRA domains of cyanobacterial Omp85s.[71]

2.3. EPR and PELDOR Theory

This section provides a short introduction into the theoretical background of EPR and PELDOR spectroscopy. For a more detailed description standard text books[81,82] and influential articles are recommended.[1,2,83,84]

2.3.1. Spin Hamiltonian

Unpaired electrons possess a magnetic moment $\boldsymbol{\mu}_e$. The corresponding operator is described by eq. 1.

$$\hat{\boldsymbol{\mu}}_e = -\beta_e g_e \hat{\mathbf{S}}$$

(eq. 1)

with β_e being the Bohr magneton, g_e the free electron *g*-factor and $\hat{\mathbf{S}}$ the electron spin vector operator. For unpaired electrons in molecules g_e is replaced by the **g**-tensor, taking the orientational dependence of the *g*-value into account.

A nucleus with the spin I has the magnetic moment $\boldsymbol{\mu}_n$, its corresponding operator being described by eq. 2.

$$\hat{\boldsymbol{\mu}}_n = \beta_n g_n \hat{\mathbf{I}} \qquad \text{(eq. 2)}$$

where β_n is the nuclear magneton, g_n the nuclear g-value, and $\hat{\mathbf{I}}$ the nuclear spin vector operator.

The energies of states within the ground state of a paramagnetic species with an effective electron spin S and i nuclei with spins I can be described by the static spin Hamiltonian (eq. 3):

$$\begin{aligned}
\hat{H}_0 &= \hat{H}_{EZ} + \hat{H}_{NZ} + \hat{H}_{HF} + \hat{H}_{NQ} + \hat{H}_{ZFS} \\
&= \beta_e \mathbf{B}\mathbf{g}\hat{\mathbf{S}} - \beta_n \sum_i g_{n_i} \mathbf{B}\hat{\mathbf{I}}_i + \sum_i \hat{\mathbf{S}}\mathbf{A}_i\hat{\mathbf{I}}_i + \sum_i \hat{\mathbf{I}}_i\mathbf{Q}_i\hat{\mathbf{I}}_i + \hat{\mathbf{S}}\mathbf{D}\hat{\mathbf{S}}
\end{aligned} \qquad \text{(eq. 3)}$$

Here, EZ abbreviates the electron Zeeman interaction, NZ the nuclear Zeeman interactions, HF the hyperfine couplings between the electron spin and the i nuclear spins, NQ the nuclear quadrupole interactions for spins with nuclear spin quantum numbers $I > 1/2$, and ZFS the zero-field splitting for electron spins S>1/2. **A** and **Q** are the hyperfine and quadrupole coupling tensors of one nucleus respectively, and **D** the zero field splitting tensor. Nuclei-nuclei interactions are neglected and the nuclear Zeeman interaction is considered to be isotropic.

For a spin system with S = 1/2, $\hat{H}_{EZ}$ is the dominant term in the Hamiltonian at the usually applied static fields. The coupling of a nuclear spin I to the external field **B** is described by the nuclear Zeeman interaction. In most EPR experiments the nuclear Zeeman interaction can be considered to be isotropic and usually has little influence on the EPR spectrum.

The hyperfine interaction comprises one of the most important sources of information in EPR spectroscopy. The hyperfine term in equation 3 can be written as the sum of the isotropic or Fermi contact interaction $\hat{H}_F$ and the electron-nuclear dipole-dipole coupling $\hat{H}_{DD}$. The Fermi contact interaction is given by eq. 4. It arises from the probability of finding electron density at the nucleus for electrons in s orbitals (orbital quantum number $l = 0$). For electrons in orbitals with $l \neq 0$ (p-, d-, f- orbitals) spin density at the nucleus may be induced by

configuration interactions or spin polarization mechanisms, leading to significant isotropic hyperfine interaction.

$$\hat{H}_F = a_{iso}\hat{\mathbf{S}}\hat{\mathbf{I}}$$
$$a_{iso} = \frac{2}{3}\frac{\mu_0}{\hbar}g_e\beta_e g_n\beta_n \left|\psi_0(r=0)\right|^2$$
(eq. 4)

where a_{iso} is the isotropic hyperfine coupling constant, μ_0 the vacuum permeability, $\hbar$ the Planck constant divided by 2π, and $\left|\psi_0(r=0)\right|^2$ the electron density at the nucleus. The anisotropic electron-nuclear dipole-dipole coupling is described by

$$\hat{H}_{DD} = \frac{\mu_0}{4\pi\hbar}\left[\frac{\hat{\boldsymbol{\mu}}_e\hat{\boldsymbol{\mu}}_n}{\left|\mathbf{R}\right|^3} - \frac{3(\hat{\boldsymbol{\mu}}_e\mathbf{R})(\hat{\boldsymbol{\mu}}_n\mathbf{R})}{\left|\mathbf{R}\right|^5}\right]$$
(eq. 5)

$$\hat{H}_{DD} = \hat{\mathbf{S}}\mathbf{T}\hat{\mathbf{I}}$$
(eq. 6)

where $\mathbf{R}$ is the distance vector interconnecting $\boldsymbol{\mu}_e$ and $\boldsymbol{\mu}_n$, and $\mathbf{T}$ the traceless dipolar coupling tensor. This tensor can be derived from the classic interaction energy of two magnetic dipoles with magnetic moments $\boldsymbol{\mu}_e$ and $\boldsymbol{\mu}_n$.

Combining these two interactions the common expression for the hyperfine coupling tensor can be derived:

$$\mathbf{A} = a_{iso}\mathbf{1} + \mathbf{T}$$
(eq. 7)

where $\mathbf{1}$ is a (3 x 3) unit matrix. The trace of this tensor does not depend on the molecular orientation with respect to the magnetic field and gives the isotropic part of the hyperfine interaction:

$$a_{iso} = \frac{1}{3}(A_{xx} + A_{yy} + A_{zz}) = \frac{1}{3}\text{tr}(\mathbf{A})$$
(eq. 8)

The hyperfine coupling between electron and nuclear spins is not field-dependent (for an external magnetic field stronger than the hyperfine interaction) and leads to a splitting of the

EPR line. The size of this splitting depends on the electronic structure of the molecule and the molecular orientation.
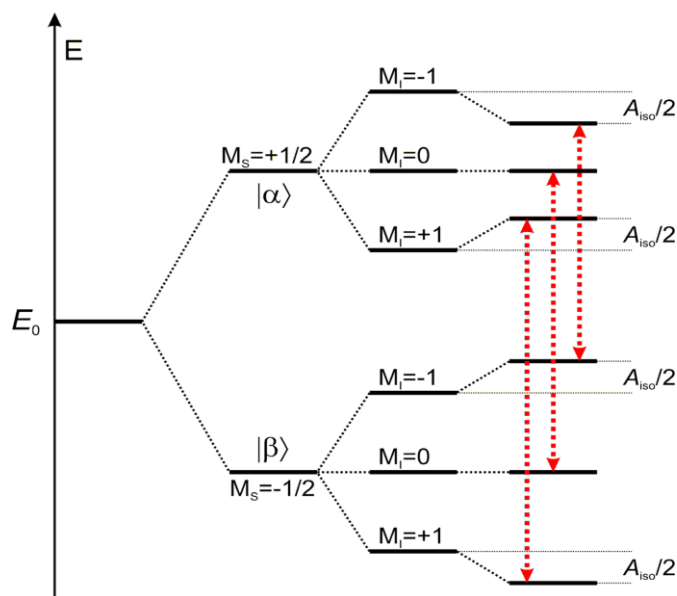
2.3.2. EPR Spectrum of a Nitroxide Radical

If the Electron Zeeman interaction is much larger compared with the hyperfine interaction and all spins, electrons and nuclei, are quantized along the direction of the magnetic field vector $\mathbf{B}_0$, taken along z (*high field approximation*), this leads to a simplified spin Hamiltonian:

$$\hat{H}_0 = g_{eff}\beta_e B_0 \hat{S}_z - g_n\beta_n B_0 \hat{I}_z + \hat{S}_z A_{eff}\hat{I}_z \qquad \text{(eq. 9)}$$

additionally neglecting the zero field splitting and the nuclear quadrupole interactions. g_{eff} and A_{eff} are orientation-dependent coupling constants. The spin operators $\hat{S}_z$ and $\hat{I}_z$ have expectation values of $M_S = -S, -S+1, ..., +S$ and $M_I = -I, -I+1, ..., +I$. The energy levels can be then described by the following expression:

$$E_{M_S,M_I} = g_{eff}\beta_e B_0 M_S - g_n\beta_n B_0 M_I + M_S A_{eff} M_I \qquad \text{(eq. 10)}$$

Figure 5. Energy level diagram for the nitroxide spin label (spin system $S = 1/2$, $I = 1$) for the case $A_{eff} = A_{iso}$.

The EPR spectrum of a nitroxide molecule at X-band frequencies (~9-10 GHz) is dominated by the hyperfine coupling to the ^{14}N nucleus of the N-O group. As ^{14}N has nuclear spin of $I = 1$, this leads to a triplet splitting of the resonance line. The energy level diagram is shown in Figure 5.

The hyperfine coupling is maximum along the direction of the p orbital on the nitrogen ($A_{zz} \sim 34$ G) and minimum in the plane perpendicular to that direction ($A_{xx} = A_{yy} \sim 6$ G). In addition, the g value is also anisotropic (Figure 6). It is maximum ($g_{xx} \sim 2.0090$) along the N-O bond, minimum along the direction of the p orbital ($g_{zz} \sim 2.0025$), and intermediate along the molecular y axis ($g_{yy} \sim 2.0060$).
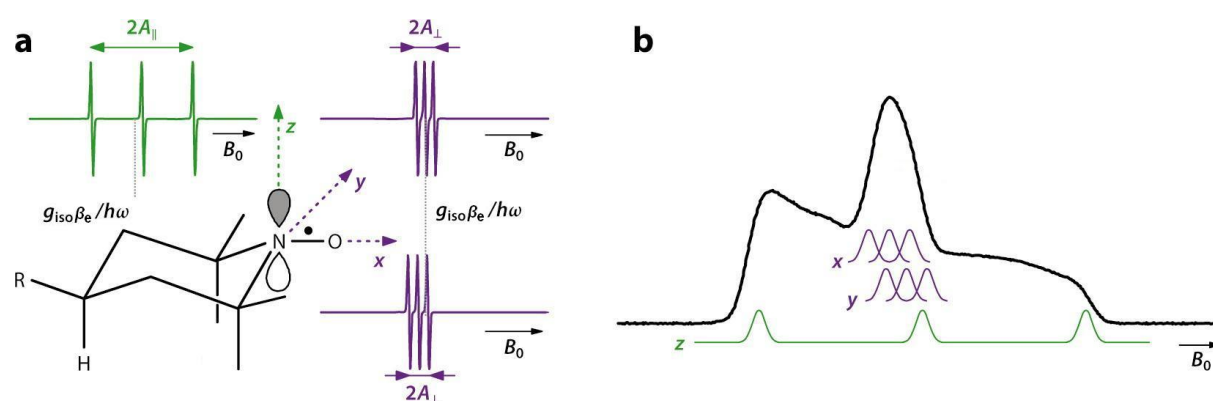

Figure 6. (*a*) Molecular frame of a nitroxide and simulated cw EPR spectra along the principal axes; (*b*) echo-detected EPR spectrum acquired at X-band in frozen solution (black, superposition of absorption spectra of all orientations). The spectrum is dominated by the large hyperfine splitting of A_{zz} (green), whereas A_{xx} and A_{yy} (purple) are not resolved.[1]

If the molecule rotates with a rate that exceeds the total spectral anisotropy of ~ 182 MHz by several orders of magnitude (rotational correlation time $\tau_r < 100$ ps, fast limit), the g- and A-tensor in equation 3 can be substituted by their averaged values $g_{iso} = (g_{xx} + g_{yy} + g_{zz})/3$ and $a_{iso} = (34+6+6)/3 \sim 15$ G, respectively. For fast rotational motion the nitroxide spectrum consists of three narrow hyperfine lines of equal intensities at the spectral positions $\left(\beta_e g_{iso} B - a_{iso}\right)/\hbar$, $\beta_e g_{iso} B/\hbar$, and $\left(\beta_e g_{iso} B + a_{iso}\right)/\hbar$ (Figure 7). If the molecule rotates with a rate that is smaller than the line width ($\tau_r > 1$ μs, $\tau_r > T_2$, where T_2 is the transversal relaxation time of the electron spin; rigid limit), the spectrum is static. It corresponds to a superposition of the spectra of all possible orientations of the molecule with respect to the magnetic field, i.e., to a powder pattern (Figure 6B).

In the intermediate regime, the lines are broadened and the rotational correlation time τ_r can be determined by simulating the line shape. In this regime, the line shapes are sensitive to details of the reorientation process and by analyzing these line shapes in detail it is possible to find out which factors influence the dynamics in a material. In the fast tumbling regime, $\tau_r < 3$ ns, rotational correlation time can be approximated from the relative intensity of the center- and high-field lines $I(0,+1)$ and the peak-to-peak linewidth $\Delta H_{pp}(0)$ of the central line (eq. 11):

$$\tau_r = 6.5 \times 10^{-10} \Delta H_{pp}(0) \left[\sqrt{\frac{I(0)}{I(+1)}} - 1 \right] \qquad \text{(eq. 11)}$$
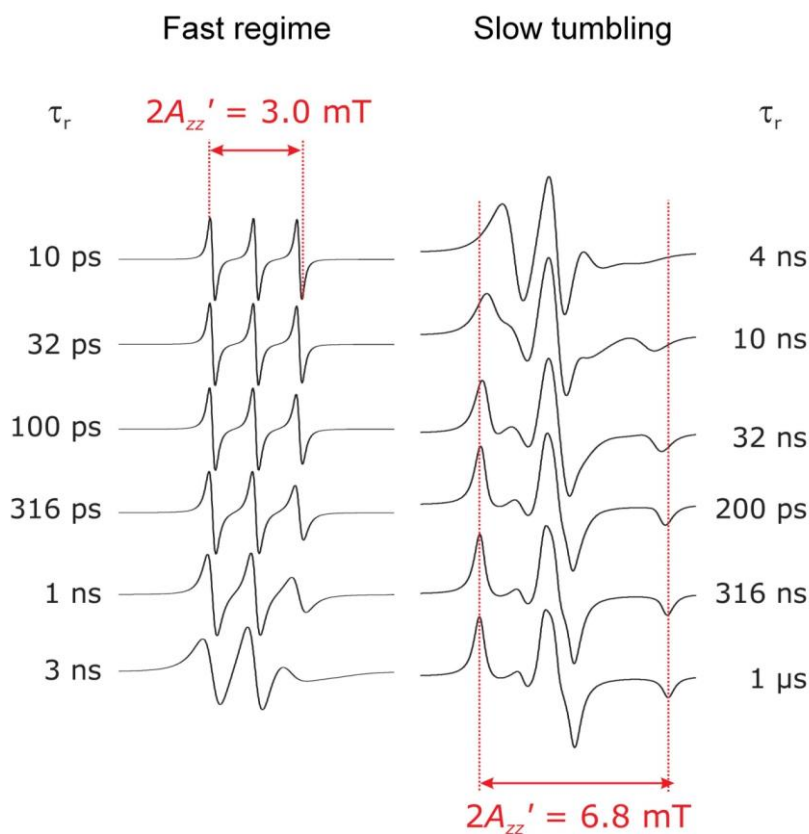
Figure 7. Dependence of nitroxide spectra on the rotational correlation time for the case of isotropic rotational diffusion. Simulation is performed by EasySpin chili.[84]

In the slow tumbling regime, $\tau_r < 3$ ns, the rotational correlation time can be determined from the total extent of the spectrum $2A_{zz}'$ normalized to the value $2A_{zz}$ in the rigid limit.

2.3.3. Electron-Electron Interactions

The main topic of this work is concerned with two weakly interacting electron spins (A and B). They are characterized by their individual spins S_A and S_B, an exchange coupling tensor $\mathbf{J}$, and a magnetic dipole-dipole coupling tensor $\mathbf{d}$. The complete Hamiltonian for such a two-spin system is given by the Hamiltonians for the individual spins and the two coupling terms

$$\hat{H}(S_A, S_B) = \hat{H}(S_A) + \hat{H}(S_B) + \hat{H}_{exch} + \hat{H}_{dd} \qquad \text{(eq. 12)}$$

The Heisenberg exchange coupling term

$$\hat{H}_{exch} = \hat{\mathbf{S}}_A \mathbf{J} \hat{\mathbf{S}}_B \qquad \text{(eq. 13)}$$

becomes relevant when the orbitals of the two spins overlap significantly, and consequently the unpaired electrons of the two species can be exchanged. In solids this can be observed if unpaired electrons are closer than about 1.5 nm or are strongly delocalized. In solution exchange can occur in biradicals, or during collisions of paramagnetic species when the orbitals overlap strongly for a short time.

The magnetic dipole-dipole coupling between two electron spins is analogous to the dipole-dipole coupling between an electron and a nuclear spin (eq. 5). The contribution to the spin Hamiltonian is given by

$$\hat{H}_{dd} = \hat{\mathbf{S}}_A \mathbf{d} \hat{\mathbf{S}}_B = \frac{\mu_0}{4\pi\hbar} \left[\frac{\hat{\boldsymbol{\mu}}_A \hat{\boldsymbol{\mu}}_B}{|\mathbf{R}|^3} - \frac{3(\hat{\boldsymbol{\mu}}_A \mathbf{R})(\hat{\boldsymbol{\mu}}_B \mathbf{R})}{|\mathbf{R}|^5} \right] \qquad \text{(eq. 14)}$$

where $\mathbf{R}$ is the distance vector interconnecting $\boldsymbol{\mu}_A$ and $\boldsymbol{\mu}_B$. We consider the electron spins as localized at the centre of the N–O bond, which is also a good approximation for distances longer than 1 nm. The dipole–dipole tensor can then be described by the point-dipole approximation. If the anisotropy of the $\mathbf{g}$ tensors can be neglected and the high-field approximation applies

$$\hat{\bar{H}}_{dd} = \omega_{dd} = 2\pi v_{dd} = -\frac{\mu_0 g_A g_B \beta_e^2}{4\pi\hbar} \frac{1}{R^3} \left(3\cos^2\theta - 1\right)$$

$$\left|\omega_\perp\right| = 2\pi\left|v_\perp\right| = \frac{\mu_0 g_A g_B \beta_e^2}{4\pi\hbar} \frac{1}{R^3}$$

(eq. 15)

where θ is the angle between the interspin vector and the external magnetic field, and R is the length of the distance vector. For $g_A = g_B = 2.0055$ this leads to

$$\left|v_\perp\right|[\text{MHz}] = \frac{52.18}{R^3[\text{nm}]}$$

$$R[\text{nm}] = \left(\frac{52.18}{\left|v_\perp\right|[\text{MHz}]}\right)^{\frac{1}{3}}$$

(eq. 16)

For molecules rotating fast compared to the inverse of dipolar coupling frequency the dipolar interaction is averaged to zero. For slowly rotating molecules or for samples of frozen solutions the spectra are a superposition of spectra of the randomly oriented biradicals, each consisting of two lines splitted by the dipolar coupling. The resulting spectrum of such a sample is called the Pake pattern. Additionally, the dipolar interaction vanishes at the "magic" angle ($\theta = 54.7^\circ$).

2.3.4. Relaxation Mechanisms of Electron Transversal Magnetization

Relaxation of electron transversal magnetization observed in Hahn echo experiments (Figure 8) arises from dipolar interaction among electron spins and the interaction of electron spins with the spins of the matrix nuclei.[85] Molecular motion of the spin label itself inducing relaxation can usually be neglected at temperatures of 50 K and below. Electron spin-spin interaction couples spins A (spins excited by microwave pulses) to the other electron spins, which are involved in a number of reorientation processes.[81] Depending on the system, the following electron spin reorientations can dominate:

(i) inversion of one electron spin with energy exchange with the lattice,
(ii) flip-flop reorientation (exchange of energy between neighboring spins with the same Zeeman energy called spin diffusion[81,85]),
(iii) instantaneous diffusion (controlled inversion of electron spins by a microwave pulse).
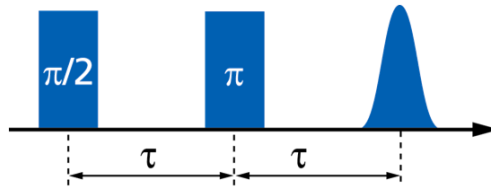
Figure 8. Two-pulse Hahn echo experiment.

Very often spins B (spins not excited by microwave pulses) are involved in the first two stochastic processes that lead to spectral diffusion (SD) due to interaction of spins A with spins B. In the instantaneous diffusion process, only the electron spins excited by pulses participate. In general, the echo intensities can be represented by a stretched exponential decay function:[85]

$$V(2\tau) = V(0) \exp\left[-\left(\frac{2\tau}{T_m}\right)^x\right] \qquad \text{(eq. 17)}$$

where $V(2\tau)$ and $V(0)$ are the echo intensity at time 2τ, twice the time between the two pulses, and echo intensity at time zero, respectively. The parameters T_m and x can be determined by fitting the experimental data (maxima of electron spin echo envelope modulation, ESEEM) with equation (17). If for instance nuclear spin diffusion is the main relaxation mechanism, $x \sim 2$–2.5 is typically found.[85,86] For processes that average inequivalent environments, such as librational motions and rotation of methyl groups, x commonly varies from ~ 2 to 0.5 as the rate of the process increases.[85] In many cases, the observed signal decays due to several processes though can be fitted with a simple exponential decay (eq. 17; $x = 1$). Then the obtained relaxation rate $1/T_m$ can be approximately considered as a sum of all contributions mentioned above:

$$\frac{1}{T_m} \approx \frac{1}{T_{ID}^{HE}} + \frac{1}{T_{SD}} + \frac{1}{T_{HF}} \qquad \text{(eq. 18)}$$

where T_{ID}^{HE} and T_{SD} are the echo dephasing times associated with instantaneous and spectral diffusion, respectively. T_{HF} describes the relaxation induced by hyperfine interactions with surrounding nuclei.

The contribution of instantaneous diffusion (ID) to the Hahn echo decay in samples with homogenous spin distribution is given by eq. 19:[81]

$$\frac{1}{T_{ID}^{HE}} = \frac{\pi \mu_0 g_A g_B \beta_e^2}{9\sqrt{3}\hbar} C\lambda \qquad (\text{eq. } 19)$$

$$\lambda = \int \sin^2\left(\frac{\beta(\Omega_S)}{2}\right) f(\Omega_S) d\Omega_S \qquad (\text{eq. } 20)$$

where $g_{A,B}$ are the effective values of the g-tensors of the spins, C is the concentration, (Ω_S) is the resonance offset, $f(\Omega_S)$ is the function describing the EPR lineshape, and $\beta(\Omega_S)$ is the flip-angle of the second pulse in a Hahn echo sequence in dependence of the resonance offset. By solving the Bloch equations for longitudinal magnetization (M_z) after a microwave pulse, which equals $\beta(\Omega_S)$, an expression for the integrand in eq. 20 is found (eq. 21) to be

$$\sin^2\left(\frac{\beta(\Omega_S)}{2}\right) = \frac{\omega_1^2}{\omega_1^2 + \Omega_S^2} \frac{1 - \cos\left[t_p(\omega_1^2 + \Omega_S^2)^{1/2}\right]}{2} \qquad (\text{eq. } 21)$$

Here, ω_1 is the microwave field strength of the second pulse in angular frequencies and t_p is the pulse length.

The theoretical consideration given above allows us to analyze experimental data and estimate the contribution of each individual dephasing process to the total dephasing rate $1/T_m$. For example, performing Hahn echo experiments with different flip angles $\beta(\Omega_S)$ of the inversion pulse displays the strength of the ID contribution compared with other dephasing mechanisms.

2.3.5. PELDOR

Distance measurements by PELDOR technique rely on the magnetic dipole–dipole interaction between electron spins, which is inversely proportional to the cube of the distance (eq. 15). For two nitroxide spin labels ($S = 1/2$, $I = 1$) at distances larger than 1.5 nm the magnetic dipole–dipole coupling is much smaller than the inhomogeneous linewidth in the EPR spectrum that is caused by hyperfine couplings and g anisotropy. PELDOR is a constant-time experiment and the intensity of the refocused echo of the observer electron spins A is

measured as a function of the time delay of a π pump pulse at frequency ω_B that inverts the state of spins B (Figure 9). The spins A and B should be well spectrally separated and selectively excited. Usually in biological applications, the paramagnetic species A and B are identical nitroxide radicals. The differentiation between A and B spins is achieved through the large A_{zz} hyperfine component of ~ 34 G. Spins A are defined as molecules in the nitrogen nuclear spin state $M_I = -1$ and with the molecular z axis almost parallel to B_0, while the spins B are molecules in the $M_I = 0$ (all orientations) and $M_{I = } \pm 1$ states with the molecular z axis perpendicular to B_0 (Figure 6B). Therefore, the central line of the nitroxide spectrum is excited with the pump pulse (ω_B) in order to achieve maximum modulation depth, whereas the low-field edge is chosen for detection frequency (ω_A) to acquire optimal sensitivity.
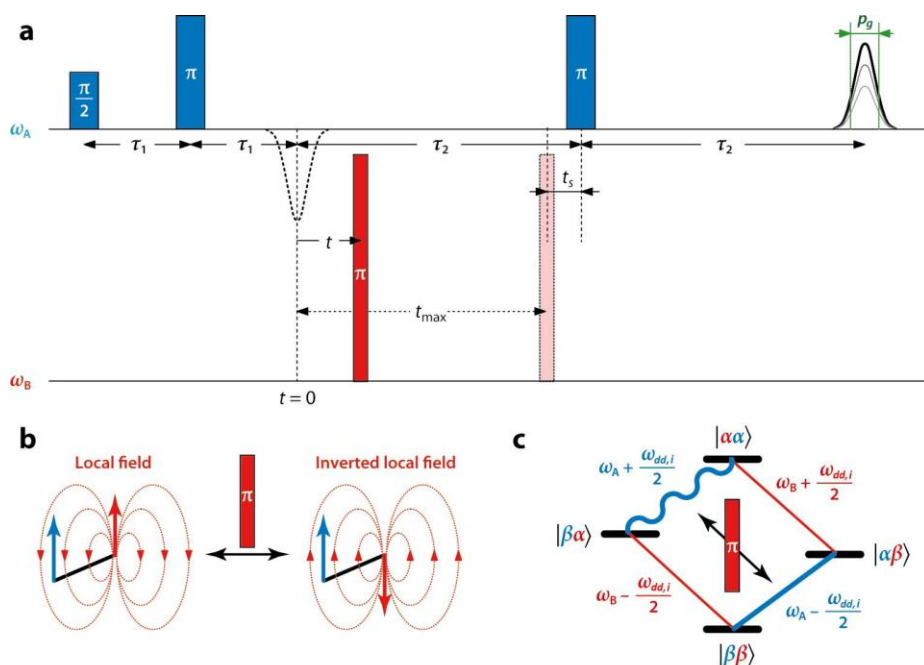
Figure 9. Four-pulse PELDOR experiment; (*a*) pulse sequence; delays τ_1 and τ_2 are kept fixed, while the time t is varied from $t < 0$ to t_{max}, and variation of the integral echo intensity in the window of length p_g is recorded; (*b*) local field picture; (*c*) energy level diagram.[1]

The time domain response of the PELDOR experiments is usually described as a product of two contributions (eq. 22)[87]

$$V\left(t\right) = V_{\text{intra}} \cdot V_{\text{inter}}$$ (eq. 22)

V_{intra} describes all spins coupled in one spin cluster, whereas V_{inter} takes into account the signal decay caused by the distribution of clusters in the sample. For the majority of spin-labeled lipids utilized in section 3.1, spin clustering is expected to be negligible, only in this case V_{intra} can be approximated to unity. In the PELDOR experiment, only the time during which spins evolve under a changed local dipolar field changes, whereas the contributions of all other dephasing mechanisms are constant. Therefore, it is possible to exclusively measure instantaneous diffusion which is proportional to the local electron spin concentration. The spatial distribution of spin labels can also be probed by PELDOR. In case of a homogeneous distribution in three dimensions, V_{inter} can be described by eq. 23:[88]

$$V_{\text{inter}} = \exp\left(-\frac{t}{T_{ID}^{PELDOR}}\right) \tag{eq. 23}$$

$$\frac{1}{T_{ID}^{PELDOR}} = \frac{2\pi\mu_0 g_A g_B \beta_e^2}{9\sqrt{3}\hbar} C\lambda \tag{eq. 24}$$

where λ being the fraction of spins excited by the PELDOR pump pulse at time delay t (modulation depth parameter), is also determined by eq. 20.

If inhomogeneous distribution of clusters occurs, characterized by a fractal dimension d, this will result in a stretched exponential decay:[88]

$$V_{\text{inter}} = \exp\left(-\alpha t^{d/3}\right) \tag{eq. 25}$$

where parameter α describes the decay rate in this case and transforms into $\dfrac{1}{T_{ID}^{PELDOR}}$ given by eq. (24) if $d = 3$.

Comparison of eqs. 19 and 24 yields the following relation for the dephasing rates caused by instantaneous diffusion in PELDOR and Hahn echo experiments

$$\frac{1}{T_{ID}^{PELDOR}} = \frac{2\lambda_{PELDOR}}{\lambda_{HE}}\frac{1}{T_{ID}^{HE}}, \tag{eq. 26}$$

where λ_{HE} is estimated to be ~ 0.3 according to eqs. 20 and 21 for Hahn echo experiment with 32 ns inversion pulse and λ_{PELDOR} has been determined experimentally ($\lambda_{PELDOR} \sim 0.52$).[89]

Equation 24 can be used to determine the local concentration of spin labels in different samples from PELDOR time traces.

If spin clustering is expected, the PELDOR signal also includes the specific intra-cluster interactions, V_{intra} (eq. 22).

Inversion of spin B_i changes the microwave resonance frequency (Larmor frequency) of spin A by the electron-electron dipolar coupling $\omega_{dd,i}$ (Figure 9C; eq. 15), which leads to a phase gain $\varphi_i = \omega_{dd,i}t$ of a fraction λ_i of the A spin magnetization.[1] As a consequence

$$v(t) = \prod_i \left\{ 1 - \lambda_i \left[1 - \cos(\omega_{dd,i}t) \right] \right\} \tag{eq. 27}$$

where the product runs over all spins B_i coupled to spin A.

Some additional assumptions have to be made for the application of PELDOR as a technique for measuring distance distributions. First, exchange coupling between the electron spins is neglected. Second, a spin pair is assumed in the cluster. Third, the correlation between λ_i and $\omega_{dd,i}$, which arises from the dependence of both quantities on θ_i, is neglected, and an orientation average is taken. With these assumptions, equation 27 converts to an expression for a macroscopically disordered sample

$$V(t) = \left\{ 1 - \lambda \left[1 - \int_0^1 \int_0^\infty P(R) \cos(\omega_{dd,i}t) dR d\cos\theta \right] \right\} V_{\text{inter}} \tag{eq. 28}$$

where $P(R)$ is the distance distribution function. If the spin cluster includes more than two spins, the signal takes the form $V(t) = F(t)V_{\text{inter}}$, with the form factor $F(t)$ being the product of all possible pair contributions. The echo amplitude $V(t)$ at a large evolution time ($t \to \infty$) can be described as:[2]

$$V(t \to \infty) = (1 - \lambda)^{N-1} \tag{eq. 29}$$

Therefore, the number of spins N in the cluster can be determined from the signal amplitude at large values of t, if the parameter λ is known independently from a structurally similar biradical system.

$$N = 1 + \frac{\ln\left(V(t \to \infty)\right)}{\ln(1-\lambda)} \qquad \text{(eq. 30)}$$

2.3.6. Data Analysis

The dipolar evolution function V_{intra} obtained after division of original PELDOR time traces by the intermolecular decay, was analyzed using Tikhonov regularization as implemented in the software package DeerAnalysis 2011[90] in order to obtain a distance distribution function $P(R)$. Conversion of V_{intra} to $P(R)$ is an ill-posed problem, meaning that small distortions in the time domain data (such as noise) may lead to a large deviation in the distance distribution. This problem can be overcome by usage of the Tikhonov regularization with an added nonnegativity constraint $P(R) \geq 0$. The time domain signal can be simulated based on the intra-cluster component (V_{intra}) of equation 28. The L-curve is a plot of the alpha term, a measure of the peak widths, against quality of fit, measured by mean square deviation between the experimental data and the simulation (Figure 10). The optimum regularization parameter (α) can be estimated from the corner of the L curve, since this provides the best compromise between smoothness (artifact suppression) and fit to the experimental data.

If additional information on the shape of the expected distribution is available, model-based fitting of $P(R)$ can be preferable. For instance, if a Gaussian distribution of distances centered at R_0 with standard deviation of σ is assumed then according to eq. 28 the PELDOR signal can be simulated by

$$V_{intra}(t) = \left\{ 1 - \lambda \left[1 - \int_R \Gamma(R) \int_0^1 \cos\left(\omega_{dd,i}t\right) d\cos\theta \, dR \right] \right\}$$

$$\Gamma(R) = A\exp\left(-B\frac{(R-R_0)^2}{\sigma^2} \right) \qquad \text{(eq. 31)}$$
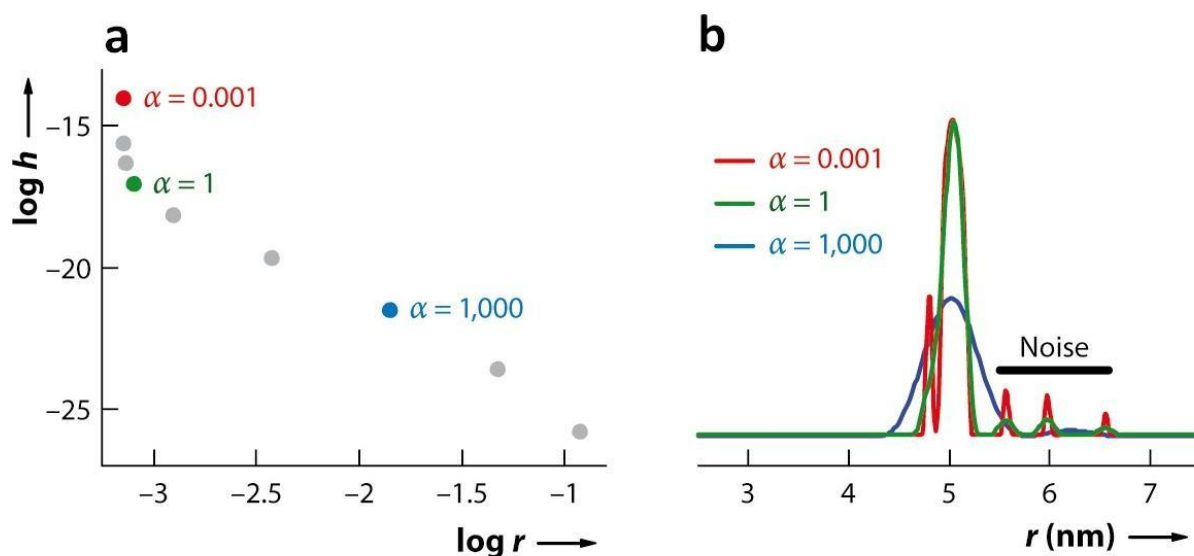
Figure 10. Data analysis and artifacts; (*a*) Tikhonov regularization L curve with three selected regularization parameters *α*; (*b*) distance distributions obtained by Tikhonov regularization with constraint $P(R)>0$. Undersmoothing (*red*) causes unrealistic peak splittings; oversmoothing (*blue*) causes artificial broadening; At the L-curve corner (*green*), $P(R)$ is most realistic.[1]

2.3.7. Modeling the Protein Structure Based on PELDOR Distance Constraints

Refinement of the protein structures using the PELDOR distance constraints depends on the proper prediction of the spin label conformation.[91] In this study, *in silico* spin labeling of the protein X-ray structures using rotamer library approach and estimation of interspin distances were performed using the MMM 2011 software package.[92] Fast and convenient predictions are possible by rotamer library modeling of the conformational space, i.e., by assuming a small number of canonical values for each of the dihedral angles of the side chain. In this approach, the interaction energy of each spin label rotamer with backbone atoms and neighboring side groups is computed from only a Lennard-Jones potential. For lack of a sufficiently large experimental database of spin label conformations, the most recent rotamer libraries are still calibrated by long MD runs. The rotamer library predicts a broader conformational distribution than is realistic and in some cases for instance loose positions in protein this might compensate for the protein backbone flexibility that is neglected. However, deviations between rotamer library predictions and experiment are most likely for the restricted positions. In some cases, comparisons have been made with the mtsslWizard which

operates as a plugin for the PyMOL molecular graphics. It has a simpler modeling approach that does not include Boltzmann weighting of rotamers but only removal of clashing conformations.

In the determination of relative arrangements of domains of a protein or components of a protein complex, assuming protein domain structures as rigid body will help to overcome the sparsity of distance constraints. If this approximation cannot be made, structures obtained from sparse constraints must be modeled with a coarse-graining approach or are uncertain. Modeller- and elastic network model-based fitting can be used to refine a known structure using a set of spin label distance constraints. Modeller[93] is the standard program for comparative protein structure modeling, i.e. modeling based on structures of homologous proteins. Such modeling appears appropriate in many applications of site-directed spin labeling (SDSL) EPR where a crystal structure or NMR structure of one state of a protein is known and information on the structure of other states is wanted. Since Modeller accepts additional restraints, experimental data from SDSL EPR can be used. Another approach for flexible fitting of conformational changes with a moderate number of distance constraints was suggested by Zheng and Brooks.[94,95] This approach is based on a residue-level anisotropic elastic network model (ANM) and restricts the protein motion to a small subset of the normal modes of the ANM. To overcome restriction to small-scale changes where the harmonic approximation inherent in the ANM is still valid, the Zheng/Brooks fit algorithm uses interactive reorientation of the modes. The distance constraints are combined with local pseudoenergy terms to set up a linear regression problem that is iteratively solved. With sparse restraints true coarse graining approaches, such as elastic network models, may be advantageous. In such a scenario one would create the first model by the Zheng/Brooks algorithm and test with Modeller how well this model is constrained by the experimental parameters. These modeling approaches are incorporated in the MMM 2011.2 software package and will be discussed in more details in section 3.4.4.

3. Results and Discussion

3.1 Optimization of Transversal Relaxation of Nitroxides for PELDOR in Membranes

3.1.1. Introduction

Although more than 30% of known genomes encode membrane proteins[96,97] and it is estimated that over 60% of all currently available drugs target these molecules,[98] determining their structure at high resolution remains a difficult challenge. Furthermore, while most membrane proteins are isolated and purified by the use of detergents, their reconstitution into liposomes is a crucial step in studying the mechanisms of action in the native environment. This is of great significance, because many membrane proteins will only display their full activity, if they are properly oriented and inserted into a lipid bilayer.[97,99-101] The high sensitivity of EPR spectroscopy makes it a valuable tool to study site-specific nitroxide-labeled membrane proteins in their native environments with reasonably small sample quantities.[102,103] PELDOR is a powerful technique to determine long-range distances[2,83] and relative orientations[104-106] in spin-labeled macromolecules and thus, provides valuable information and long-range restraints for structural modeling.[7] However, the applicability of PELDOR to membrane proteins in reconstituted systems has been limited because of much faster transversal relaxation time or generally spin echo dephasing time (T_m) of spin labels in lipid vesicles[8,105,107-112], as compared to detergent micelles.[105,111,113] Short T_m dampens the signal-to-noise ratio. A compensation of this effect using longer accumulation time or larger amount of sample is not always possible. In general, spin echo dephasing determines the feasibility of doing pulse experiments that depend upon echo detection.[85] Therefore, it limits the observation time window for PELDOR and thus, the maximum distance that can be measured due to Fourier arguments.[2] T_m of nitroxides in detergent micelles at 50K is in the order of a few microseconds (~2-3 µs) but in phospholipid membranes it can be less than 1 µs.[8,105,107-112] Such rapid spin echo dephasing is too fast for a reliable extraction of distances larger than 3 nm or the quantitative interpretation of broad distance distributions as commonly observed in membrane proteins.[2] In addition, the extraction of distances relies on a good

estimate of the PELDOR background function, which can be achieved only if a reasonable part of the dipolar evolution time is obtained (e.g. several times the inverse dipolar coupling). Background correction of time traces with low signal-to-noise ratio, a short time window or fast-decaying background is complicated and uncertain.[2] Therefore, it seems that the fast relaxation rates of spin-labeled membrane proteins in lipid bilayers are the major challenge for PELDOR applicability to such systems. In several recent publications, some methods are implemented to optimize sample conditions for PELDOR on spin-labeled membrane-associated proteins.[11,105,109,114,115] This study is the first systematic study of the mechanisms that are involved in enhanced transversal relaxation of nitroxides in phospholipid membranes. In order to optimize samples for PELDOR with respect to T_m, Hahn echo decay of spin labels in phospholipid vesicles has been studied under the conditions typically employed for PELDOR. The doxyl (4,4-dimethyloxazolidine-N-oxyl) derivatives of stearic acid[116-120] and phosphatidylcholine[121-125] (Figure 11) utilized in this study are well established spin label model systems for EPR studies in lipid membranes. In addition, C-terminal spin-labeled Gramicidin A (gA-PROXYL), as an extensively studied membrane-embedded peptide forming head-to-head dimers,[126,127] has been utilized to compare its relaxation behavior with the spin-labeled lipids in order to evaluate the optimization procedure on a membrane-embedded peptide.

T_m can be measured using a two-pulse Hahn echo experiment (Figure 8). When the time between the two pulses (τ) is increased, the echo is usually found to decay exponentially. Any process that shifts the resonance frequency of the electron spin by $1/\tau$ or more will prevent the spin from refocusing to form the echo and such process constitutes a dephasing mechanism.[85] These processes can be electron-electron dipole-dipole interaction,[81,128] nuclear spin diffusion,[81,85,86,129] instantaneous diffusion,[81] intramolecular dynamic processes and processes that average magnetically inequivalent environments such as librational motions,[85] rotation of methyl groups to which the unpaired electron is coupled[86] and relaxation of spin-coupled systems.[85] Furthermore, longitudinal relaxation (T_1) poses an upper limit to T_m.[81] All of these processes can contribute to T_m in solids and frozen solutions. Two-pulse Hahn echo and four-pulse PELDOR experiments have been performed to investigate how different factors including local and total spin label concentration, matrix deuteration, measurement temperature, presence of oxygen as paramagnetic relaxing agent, membrane composition and labeling position in the membrane, and cryoprotectant type affect the transversal electron spin relaxation.
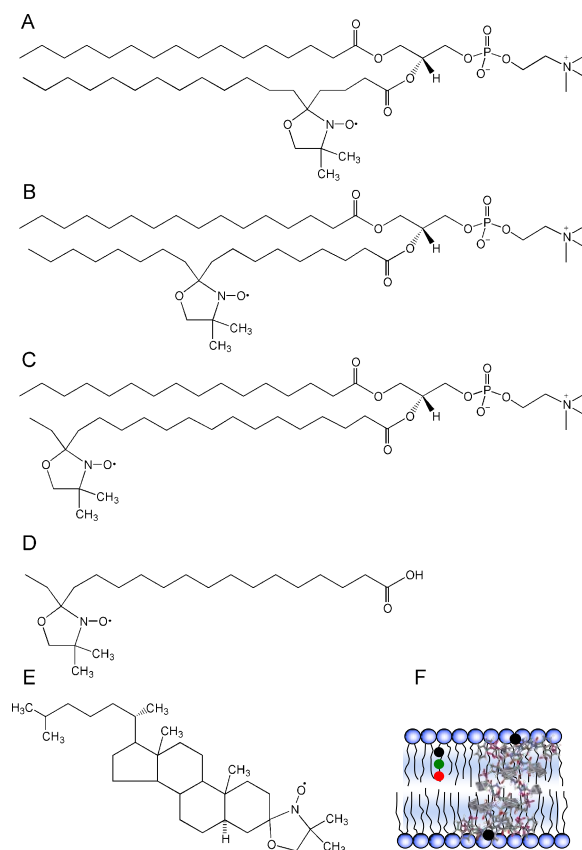
Figure 11. Chemical structure of lipid analogs; (*A*) 1-Palmitoyl-2-stearoyl-(5-doxyl)-*sn*-glycero-3-phosphocholine (5-PCSL); (*B*) 1-Palmitoyl-2-stearoyl-(10-doxyl)-*sn*-glycero-3-phosphocholine (10-PCSL); (*C*) 1-Palmitoyl-2-stearoyl-(16-doxyl)-*sn*-glycero-3-phosphocholine (16-PCSL); (*D*) (16-doxyl)-stearic acid (16-SASL); (E) (3*β*-doxyl)-5*α*-cholestane (SL-chol); (*F*) average position of *n*-PCSLs and gA-PROXYL in bilayer membranes.

3.1.2. Effect of Spin Label Concentration and

Electron-Electron Spin Interaction

As explained in section 2.3.5, both the local spin concentration and the spatial distribution of spin labels (16-SASL) in DPPC multilamellar vesicles can be deduced from PELDOR decay curves (Figure 12B). The curvature and slope of the PELDOR decay functions, which reflect the topology of the spin distribution and the local spin concentration via ID, respectively, differ for two samples with the same spin label (SL) but different phospholipid (PL) concentrations (molar ratios 1:100 and 1:1000). The dimensionality d of the spin label distribution function changes from 2.3 to 2.6 for the samples with high (SL/PL 1:100) and low (SL/PL 1:1000) spin label concentration in the membrane, consistent with previous

reports for spin labels in multilamellar vesicles ($2 \leq d \leq 3$).[130,131] In addition, T_{ID}^{PELDOR} changes by almost a factor of 7 by lowering the SL/PL molar ratio from (1:100) to (1:1000). Assuming a three-dimensional distribution of spin labels, local spin concentrations of 5 mM and 700 μM can be estimated from the decays of the PELDOR time traces. These concentrations are much higher than the total sample concentration of $\sim$ 100 μM. This difference arises from the fact that the spin labels are localized inside the lipid vesicles only. Obviously, the spin labels are not randomly 3D distributed in the 1:100 sample, leading to a strongly enhanced local concentration, whereas the 1:1000 sample is closer to a statistical 3D-distribution. The differences in the PELDOR trace hint at a larger average electron–electron dipolar interaction in the more concentrated sample. Moreover, the Hahn echo decay is much faster for the SL/PL (1:100) sample (Figure 12A; Table 1). The transversal relaxation time T_m increases by a factor of 1.7 from molar ratio of 1:100 to 1:1000 (Figure 12A). The estimated error of T_m measurements is less than 15% and is due to errors in SL/PL molar ratios and uncertainties in choosing the proper fitting curves, especially in the case of deeply modulated decay curves due to hyperfine interactions with nuclei. Further reduction of the SL/PL molar ratio ($<$ 1:1000) did not change T_m significantly (data not shown). Therefore, most of the further experiments were performed using a SL/PL molar ratio of 1:1000. It can be concluded that for SL/PL molar ratios higher than (1:1000), the echo decay is dominated by intermolecular dipolar interactions. However, the observed enhancement in T_m from Hahn echo decays is smaller than that of T_{ID}^{PELDOR} for PELDOR decays. Thus, the Hahn echo decay of the sample with SL/PL molar ratio of 1:1000 is limited by dephasing mechanisms other than ID, which is not the case for PELDOR. Accordingly, in the case of high local spin concentration in the membrane (SL/PL 1:100), the contribution of ID to electron spin echo dephasing is significant (eq. 18; Figure 13A):

$$\frac{1}{T_{SD}} < \frac{1}{T_{ID}^{HE}} \leq \frac{1}{T_{HF}} \qquad\qquad (\text{eq. 32})$$

Whereas dephasing is not dominated by ID for the sample with SL/PL molar ratio of 1:1000 (Figure 13B):[81,85]

$$\frac{1}{T_{SD}} < \frac{1}{T_{ID}^{HE}} << \frac{1}{T_{HF}} \qquad\qquad (\text{eq. 33})$$

T_m of 16-SASL in DDM micelles with the SL/DDM molar ratio of 1:100 is much longer than in the phospholipid sample with the same molar ratio (Figure 12A), which demonstrates that the major difference between spin labels in detergent micelles and membranes is their spatial distribution and thus their local concentration.[111,114] In addition, in the low concentration regime T_m is virtually independent of the spatial distribution of the vesicles within the samples. Therefore, it is possible to enhance the total concentration of spin labels and thus the EPR signal intensity by sedimentation of the samples. In this case, the addition of a cryoprotectant is not needed, due to the decreased water content of the samples.
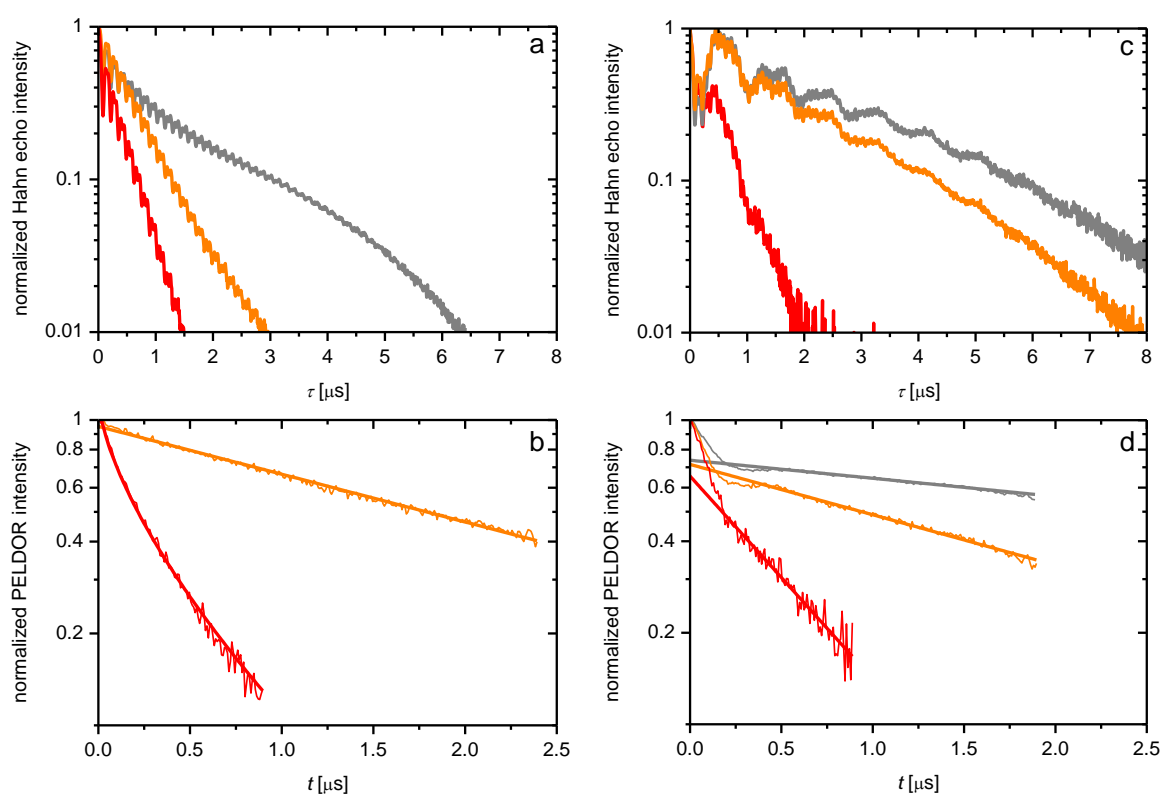
Figure 12. Effect of spin label concentration; (*a*) electron spin echo decays of the 16-SASL spin label in DDM micelle (molar ratio 1:100; gray) and in DPPC bilayers with SL/PL molar ratio of (1:100, red) and (1:1000, orange); (*b*) PELDOR time traces of 16-SASL in DPPC bilayers and the background fits with different dimensions: SL/PL 1:100 (fit with $d = 2$), SL/PL 1:1000 (fit with $d = 3$); (*c*) electron spin echo decays of gA-PROXYL in DMPC/D$_2$O bilayers with different molar ratios (SL/PL 1:100, red; 1:1000, orange; 1:4000, gray); (*d*) PELDOR time traces on samples in (c) and the background fits.

Similar results as for the spin-labeled lipid samples were obtained for the lipophilic C-terminus-labeled peptide gA-PROXYL in DMPC and DPPC bilayers and SDS micelle, in agreement with previous studies (Table 2; Figure 12C,D).[126,127] The estimated local peptide
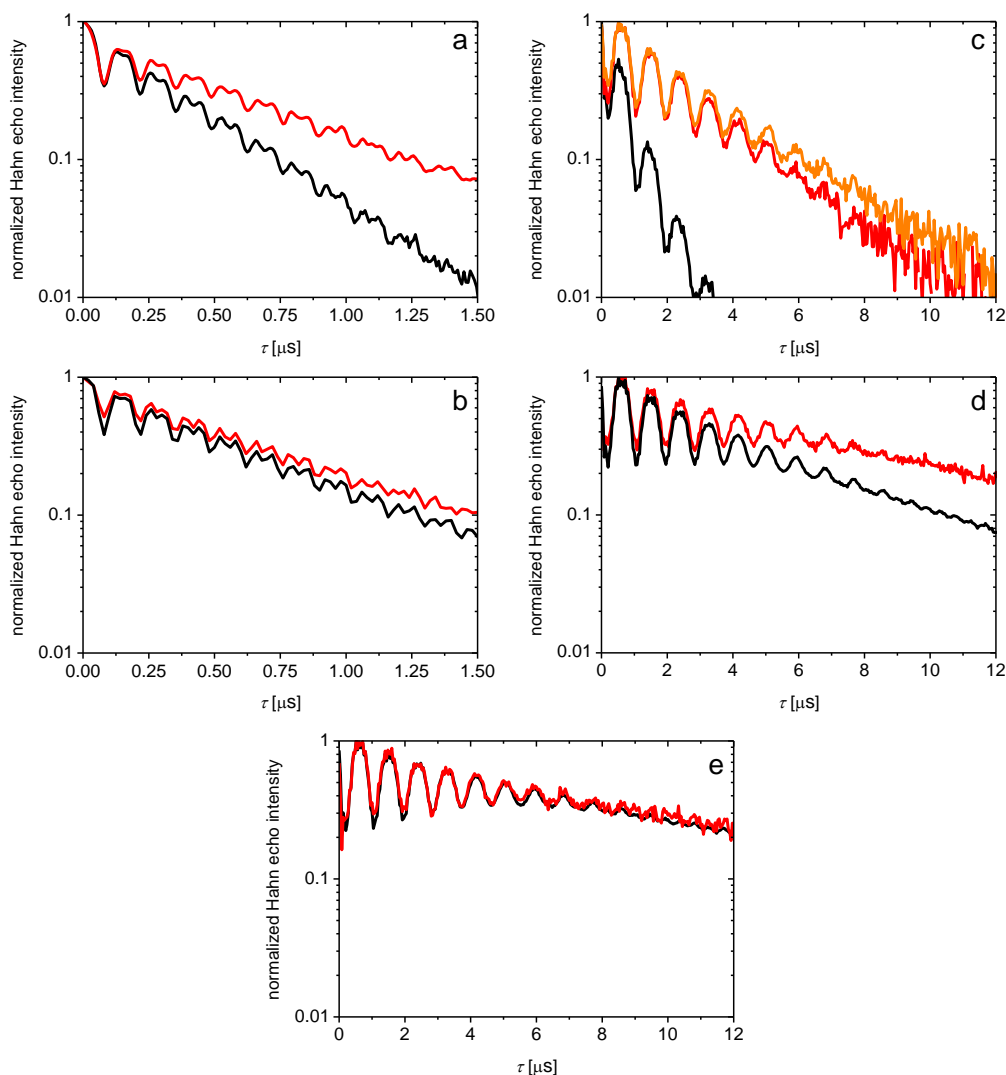
Figure 13. Electron spin echo decays of 16-SASL in DPPC membranes with the first $1/2\pi$ microwave pulse of 16 ns and two flip angles of the second pulse, 32 ns π (black), $1/8\pi$ (red), $1/8\pi$ recorded at 5 K (orange); (*a*) SL/PL (1:100) protonated DPPC; (*b*) SL/PL (1:1000) protonated DPPC; (*c*) SL/PL (1:100) acyl chain and buffer deuterated; (*d*) SL/PL (1:1000) deuterated; (*e*) SL/PL (1:10000) deuterated.

concentrations and corresponding dipolar decay time constants, probed by PELDOR measurements on gA-PROXYL samples (Figure 12D), confirmed the dilution of non-interacting dimers of gA-PROXYL in DMPC bilayers by increasing the lipid content. The echo dephasing rate ($1/T_m$) reduces significantly by decreasing the gA-PROXYL/DMPC molar ratio from 1:50 to 1:1000 and below 1:1000, T_m is almost independent of the local concentration in the membrane. In addition, for gA-PROXYL/DMPC (1:1000), the echo dephasing time T_m in large unilamellar vesicles (LUVs; Table 2) in which spin labels are more

uniformly distributed in the sample volume, is identical to that of multilamellar vesicles, suggesting that nitroxide spins are sufficiently separated in the later sample.

Table 1. Spin echo dephasing times (T_m) for the doxyl-labeled lipid samples.

sample properties[a]	T_m (µs)	T_{ID}^{PELDOR} (µs), best dimension fit[b]
16-SASL in DDM/H_2O/EG, SL/DDM (1:100)	1.18 ± 0.04	–
16-SASL in DPPC/H_2O/EG, SL/PL (1:100)	0.37 ± 0.04	0.38, 2.36
16-SASL in DPPC/H_2O/EG, SL/PL (1:100), 5K	0.39 ± 0.04	–
16-SASL in DPPC/H_2O/EG	0.65 ± 0.04	2.70, 2.62
16-SASL in DPPC-d_{62}/D_2O/EG-d_6, SL/PL (1:100)	0.78 ± 0.12	0.35, 2.14
16-SASL in DPPC-d_{62}/D_2O/EG-d_6	4.12 ± 0.12	3.40, 2.8
16-SASL in DPPC-d_{62}/D_2O/EG-d_6, SL/PL (1:10000)	6.87 ± 0.12	16.53, 2.9
16-SASL in DPPC-d_{62}/D_2O/EG-d_6, 5K	4.25 ± 0.12	–
5-PCSL in DPPC/H_2O/EG	1.86 ± 0.06	–
5-PCSL in DPPC/D_2O/EG-d_6	1.95 ± 0.06	–
5-PCSL in DPPC-d_{62}/H_2O/EG	2.05 ± 0.10	–
5-PCSL in DPPC-d_{62}/D_2O/EG-d_6	2.30 ± 0.10	2.74, 2.45
10-PCSL in DPPC/H_2O/EG	0.60 ± 0.04	–
10-PCSL in DPPC/D_2O/EG-d_6	0.81 ± 0.04	–
10-PCSL in DPPC-d_{62}/D_2O/EG-d_6	1.09 ± 0.12	1.63, 1.44
16-PCSL in DPPC/H_2O/EG	0.58 ± 0.04	–
16-PCSL in DPPC/D_2O/EG-d_6	0.50 ± 0.04	–
16-PCSL in DPPC-d_{62}/H_2O/EG	2.58 ± 0.12	–
16-PCSL in DPPC-d_{62}/D_2O/EG-d_6	2.66 ± 0.12	2.76, 2.97
16-SASL in POPC/H_2O/EG	0.99 ± 0.04	2.5, 2.58
16-SASL in POPC/H_2O/EG, oxygenated	1.03 ± 0.04	–
16-SASL in DOPC/H_2O/EG	1.24 ± 0.04	–
16-SASL in POPG/H_2O/EG	1.12 ± 0.04	–
SL-chol in POPC/H_2O/EG	1.70 ± 0.04	2.05, 2.68
SL-chol in POPC/Chol (80:20)/H_2O/EG	1.55 ± 0.04	–
16-SASL in octadecane	0.76 ± 0.04	–

[a] SL/PL molar ratios are 1:1000 and temperature is 50K if not mentioned otherwise.

[b] T_{ID}^{PELDOR} (µs) and best background dimension fit values are estimated from PELDOR time traces.

3.1.3. Effect of Acyl Chain and Buffer Deuteration

A major contribution to transversal relaxation appears in systems with abundant protons. Nuclear relaxation and nuclear motion lead to fluctuating hyperfine fields and thus to transversal relaxation of the electron spins. Therefore, we studied the influence of acyl chain and buffer deuteration on transversal relaxation of 16-SASL in DPPC membranes (Figure 14A). Since nuclear spin diffusion scales with the product of the nuclear magnetic moments

of the nuclei and electron−nuclear spin−spin coupling scales with the nuclear magnetic moment, electron spin dephasing by nuclei can be roughly approximated to scale with the nuclear magnetic moment to the third power.[85] For the exchange of protons to deuterons, this leads to a suppression of relaxation induced by nuclei by a factor of 35 (e.g., the relative magnetic moment to the third power). For the sample with SL/PL of 1:100, it is possible to increase T_m only by a factor of 2 by acyl chain and buffer deuteration. This effect is similar to lowering the SL/PL molar ratio by an order of magnitude.

Table 2. Spin echo dephasing times (T_m) for the gA-PROXYL samples.

sample properties[a]	T_m (µs)[b]
DMPC/D$_2$O, (1:100)	0.46 ± 0.10 (0.68)
DMPC/H$_2$O	1.90 ± 0.06
DMPC/D$_2$O	1.93 ± 0.10 (2.34)
DMPC-d_{67}/H$_2$O	2.10 ± 0.10
DMPC-d_{67}/D$_2$O	2.70 ± 0.12 (3.70)
DMPC-d_{67}/D$_2$O, LUV	2.66 ± 0.12
DMPC/D$_2$O, (1:2000)	2.27 ± 0.10
DMPC/D$_2$O, (1:4000)	2.47 ± 0.10 (6.00)
DPPC/H$_2$O	2.18 ± 0.06
DPPC/D$_2$O	2.33 ± 0.10
DPPC-d_{62}/H$_2$O	3.28 ± 0.10
DPPC-d_{62}/D$_2$O	3.75 ± 0.12
SDS-d_{25}/D$_2$O/glycerol-d_8, (1:100)	5.92 ± 0.12
SDS/H$_2$O/glycerol	3.08 ± 0.06
SDS/D$_2$O/glycerol-d_8	4.43 ± 0.12
SDS-d_{25}/D$_2$O/glycerol-d_8	5.75 ± 0.12 (13.7)

[a] Molar ratios are 1:1000 if not mentioned otherwise.

[b] T_{ID}^{PELDOR} (in µs) values are estimated from PELDOR time traces.

For the sample with SL/PL of 1:1000, an enhancement of a factor of 6.4 and a T_m as long as 4.1 µs has been achieved for the same deuteration level. For Hahn echo experiments the contribution of ID can be diminished by lowering the flip angle of the inversion pulse to $\pi/8$ (Figure 13). T_m of the 1:100 deuterated sample increases by almost a factor of 3 in this experiment (Figure 13C). This clearly demonstrates that, in deuterated samples, ID is the dominant dephasing mechanism at high local concentration of spins (eq. 34) similar to the protonated samples wherein the contribution of ID is significant.

$$\frac{1}{T_{HF}} < \frac{1}{T_{SD}} << \frac{1}{T_{ID}^{HE}}$$

(eq. 34)

When ID is not prevalent, proton spin diffusion (mutual spin flips of neighboring protons) is the next dominant mechanism.[81,85,86,129] For 16-SASL in protonated DPPC membranes, the stretching exponent value, x (eq. 17), is 0.72, indicating that relaxation is mainly driven by averaging nonequivalent environments such as rotation of methyl groups to which the unpaired electron is coupled.[86] This observation is in agreement with the local environment of 16-SASL in the center of phospholipid bilayers, which is exposed to aliphatic methyl groups at the end of acyl chains. Furthermore, in the case of 16-SASL, where the nitroxide radical is expected to be well embedded inside the membrane, the effect of buffer deuteration only is negligible (data not shown).
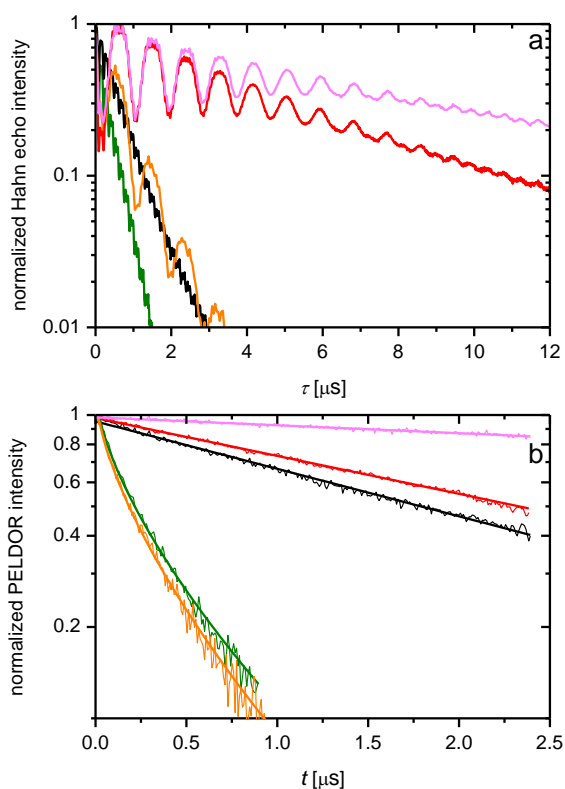
Figure 14. Effect of acyl chain and buffer deuteration; (*a*) electron spin echo decays of 16-SASL in protonated (SL/PL 1:100, green; SL/PL 1:1000, black) and acyl chain- and buffer-deuterated (SL/PL 1:100, orange; SL/PL 1:1000, red; SL/PL 1:10000, magenta) DPPC bilayers; (*b*) PELDOR time traces of these samples and 2D and 3D background fits for the 1:100 and 1:1000(0) samples, respectively.

To compare the spatial distributions of spin labels, which should not be affected by matrix deuteration, we performed PELDOR measurements on the samples with deuterated matrices (Figure 14B). T_{ID}^{PELDOR} values and dimensionalities of the spin label distribution are in good

agreement with the protonated samples when small differences in SL/PL molar ratios due to sample preparation are considered (Table 1). It is important to note that by reducing the proton spin diffusion by deuteration, instantaneous diffusion again dominates the electron spin echo dephasing. For the deuterated sample with SL/PL molar ratio of 1:1000 (eq. 35; Figure 13D):

$$\frac{1}{T_{SD}} < \frac{1}{T_{ID}^{HE}} \leq \frac{1}{T_{HF}}$$

(eq. 35)

Therefore the molar ratio has been lowered to 1:10 000 to achieve a Hahn echo decay that is not dominated by ID and SD any more (eq. 36; Figure 13E,14A):

$$\frac{1}{T_{SD}} < \frac{1}{T_{ID}^{HE}} << \frac{1}{T_{HF}}$$

(eq. 36)

The PELDOR data on the highly diluted 1:10 000 sample exhibits a homogeneous 3D distribution (best dimension fit of 2.9) and a local spin concentration of 117 μM that is in good agreement with to the total sample concentration of 100 μM (Figure 14B).

3.1.4. Effect of Lipid Composition of Phospholipid Membranes

To study the effect of lipid composition on the transversal relaxation of nitroxides, samples of 16-SASL and SL-chol in protonated phosphatidylcholine bilayers with different saturation levels of acyl chains (from DPPC to DOPC) and different headgroups (POPG) have been studied (Figure 15A; Table 1). The effects are more pronounced when the nature of the acyl chain is changed rather than the type of headgroup, as can be seen for 16-SASL (Table 1). From 16-SASL in DPPC to DOPC, T_m increases by a factor of 2. This enhancement might be caused by a decrease in perturbation by the nitroxide moiety in the less-ordered POPC and DOPC membranes as compared to the more ordered DPPC membranes.[122] However, by comparison of PELDOR time traces of DPPC and POPC samples (Figure 15B), their T_{ID}^{PELDOR} values are similar. Therefore, the average distance between spins is not affected and this difference in T_m might be caused by other effects such as different local concentration of protons and particularly terminal methyl groups around the spin label. Furthermore, the

average lateral pressure in the middle of the bilayer is higher for DPPC in comparison to POPC and DOPC membranes as proposed by molecular dynamics simulations.[132] This might increase the exposure of spin labels to chain protons.
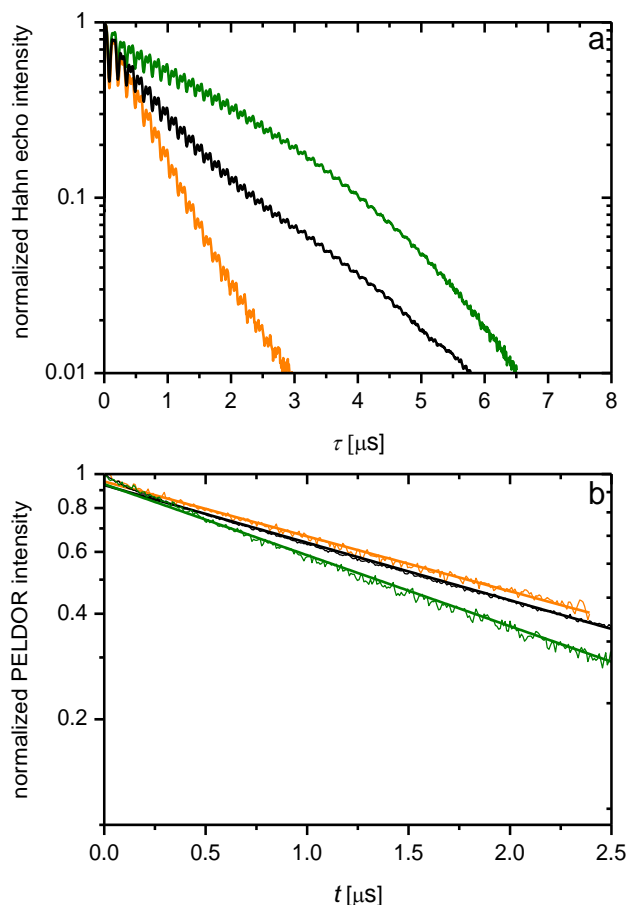
Figure 15. Effect of lipid composition; (*a*) Electron spin echo decays of 16-SASL in DPPC (orange) and 16-SASL (black) and SL-chol (green) in POPC bilayers with SL/PL of 1:1000; (*b*) PELDOR time traces of these samples and 3D background dimension fits.

3.1.5. Effect of Spin-Labeled Molecules and Spin Label Position

In order to investigate the dependence of the transversal relaxation of nitroxides on the immersion depths in the membranes, we utilized three different spin-labeled phosphatidylcholine analogues (*n*-PCSLs; Figure 11) in DPPC bilayers (Figure 16).[124,133] In addition, the effect of buffer and acyl chain deuteration was studied independently and position-dependently (Figure 16; Table 1). For the buffer- and chain-deuterated samples, the T_m is in the order 16-PCSL > 5-PCSL > 10-PCSL (Figure 16A), whereas for protonated
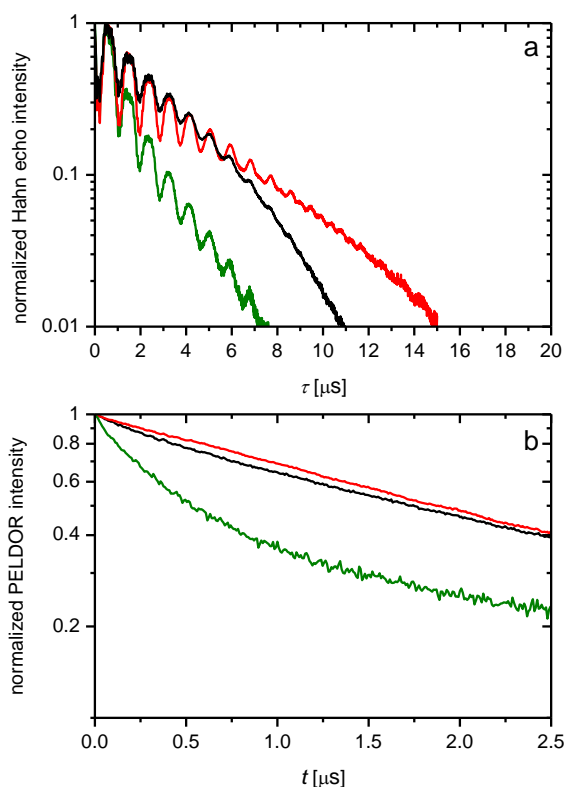
Figure 16. Effect of spin label position; (*a*) electron spin echo decays of *n*-PCSL spin labels in acyl chain- and buffer-deuterated (DPPC-d_{62}/D$_2$O/EG-d_6) bilayers with SL/PL molar ratio of 1:1000. 5-PCSL (black), 10-PCSL (green), and 16-PCSL (red); (*b*) PELDOR time traces of these samples.

samples, it is in the order 5-PCSL > 10-PCSL ~ 16-PCSL (Table 1). Consistent with the average position of *n*-PCSLs relative to the lipid−buffer interface,[124] the relaxation of 16-PCSL is independent of buffer deuteration but T_m of 5-PCSL is, by a factor of 1.1, higher in chain- and buffer-deuterated sample in comparison to just chain-deuterated sample (Table 1).

The spatial distribution of *n*-PCSLs in buffer and chain deuterated samples was investigated by PELDOR (Figure 16B). 16-PCSL showed a homogeneous three dimensional spin-distribution whereas 5-PCSL deviates slightly and 10-PCSL deviates significantly from this behavior. Especially for 10-PCSL, this deviation can be due to segregation or clustering of spin labels,[130,131] consistent with the shorter T_m in the perdeuterated 10-PCSL sample. In addition, our results indicate that as long as the intermolecular interactions among spin labels are comparable, electron spin echo dephasing is dependent on the immersion depth into the bilayer, but independent of the nature of nitroxide spin label. For instance, a similar trend in echo decay as 5-PCSL is observed for SL-chol as a spin-labeled cholesterol analog with
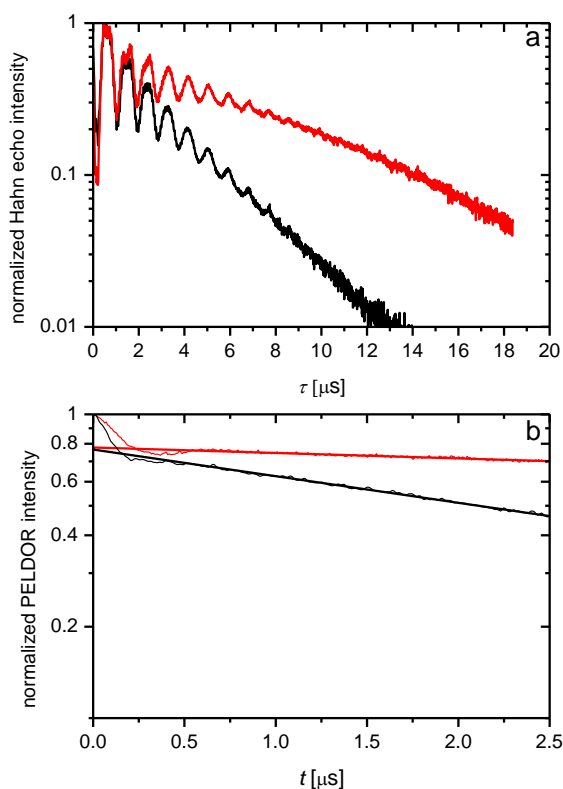
Figure 17. Comparison of the effect of matrix perdeuteration for gA-PROXYL in SDS micelles (red) and DMPC multilamellar vesicles (black) with molar ratio of 1:1000; (*a*) electron spin echo decays; (*b*) PELDOR time traces.

similar position in the membrane (Figure 11; Figure 15A; Table 1). In protonated DPPC membranes T_m enhances by a factor of three from 16-PCSL to 5-PCSL (Table 1). Interestingly, a similar trend in echo decay as SL-chol and 5-PCSL has been shown for water-exposed labels. Therefore it seems that the higher T_m of spin labels which are located close to polar-apolar interface in comparison to the center of the bilayer is due to their proximity to water. A more detailed description of this effect can be found in the supporting information of reference [134].

Furthermore, the effect of solvent and lipid deuteration was studied for the investigated gA-PROXYL samples (Table 2; Figure 17). In both DMPC and DPPC vesicles, the nitroxide moiety is located close to the polar−apolar interface,[127] and therefore the relaxation behavior of gA-PROXYL in these compositions resembles that of spin-labeled lipids such as 5-PCSL, wherein the nitroxide is in the proximity of solvent (Tables 1 and 2). In DPPC and DMPC bilayers, a significant difference in T_m can be found only between protonated and

45

perdeuterated samples, although the T_m increment due to acyl chain deuteration is higher in DPPC compared to DMPC with the shorter acyl chain length.[126,127]

In addition, to compare spin-labeled gramicidin A in perdeuterated lipid bilayers with detergent micelles, samples of gA-PROXYL in micelles of perdeuterated SDS were prepared (Figure 17). Deuterium accessibility analysis and the ^{14}N hyperfine coupling constant for gA-PROXYL in SDS micelles confirmed that nitroxides are accessible to the solvent (data not shown).[129] According to the PELDOR measurements, the overall conformation of the gramicidin dimer is conserved in SDS micelles. But in contrast to phospholipid membranes, for gA-PROXYL/SDS molar ratios lower than 1:50, echo dephasing is independent of molar ratio and T_m is significantly higher than in phospholipid membranes (Figure 17A; Table 2). Furthermore, by comparing the corresponding PELDOR traces (Figure 17B), it is clear that SDS micelles that enclose dimers are uniformly distributed in the sample (T_{ID}^{PELDOR} 13.7 μs).

3.1.6. Effect of Temperature, Presence of Oxygen, and Cryoprotectant Type

T_m relaxation is well-known to be temperature-dependent. Usually the low-temperature maximum of nitroxide T_m in glassy frozen solvents is reached already at 50 K. However, if T_m is dominated by spectral diffusion, the relaxation rate will also depend on T_1. The latter should decrease monotonously with decreasing temperature. This expectation could be confirmed by lowering the temperature to 5 K for 16-SASL in DPPC (SL/PL of 1:100). Here, the relaxation rate reduces slightly almost regardless of proticity and ID (Table 1; Figure 13C), whereas for the concentration-optimized protonated and deuterated (DPPC) samples, T_m is independent of temperature from 50 K downward (Table 1). In the former case, T_m is dominated by spin−spin interactions, but in the latter case, nuclear spin diffusion is the dominant relaxation mechanism and at temperatures below 50 K this exhibits only small temperature dependence.[128]

Oxygen is known as a paramagnetic relaxation agent for spin labels. In order to test its significance for transversal relaxation enhancement at 50 K, the concentration-optimized sample of 16-SASL in POPC was purged with air. As a result, only a small variation in T_m has been observed (Table 1). For the acyl chain- and buffer-deuterated sample of 16-SASL in DPPC-d_{62}, T_m was invariant with respect to the oxygen content, which is consistent with

literature.[85,129] In the case of DPPC multilamellar vesicles, oxygen diffusion is slow, because the membrane is already in the gel phase at room temperature. No effect has been observed for changing the cryoprotectant from ethylene glycol to glycerol and varying its concentration between 20% (v/v) and 50% (v/v). The spin labels are partitioned into the multilamellar vesicles and experience higher local concentrations as compared to the nominal bulk concentration as discussed above. Thus, aggregation of vesicles due to ice formation in the samples does not significantly alter the local concentration of spin labels. Therefore, the use of cryoprotectant at all shows little effect on T_m as compared to systems with spin labels in the aqueous phase.

3.1.7. Discussion

At high local concentration of spin-labeled species in the membrane, dephasing due to dipolar interaction of electron spins that manifests itself in ID due to excitation of spins by a microwave pulse is an important contributor to T_m within the studied temperature range. Thus, in the high-concentration regime, ID conceals the relaxation caused by coupling of electrons to the matrix protons of the lipid acyl chains, of the protein itself, and of the buffer (for nitroxides located in the proximity of water protons). Therefore, the first step in optimization of transversal relaxation time is to inhibit spin clustering. As for the gA-PROXYL in DMPC (Table 2; Figure 12C), this inhibition can be achieved by increasing the ratio of lipid to spin-labeled species.[11,111,114,115] However, if spin labels tend to segregate in bilayer membranes, as in the case of 10-PCSL in DPPC membranes, then their dilution by increasing the lipid content will be less effective,[105,107] although in such cases implementing magnetically dilute samples, in which spin-labeled membrane proteins are intermixed with wild-type proteins, is helpful.[105,109] In the case of spin-labeled phospholipids, partial segregation of them in DPPC bilayers in the gel phase[121-125,135] and increased segregation for labeling positions toward the center of the chain ($n = 8-10$) have been observed previously.[121-125] These findings are in accordance with the observed order of dephasing rates 10-PCSL > 5-PCSL > 16-PCSL observed here. However, if the bilayer structure is disturbed by the nitroxide moieties and this induces segregation of labeled phospholipids, and thus enhances echo dephasing rates, then it might be possible to compensate this effect, for instance, by changing the composition of the membrane.[122] Lateral packing (pressure) in bilayer membranes directly depends on composition and position in the membrane. Therefore, the introduction of nitroxide spin

labels leads to increased perturbation at positions where the packing level is high, for instance, close to the geometric center of the acyl chain. Accordingly, hydrophobic mismatches and lateral packing defects are important motives that stabilize the aggregate or oligomeric form of integral membrane proteins.[126,127,136] Thus, the major parameter that governs segregation of spin-labeled species, regardless of their size and nature, might be the amount of perturbation in bilayer structure that can be introduced by inclusion of them.[122,136]

In addition, as is evident from PELDOR data, local concentrations of 16-SASL and SL-chol in protonated DPPC and POPC membranes are similar, but the corresponding relaxation rates are significantly different (Figure 15; Table 1). For low local concentrations of spin-labeled species in membrane, transversal relaxation is mainly driven by proton spin diffusion.[85,86,129] Generally, the transversal relaxation of electron spins below 50 K strongly depends on the concentration of nonmethyl protons and on the concentration and type of methyl protons in the environment, on length scales in the range 6−20 Å.[86] Thus, a significant enhancement in T_m can be achieved by deuterium exchange of these protons.

The PELDOR background decay is governed by instantaneous diffusion. The rate of the PELDOR background decay can be related to the ID dephasing rate from the Hahn echo decay (eq. 26). This is of great importance because a precise estimation of the PELDOR background function is essential for reliable extraction of distances. The contribution of ID can be separated from T_m by extrapolation to very small turning angles of the second microwave pulse (eqs. 19 and 20).[81] The importance of instantaneous diffusion in echo dephasing depends on the magnitude of other contributions to T_m (eq. 18).[85] In the case of 16-SASL in protonated DPPC membranes, ID makes an important contribution to T_m at SL/PL molar ratios of around 1:100 (Figure 13A; eq. 32), which corresponds to local spin concentration of a few millimolar, whereas in deuterated phospholipid membranes, the significance of ID persists to much lower spin concentrations (SL/PL molar ratio of 1:1000; Figure 13D; eq. 35). In deuterated samples T_m can be enhanced maximally by a factor of 1.7 for SL/PL molar ratios lower than 1:1000 (Figure 14A). It has been shown before that at sufficiently long time, during which electron coherence evolves or at high concentrations of spin labels, the sensitivity of PELDOR can be enhanced by reducing ID via increasing the length of the observer pulses and thus decreasing the excitation bandwidth.[83] In some exceptional cases, this might be an option to improve the quality of PELDOR on a given sample.

3.2. PELDOR Distance Measurements in Detergent Micelles

3.2.1. Introduction

One approach in pulse EPR distance measurement by PELDOR is to covalently attach two spin-labels to a macromolecule and measure the inter-spin distance. Alternatively, singly-labeled components of a system that forms aggregates or oligomers can be employed. This situation has been referred to as a spin-cluster. All methods to derive structural information from PELDOR time traces rely on the assumption that the inter-cluster background signal can be separated from the specific intra-cluster interaction under study. However, an erroneous assumption of the background function can cause artifacts in the data analysis. In frozen solutions of model compounds in organic solvents,[4,137,138] or soluble proteins[139,140] the distribution of spin-clusters can be approximated to be homogeneous in three-dimensional space. The background signal corresponding to such a distribution is an exponential decay function (eq. 23). The distribution of spin-clusters in lipid vesicle membranes can also be assumed to be homogeneous. As it was discussed in section 3.1, the dimension of this homogeneous distribution varies from two to three depending on the sample concentration. This corresponds to a stretched exponential decay function describing the background (eq. 25). In contrast to homogeneous solutions and lipid vesicles, spin-labels in detergent micelles are confined to small volumes. This leads to an inhomogeneous distribution of spin-clusters on the length scale accessible by the PELDOR method. Several earlier works have relied on PELDOR to investigate size restriction effects in microscopic assemblies. Ruthstein et al. have characterized micelles with respect to micelle size and aggregation number. The micelles were formed from pluronic block copolymers built from chains of poly(ethylene oxide) and poly(propylene oxide).[141] In a second study the formation of mesoporous materials from solutions of these micelles was monitored using PELDOR.[142] Mao et al. investigated the local structures in organically modified layered silicates and their composites with polymers. PELDOR on spin-labeled surfactants allowed the extraction of local spin concentrations and the fractal dimension of the homogeneous spin distribution.[143] The lateral diffusion of spin-labeled thiols on spherical gold nanoparticles has been studied by Ionita et al. The spin–spin distance distribution function was extracted from PELDOR data.[144]

In this study, the effects of this size restriction on the PELDOR signal have been investigated especially on micelles formed from detergents that are frequently used for solubilization of membrane proteins (Figure 18A).[145] Therefore, the characteristics of the intermolecular dipolar interactions between single spin-labeled fatty acid molecules statistically partitioned into detergent micelles have been explored. We have chosen spin-labeled fatty acids instead of large macromolecules as test system, because they do not give rise to large exclusion volumes, the conformational freedom of the spin-label moiety is less hindered and the structure of the micelle will be less distorted (Figure 18B).

We find that the resulting time traces cannot be described by stretched exponential decay functions but can be simulated based on literature values for the detergent micelles dimensions and aggregation numbers and a statistic distribution of spin-labels inside the micelles. Since a specific interaction between the spin-probes is not observed, these statistic aggregates resemble a background function for detergent micelles. Understanding the background signal in detergent micelles is of importance for spin-labeled membrane proteins and peptides solubilized in detergent micelles or small vesicles for PELDOR measurements. Based on two different models for the distribution of the spin-labels (surface and bulk distribution) the data can be modeled quantitatively based on the size of the micelles (D), their aggregation number (n), the spin-label concentration (c) and the degree of spin-labeling (p). Detailed description of the modeling of PELDOR time traces is discussed in appendix C.
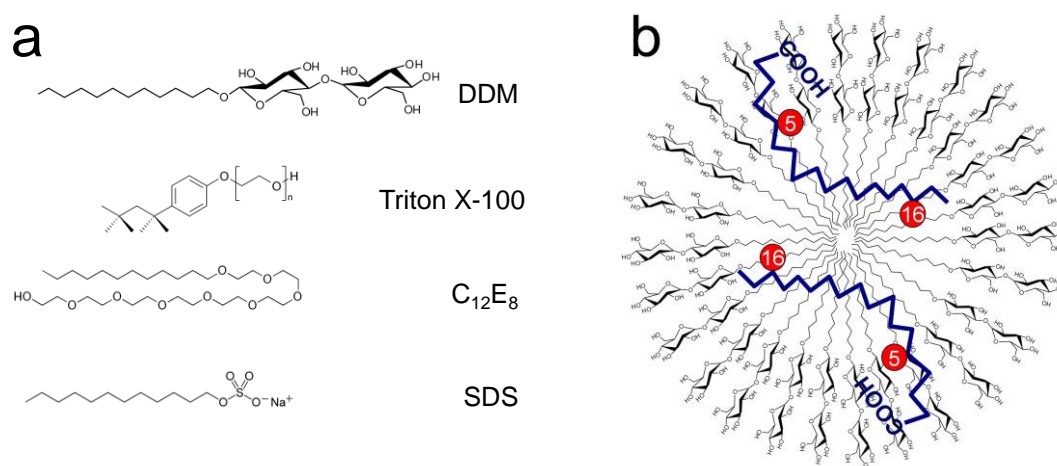
Figure 18. (*a*) Chemical structure of the utilized detergents; (*b*) estimated position of 5- and 16-SASL in DDM micelle.

3.2.2. Results and Discussion

The experimental PELDOR time traces for two different spin-labeled fatty acids (5-SASL and 16-SASL) incorporated into several micelles (DDM, SDS, $C_{12}E_8$ and Triton X-100) are shown in Figure 19. All of them exhibit a fast initial decay and a slow decay component which persist for the length of the observation window. None of the traces can be fitted by a stretched exponential decay function. To remove the homogeneous inter-micellar background the time traces have been divided by an exponential decay function fitting the slow component. The modulation depth for most of the samples are rather similar (27–32%); only the sample of 3 mole% 16-SASL in DDM shows a somewhat larger value of 38%. The PELDOR time traces were corrected for background decay using a homogeneous three-dimensional spin distribution. For 16-SASL the mean distances, obtained from the time traces by Tikhonov regularization ($\alpha = 1000$) are all between 2 and 2.5 nm (Figure 20). Given the broad distance distribution width ($\sigma(r) \sim 0.6$–1.3 nm) they are rather similar. In the case of 5-SASL in DDM the mean distance is significantly shifted to almost 3 nm. Two-pulse ESEEM (electron spin echo envelope modulation) measurements on the utilized samples in deuterated buffer (Figure 21),[129] as a measure for accessibility to water, as well as nitroxide A_{zz} values that are sensitive to the polarity of spin-label environment (Table 3),[129,146] are consistent with the observed slight changes in the PELDOR distances. In the case of the SDS micelles the significant higher water accessibility is probably due to the small size of the detergent headgroup (Figure 18).

These distinct distances are not caused by specific interactions between the spin-labeled fatty acids but reflect the distance restrictions imposed by the finite micelle dimensions. It is important to note that we cannot rule out the presence of specific interactions between spin-labels. However, utilizing the same spin-labels in phospholipid vesicle membranes homogeneous distributions have been observed (Section 3.1.2). Thus, there is no indication of specific interactions. Furthermore, if the spin-labels form specific structures with short spin–spin distances, their dipolar coupling will be too large to be excited by the microwave pulses. Thus, we can neglect their contribution to the PELDOR signal in good approximation.
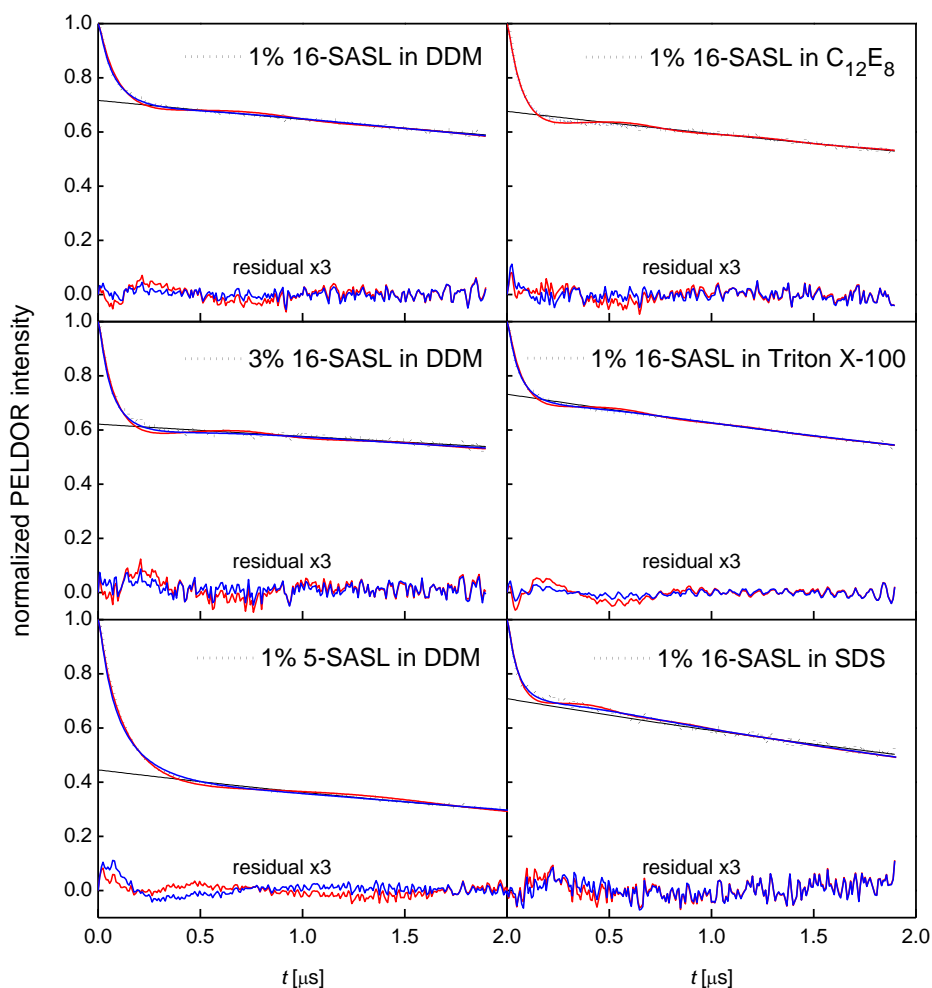
Figure 19. The model fits in different detergent micelles. Experimental data is given in dotted black, the PELDOR background functions in solid black, surface model in red and the bulk model in blue. Below each trace the residual of experimental data minus simulation multiplied by three is displayed.

Table 3. Nitroxide A_{zz} values measured by 9.4 GHz (X-band) cw EPR at $T = 70$K.

Sample	A_{zz} (mT)
TEMPOL in water	7.58±0.02
1% 16-SASL in SDS	7.15±0.02
1% 5-SASL in DDM	7.00±0.02
1% 16-SASL in $C_{12}E_8$	6.98±0.02
1% 16-SASL in Triton X-100	6.86±0.02
1% 16-SASL in DDM	6.81±0.02
3% 16-SASL in DDM	6.81±0.02
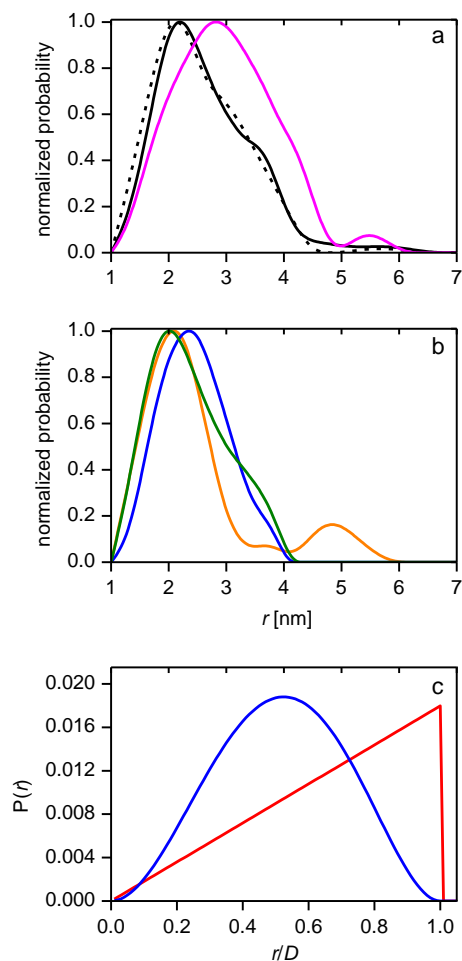
Figure 20. Distance distributions; (*a,b*) obtained distance distributions from Tikhonov regularization for different detergent micelles; 1% 16-SASL/DDM (solid black), 3% 16-SASL/DDM (dashed black), 1% 5-SASL/DDM (magenta), 1% 16-SASL/Triton (green), 1% 16-SASL/$C_{12}E_8$ (blue), 1% 16-SASL/SDS (orange); (*c*) distance probability densities for the two different distribution models in micelles; bulk model (blue), surface model (red).
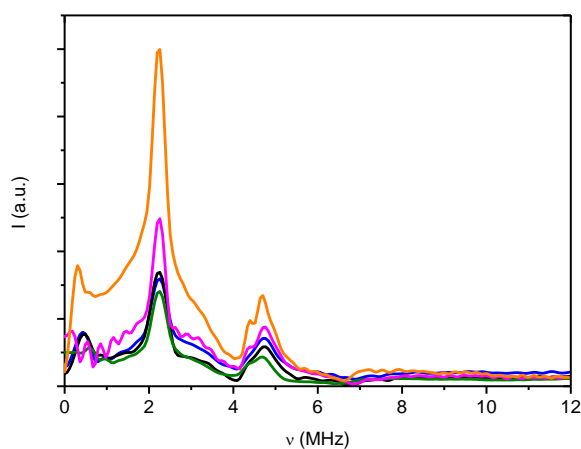
Figure 21. Two-pulse ESEEM spectra of the utilized samples in deuterated buffer; same color code as Figure 20.

Simulations based on the surface and bulk distribution model together with their deviation from the experimental PELDOR time traces are shown in Figure 19. The parameters (n, D, c and p) of both models, surface and bulk, have been optimized by minimizing the root mean square deviation between the experimental data and the simulation based on Eq. (44). Both models show a very good agreement with the experimental PELDOR time traces. The surface model exhibits a slightly larger divergence. This model predicts a large contribution from spin pairs at the maximum distance (Figure 20C) leading to a shallow but distinct dipolar modulation in the simulations. This oscillation is not visible in the experimental data; however, already a moderate distribution in micelle diameters will easily diminish this oscillation. The optimal fitting parameters for n, D, c and p are summarized in Table 4. The initial fast decay of the time traces can be attributed to the dipolar interaction of spin-labels within one micelle, whereas the slower decay results from the dipolar interactions between spin-labels in different micelles. The different influence of the parameters n, D, c and p on the PELDOR time traces is noteworthy. The micelle diameter D mostly influences the fast initial decay of the PELDOR time traces, whereas the spin-label concentration c determines the slope of the slowly decaying part. In contrast, both n and p contribute mainly to the modulation depth and have only minor effects on the fast initial decay of the PELDOR time traces. In principle, p governs the amount of multi-spin effects[147] and, thus, also contributes to the dipolar evolution caused by spin-labels within one micelle. In cases of broad distance distributions and moderate labeling degrees these effects are usually not resolved experimentally.[89] As a consequence, these two parameters are strongly interdependent. To separate them, we also fitted all time traces by fixing p to the nominal labeling degree. For 16-SASL, simulations with both models reproduce the literature values for D nicely.[145,148] It is important to note that micelle diameters are usually derived from the radius of gyration including a solvent shell. However, in the present study the nitroxide moiety is expected to be located between the micelle's hydrophobic core and the polar-apolar interface, well inside of this solvent shell. 5-SASL results in larger micelle diameters. This might be caused by a distortion of the micelle by the labeling close to the head-group. Otherwise, it might indicate that neither model fully reflects the real distribution in the micelle. The polar head-group of the fatty acid is assumed to be restricted to the polar-apolar interface close to the micelle surface. In this case, the nitroxide moiety of 5-SASL can occupy a spherical shell with a bigger mean radius as compared to 16-SASL. A shorter linker between head-group and nitroxide moiety restricts the nitroxide to the periphery of the micelle. This is in agreement

with the water accessibility and polarity measurements (Figure 21; Table 3). Thus, in the approximation that the variations of radii of this spherical shell arise from the length of this linker, the variation of radii will be much smaller for 5-SASL as it is much more closely linked to the head-group.

Table 4. Relevant micelle and sample parameters.

Sample	Triton X-100 1% 16SASL	SDS 1% 16SASL	C12E8 1% 16SASL	DDM 1% 5SASL	DDM 3% 16SASL	DDM 1% 16SASL
n	75[a], 140[a], 96-165[a]	62[b]	89[a], 98[a], 120[a]	110[a], 126[a], 111-140[a], 78-149[c], 140[c], 135-145[c]	110[a], 126[a], 111-140[a], 78-149[c], 140[c], 135-145[c]	110[a], 126[a], 111-140[a], 78-149[c], 140[c], 135-145[c]
D [nm]	6.84[a], 7.50[a]	3.38-3.7[d], 3.1 (core)[a]	6.44[a], 8.04[a], 3.1 (core)[a]	5.98[a], 6.24[a], 2.82-5.8[c], 3.1 (core)[a]	5.98[a], 6.24[a], 2.82-5.8[c], 3.1 (core)[a]	5.98[a], 6.24[a], 2.82-5.8[c], 3.1 (core)[a]
$c_{surface}$ [µM]	316[e], 316[f]	430[e], 430[f]	252[e], 255[f]	436[e], 435[f]	167[e], 208[f]	229[e], 228[f]
$n_{surface}$	110[e], 139[f]	121[e], 144[f]	143[e], 170[f]	217[e], 272[f]	244[e], 67[f]	116[e], 136[f]
$P_{surface}$	1.27%[e], 1%[f]	1.19%[e], 1%[f]	1.19%[e], 1%[f]	1.26%[e], 1%[f]	0.79%[e], 3%[f]	1.17%[e], 1%[f]
$D_{surface}$ [nm]	3.20[e], 3.23[f]	2.91[e], 2.91[f]	3.26[e], 3.26[f]	4.29[e], 4.30[f]	3.44[e], 2.91[f]	3.56[e], 3.57[f]
c_{bulk} [µM]	310[e], 309[f]	423[e], 423[f]	244[e], 243[f]	416[e], 417[f]	159[e], 158[f]	221[e], 221[f]
n_{bulk}	110[e], 142[f]	123[e], 145[f]	132[e], 172[f]	161[e], 273[f]	48[e], 65[f]	143[e], 138[f]
P_{bulk}	1.29%[e], 1%[f]	1.18%[e], 1%[f]	1.30%[e], 1%[f]	1.70%[e], 1%[f]	4.07%[e], 3%[f]	0.96%[e], 1%[f]
D_{bulk} [nm]	4.19[e], 4.18[f]	3.88[e], 3.89[f]	4.28[e], 4.27[f]	5.75[e], 5.75[f]	4.50[e], 4.50[f]	4.63[e], 4.63[f]

[a] from [145]; [b] from [149]; [c] from [148]; [d] from [150].
[e] diameter D, labeling probability p, aggregation number n and concentration c have been optimized simultaneously.
[f] D, n and c have been optimized simultaneously, p has been set to the nominal labeling degree.

Considerably more uncertainties are related to the obtained fit values for n and p as long as none of them can be independently determined to high precision. Already a small amount of free spin-label in the solution would affect p.[151] Furthermore, the literature values for n show a significant spread (Table 4). Therefore the values of these parameters extracted from both models should be taken only as rough estimates. Nevertheless, the analysis based on both of our models yields micelle properties which are in reasonable agreement with values obtained by luminescence quenching,[149] sedimentation techniques,[145] small angle X-ray scattering,[148] and positron lifetime spectroscopy.[150]

Our results clearly show, that in micellar systems PELDOR time traces with a distinct initial decay are not a decisive indication of a specific aggregate but a result of the finite size of the micelle. In extreme cases, even the observation of a dipolar modulation, as present in the simulations using the surface model, might be caused by size restriction effects rather than specific interactions.[152] This might be important for the study of homo-oligomeric systems, such as lipophilic peptides or membrane proteins in detergent micelles, were such PELDOR signals could be easily misinterpreted to represent structural information on the macromolecular complex itself. As we have shown here, a signal deviating from a stretched exponential alone does not allow discriminating between specific and unspecific clustering. The assumption, that the observed dipolar interaction represents a specific interaction and not statistical segregation into the micelles will have to be confirmed by further evidence. Wherever possible a system in which the desired specific interaction has been switched off by design (the 'singly-labeled' reference) should be measured. Through this control the unspecific PELDOR background function could be identified. The observation of significant differences between the sample and its control will allow relevant structural conclusions. In general, it seems unlikely to solve the problem of the background theoretically without utilizing a 'singly-labeled' reference sample. Obviously, the solution to this problem is not trivial. In principle, the singly-labeled reference can be obtained by cross-linking the oligomer under study and expressing it as a single polypeptide chain that only contains a single cysteine residue. This sample could act as singly-labeled reference. However, such a construct might not always be feasible. On the other hand, lowering the local concentration of spin-labeled molecules by decreasing their overall concentration can be used to test if size restriction effects blur the analysis of specific interactions by PELDOR. If the oligomer under study exhibits strong binding and the monomers do not exchange, the multiply-labeled oligomer could be diluted with unlabeled oligomer to achieve a similar effect.

3.3. Regulation of the Dynamics of the Toc34 GTPase Homodimer by Nucleotides and Substrates

3.3.1. Introduction

According to the current experimental evidences Toc34 is the preprotein receptor of the TOC complex (see section 2.1 for more details). Comparison of the GDP and the GTP form

of Toc34 revealed only marginal conformational differences in the crystal structures[15,39] -an unexpected observation as structural changes of G-proteins are typically the mode of signal transmission. Here the structural flexibility of the *ps*Toc34 G-domain dimer in fast-frozen solution is analyzed by PELDOR.

Samples were prepared in collaboration with the group of Prof. Enrico Schleiff. Samples for X-band (200 µl with 160-200 µM) and Q-band (5-10 µl) were transferred to standard 4 and 1.6 mm outer diameter EPR tubes, respectively. The samples were shock-frozen in liquid nitrogen. In these experiments we utilized the neck-coiled-coil of Kinesin-1 (*dm*KHC) from *Drosophila melanogaster* that is fused to the G-domain of *ps*Toc34 via a non-coiled-coil-forming spacer. In this construct the C-termini of the two monomers are linked by zipper formation, which likely reflects the native condition where the C-terminus is anchored to the membrane. Two single-Cys mutants were prepared (M79C and K143C; Figure 22). The two mutants show only a slightly higher K_M and k_{cat} (< 5 fold) of multiple turnover GTP hydrolysis when compared to wild-type (Appendix E), which confirms the functionality of the mutants. As a control, one additional monomeric mutant was created with cysteines at both ends of helix α5 (D175C/S191C; Figure 22) containing an arginine 133 to alanine substitution reducing the affinity for homodimerization.[45,53]
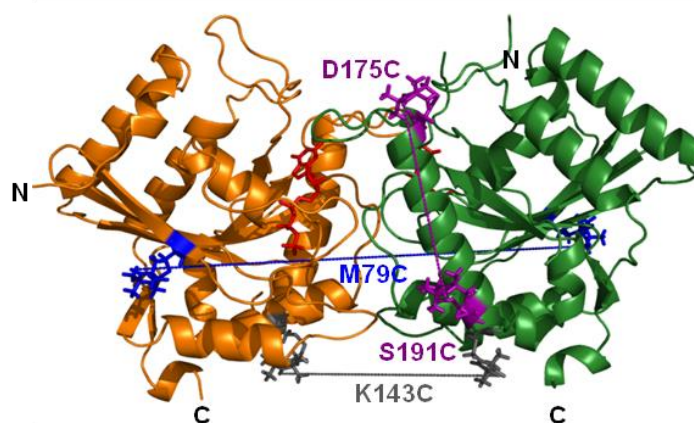
Figure 22. Dimeric G-domains of *ps*Toc34 (PDB code 3bb1) indicating the positions of the cysteines introduced for PELDOR. The R133A/D175C/S191C double-Cys mutant is monomeric.

3.3.2. Effect of the Nucleotide Loading State

We measured a distance of 27±5 Å by PELDOR on the monomeric R133A/D175C/S191C sample irrespective of the nucleotide loading state (Figure 23; Table 5), which is in agreement

with the distance in the structure proving that R133 is essential for homodimer formation. For K143C$_{GDP}$ we measured a distance of 28±5 Å for ~70% of the population, which agrees well with the proposed dimeric conformation based on the X-ray structure (Figure 24; Table 5). For ~30% of the population we observed a broad longer distance (49±11 Å) than expected from the crystal structure. This might be either due to a second conformation of the dimer or monomeric population that is kept together by the zipper. By Q-band (33.7 GHz) PELDOR using an 80 MHz shaped pump pulse,[153] for M79C$_{GDP}$ two populations with distances 64±2 Å (65%) and 78±2 Å (35%) have been found (Figure 25; Table 5). This is in agreement with the dimeric crystal structure and confirms that the monomers are not arranged "back to back". We also explored the nucleotide dependence of the conformational freedom of the homodimer by loading *ps*Toc34 K143C with either GMP-PNP or aluminum fluoride and GDP (GDP-AlF$_x$ mimicking the transition state of GTP hydrolysis). For the GDP-AlF$_x$-loaded protein a similar PELDOR trace as for the GDP-loaded protein is observed (Figure 24), but the conformation with the distance comparable to the X-ray structure is less populated. The GMP-PNP-loaded protein showed a broad distance distribution which corresponds to a distance of 49±26 Å. This might suggest that the γ-phosphate of GMP-PNP induces intramolecular changes favoring a high conformational flexibility of the dimer. Taken together, the results suggest that the nucleotides modulate the equilibrium between different conformations of the homodimer of Toc34.
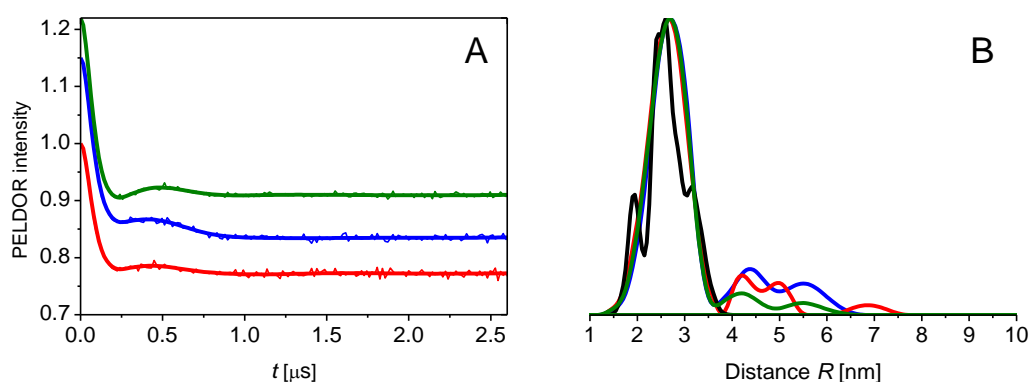
Figure 23. PELDOR on monomeric *ps*Toc34 R133A/D175C/S191C; (*a*) The background-corrected PELDOR time traces and (*b*) obtained distance distributions from Tikhonov regularization on different nucleotide bound states: (green) GDP, (blue) GDP-AlF$_x$, (red) GMP-PNP; (black) the simulation based on X-ray structure (PDB code 3bb1).
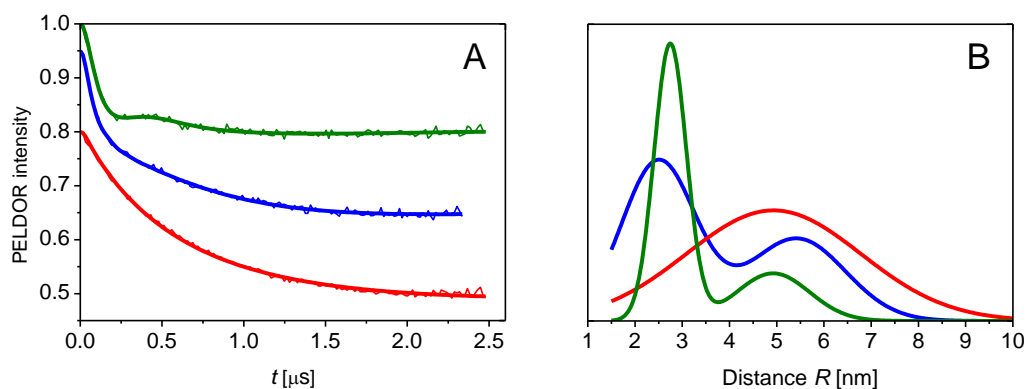
Figure 24. Effect of the nucleotide loading state; (*a*) The background-corrected PELDOR time traces and (*b*) obtained distance distributions by Gaussian model fitting on different nucleotide bound states of *ps*Toc34 K143C: (green) GDP, (blue) GDP-AlF$_x$, (red) GMP-PNP.
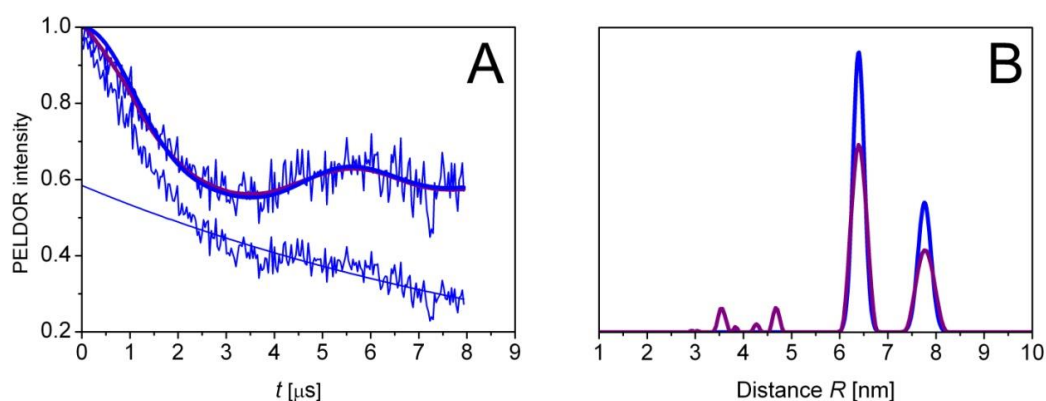
Figure 25. (*a*) The primary and background-corrected PELDOR time traces for *ps*Toc34 M79C$_{GDP}$ and (*b*) obtained distance distributions by Gaussian model fitting (blue) and Tikhonov regularization (purple).

3.3.3. Nucleotide-Dependent Effect of the Transit Peptide

Toc34 is discussed to be a receptor for incoming preproteins.[22] Thus, we analyzed the influence of a small 28 amino acid long peptide comprising the C-terminal portion of the transit of the small subunit of Rubisco[44] on the structure and dynamics of the homodimer. By PELDOR measurements we observed a reduction of the dimeric population in the more closed conformation for GDP-loaded *ps*Toc34 K143C (Figure 26A). In turn, peptide addition to the receptor preloaded with GDP-AlF$_x$ shifted the equilibrium towards the more closed state (Figure 26B; Table 5). In the GMP-PNP-loaded state, the distance distribution is still broad as seen in the absence of the peptide and thus, due to the high conformational flexibility of this state significant conformational change cannot be detected (Figure 26C).

59
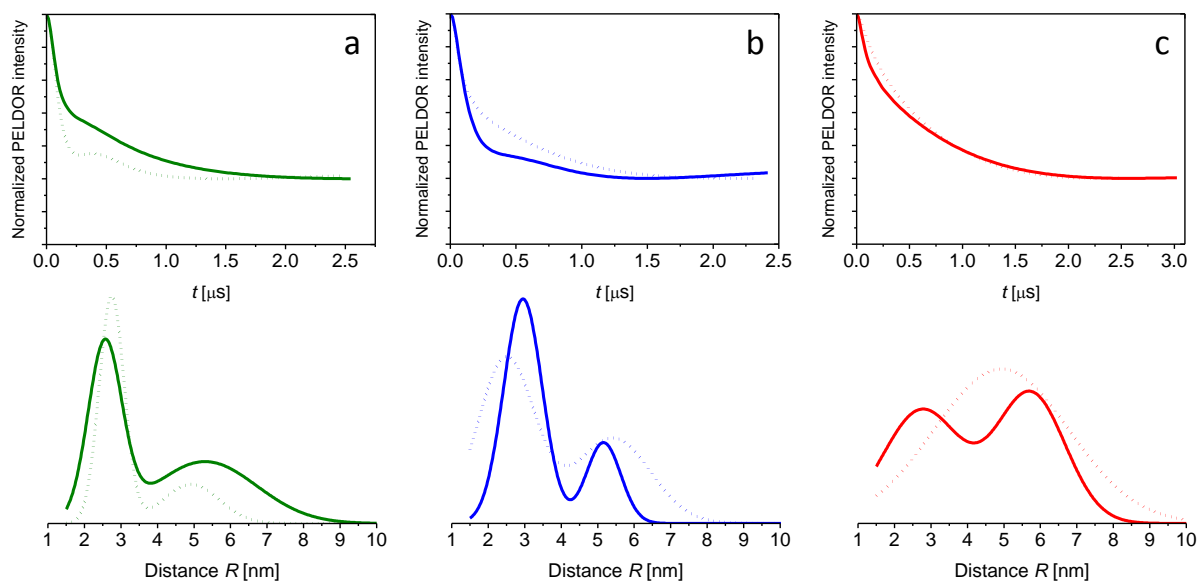
Figure 26. Nucleotide-dependent effect of the transit peptide; One or two Gaussian model fits to the background-corrected PELDOR time traces and the corresponding distance distributions for *ps*Toc34 K143C (100 µM dimer) loaded with: (*a*) GDP; (*b*) GDP-AlF$_x$; (*c*) GMP-PNP, in the absence (dotted line) or presence (solid line) of 1 mM transit peptide. For comparison, the PELDOR time traces are scaled to a same modulation depth.

Table 5. Obtained distance information by PELDOR on *ps*Toc34 samples.

Mutant	Distance predicted[a] (Å)	Nucleotide	PELDOR (Å) (%)[b]	
			Population I	Population II
R133A/D175C/S191C	26	GDP	27±5	–
		GDP-AlF$_x$	27±5	–
		GMP-PNP	27±5	–
M79C	64	GDP	64±2 (65)	78±2 (35)
K143C	27	GDP	28±5 (72)	49±11 (28)
		GDP-AlF$_x$	25±11 (57)	54±15 (43)
		GMP-PNP	–	49±26 (100)
K143C+TP	27	GDP	26±7 (48)	53±20 (52)
		GDP-AlF$_x$	30±8 (76)	52±7 (24)
		GMP-PNP	28±15 (46)	57±13 (54)

[a] from rotamer library simulations; [b] given is the distance as mean ± SD (standard deviation) and the percentage of molecules representing this population.

3.3.4. Discussion

Dimeric GTPases are involved in multiple essential cellular processes. It is discussed that dimerization is essential for the regulation of the GTPase cycle and can replace the need for a GAP.[28] For the GTPase Toc34, which dimerizes in context of the TOC complex (Figures 2 and 22), homodimerization is thought to regulate nucleotide exchange as consequence of the positioning of the nucleotide binding site at the dimerization interface.[16,39,63] The regulation of Toc34, however, is largely unexplored as most previous studies concentrated on the monomeric receptor form as the K_D for homodimerization of the isolated G-domain is in the range of 100 µM.[48] To stabilize the dimeric conformation for our experiments we used a C-terminal zipper tethering the soluble G-domains together.

We used PELDOR measurements to describe structural changes and observed distinct conformational states of the Toc34 homodimer (Figures 24 and 26). We observed a tight conformation, e.g. for the GDP-loaded receptor, which is consistent with the proposed GDI function of dimerization.[63] A relaxed conformation was induced after addition of TP to the GDP-loaded receptor (Figure 26A; Table 5). This observed opening finally proofs the previous suggestion that Toc34 dimerization is regulated by its substrate.[63] Remarkably, the dimeric GDP state shows a very fast kinetics for the TP recognition, and the observed K_D for TP binding to the dimer is with 5 µM more than a magnitude lower than for the monomeric receptor (K_D = 90 µM).[154] This would suggest that a dimeric conformation of Toc34 rather than the monomeric protein serves as receptor for the incoming preprotein. For the GMPPNP-loaded receptor we observed a long broad distance distribution by PELDOR. In the absence of the substrate, the receptor at transition (GDP-AlFx) state is in a more closed conformation. However, this is less pronounced than seen for the GDP-loaded receptor. Accordingly, fluorescence anisotropy measurement using fluorescent-labeled transit peptide shows that the transition state has a reduced binding rate compared with the GDP- or GMP-PNP-loaded state (data not shown).

We conclude that the nucleotide loading state enforces a different dynamics of the dimer, which in turn is altered upon addition of the peptide mimicking a substrate of Toc34. As crystallization of Toc34 revealed almost identical dimeric conformations for the GDP- and GTP-loaded state,[39] one might speculate that only one conformation was crystallized, which should to be challenged in future with extensive crystallization trials.

Transferred to the native system one could extract the following model: The transit peptide is recognized by the Toc34 dimer tethered by its membrane anchor to stimulate nucleotide exchange. The intrinsic GTPase activity of Toc34[51] argues for a GDP-loaded ground state of dimeric Toc34 in the context of the TOC complex (Figure 27, step 1), which most likely recognizes incoming preproteins (step 2). The preprotein-induced opening of the dimer (step 2) would induce nucleotide exchange (step 3) and the occurring monomer might subsequently interact with another component of the TOC complex (step 4). Indeed, it was suggested that GTP-loaded monomeric Toc34 possesses enhanced affinity for Toc159 in the presence of the transit peptide.[44]
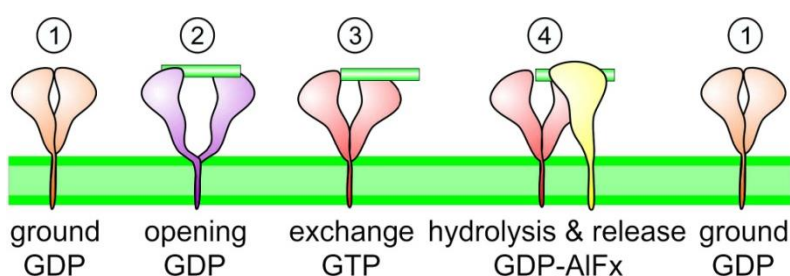
Figure 27. The model for the interdependency of substrate binding and nucleotide-dependent dimerization of Toc34; the conformations are visualized for the different molecular events during preprotein recognition and transfer (preprotein: green). An additional interaction partner within TOC is indicated in yellow. Nucleotide loading is given below. Please note, the GTP state in the absence of peptide is not considered in the physiological model.

3.4. Conformational Flexibility and Relative Orientation of the POTRA Domains of *Anabaena* Omp85 by PELDOR Spectroscopy

3.4.1. Introduction

The structure of the N-terminal POTRA domains has been solved for Omp85 from *Anabaena sp.* PCC 7120.[17] Molecular dynamics (MD) simulations predicted a rather rigid conformation between the P2-P3 domains, consistent with a short connection and a large interface between domains observed in the X-ray structure (PDB code 3mc8).[17] The analysis showed that there is a flexible hinge between P1 and P2. Two dominant conformations were observed for P1-P2 in MD simulations; and one (MD1) is close to the crystal structure.

Therefore as it was shown before,[10] studying the dynamics within the N-terminal domain of cyanobacterial Omp85 using available spectroscopic techniques such as PELDOR is crucial for evaluation of the previous structural and molecular dynamics analyses. In addition, Modeller- and elastic network model-based fitting can be used to refine a known structure using a set of spin label distance constraints obtained by PELDOR.[93,95,155] Assuming protein domain structures as rigid body will help to overcome the sparsity of the constraints. In this study we used site-directed spin labeling (SDSL) to covalently attach two spin labels (MTSSL spin labels in this study) in order to investigate the relative orientation and conformational flexibility between POTRA domains of *Anabaena* Omp85 by PELDOR spectroscopy (Figure 28).
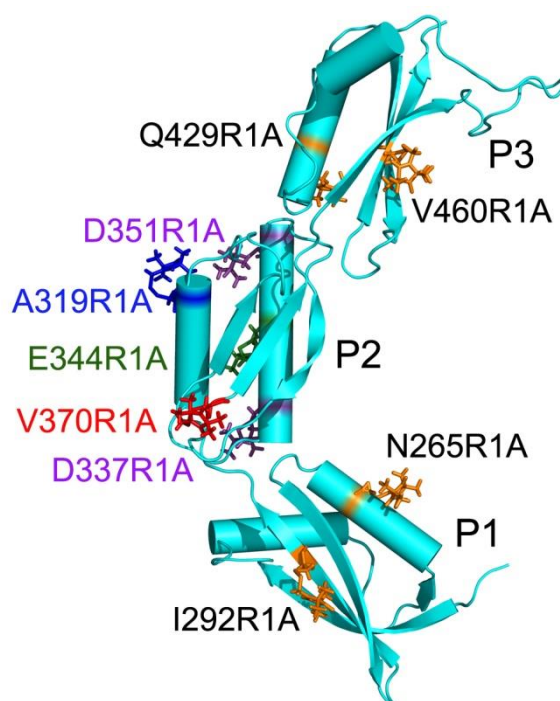
Figure 28. Structure of the N-terminal POTRA domains of *Anabaena* Omp85 (PDB code 3mc8) showing the locations selected for introduction of nitroxide side chains.

3.4.2. Available Cysteine Mutants and Control PELDOR Experiments

A construct consists of the soluble fragment of the N-terminal periplasmic domain of *Anabaena sp.* PCC 7120 (residues 161 to 465), similar to the one that was crystallized,[17] was utilized in this study. 12 double-Cys mutants between P1-P2 and P2-P3, and one long-distance mutant between P1-P3 were prepared, spin-labeled with MTSSL, and measured
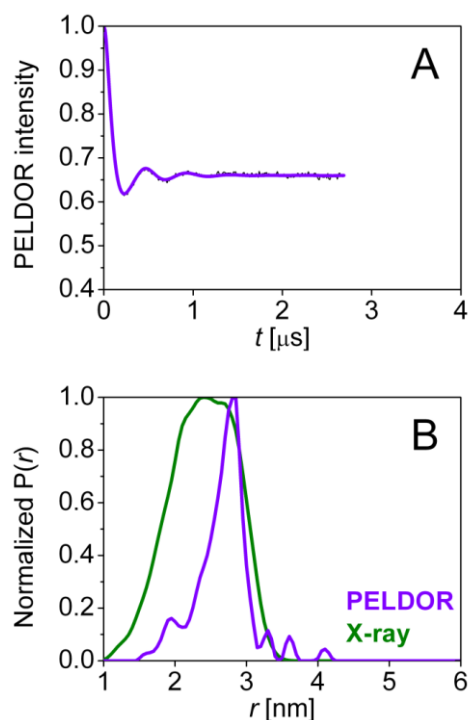
Figure 29. (A) The background-corrected PELDOR time trace for the control mutant D337C/D351C at both ends of helix α_2 in P2 with fit from Tikhonov regularization, (B) obtained distance distribution by Tikhonov regularization compared with X-ray structure.

(Figure 28). In addition to these interdomain mutants, five additional control mutants within P2 (A319C/E344C; A319C/D337C; D337C/D351C; V370C), and P3 (Q429C/V460C) were prepared. Three of these control mutants (A319C/E344C, A319C/D337C, and Q429C/V460C) assist analyzing the structural dynamics within individual domains, and the other two mutants in P2 (D337C/D351C; V370C) were to test the interaction of N-terminal domains under the circumstances utilized in this study. PELDOR measurement on D337C/D351C at both ends of the helix $\alpha2$ showed a narrow distance distribution with the average distance corresponding to the predicted one (Figure 29); in addition, PELDOR on the single-Cys mutant V370C was mainly an exponential background due to random intermolecular interactions (not shown).[1] Therefore a monomeric behavior of the N-terminal domains can be concluded. In addition, using I292C/V370C double-Cys mutant no significant change in the average distance was observed under different buffer conditions (pH 6–8, 125–500mM NaCl, and different hydrophobic or hydrophilic cryoprotectants) and freezing procedures (Figure 30). Also, for most of the PELDOR measurements on the intra-domain double mutants the corresponding distances based on X-ray structure can be obtained that

prove the well-defined structure of the individual POTRA domains as well as suitable prediction of the spin label conformation on most of these sites (Figures 31 and 32; Table 6).
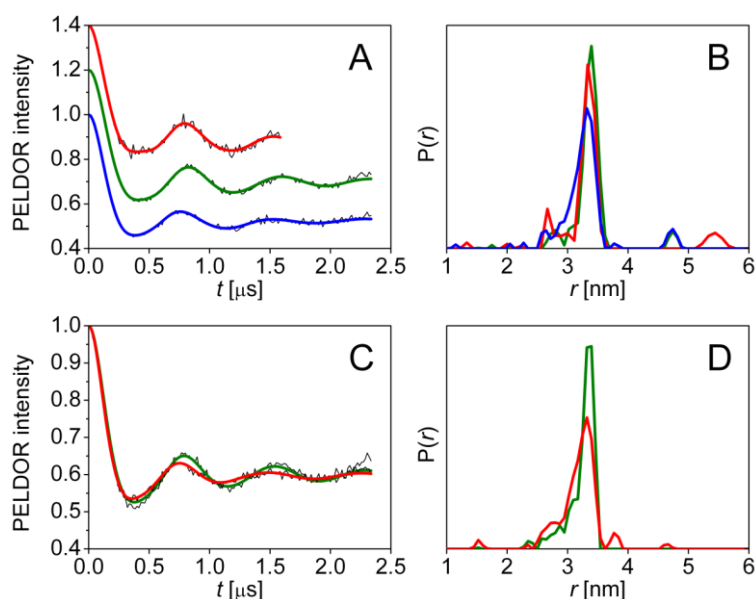
Figure 30. Effect of different cryoprotectants and freezing procedures on PELDOR measurements using I292C/V370C double-Cys mutant. The background-corrected PELDOR time traces and obtained distance distributions for different hydrophobic or hydrophilic cryoprotectants (A and B): 30% DMSO (red, 3.3±0.2 nm), 30% ethylene glycol (green, 3.4±0.2 nm), 25% Ficoll 70 (blue, 3.3±0.3 nm). The background-corrected PELDOR time traces and obtained distance distributions for fast freezing of the samples by freeze-quench technique (C and D): with 30% glycerol (green, 3.2±0.2 nm), without glycerol (red, 3.2±0.4 nm). Likewise, no change was observed for different pH values (6–8, 3.3±0.2 nm), and ionic strength (125–500mM NaCl, 3.3±0.2 nm).

3.4.3. PELDOR on POTRA Domains
and Comparison with X-ray and MD Structures

Majority of the PELDOR time traces between different POTRA domains show pronounced dipolar oscillations, indicating a rather rigid structure (Figure 31). For P1-P2, these results are different from MD predictions. For PELDOR measurements between P2 and P3, predicted distance distributions based on X-ray structure with a rotamer library of MTSSL spin labels (with steric restrictions)[92] and experimental distance distributions derived by Tikhonov regularization show good agreement (Figure 32). Since structural refinement of the X-ray structure using the PELDOR distance constraints depends on the proper prediction of the spin label conformation, we also compared the MMM-based distributions to another modeling

approach that does not include Boltzmann weighting of spin label rotamers but only removal of clashing conformations.[156] Both methods predicted the same distance distributions (Figure 32). There is also acceptable agreement between experimental distributions and the ones predicted on the representative MD-based structure (Figure 33). Therefore the relative orientation between P2 and P3 is in good agreement with the structure determined by X-ray,
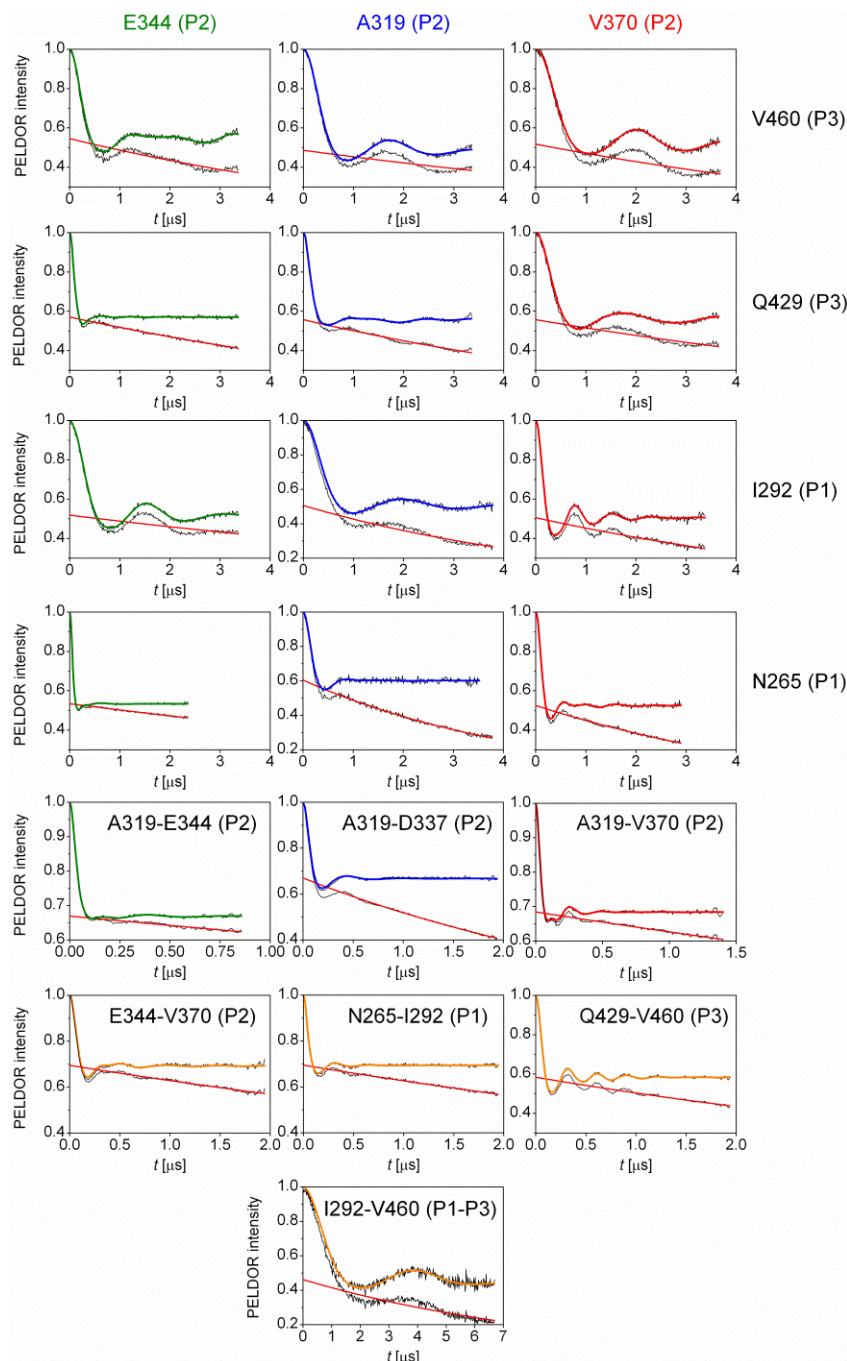
Figure 31. The primary and background-corrected PELDOR time traces for measurements on POTRA domains with fits from Tikhonov regularization.

and compatible with the MD simulations suggesting a rather fixed orientation between these domains. On the other hand, the shift in the average distances between P1 and P2 compared with X-ray structure as well as the dominant conformation from MD reflects a different orientation of these domains (Figure 32; Table 6).
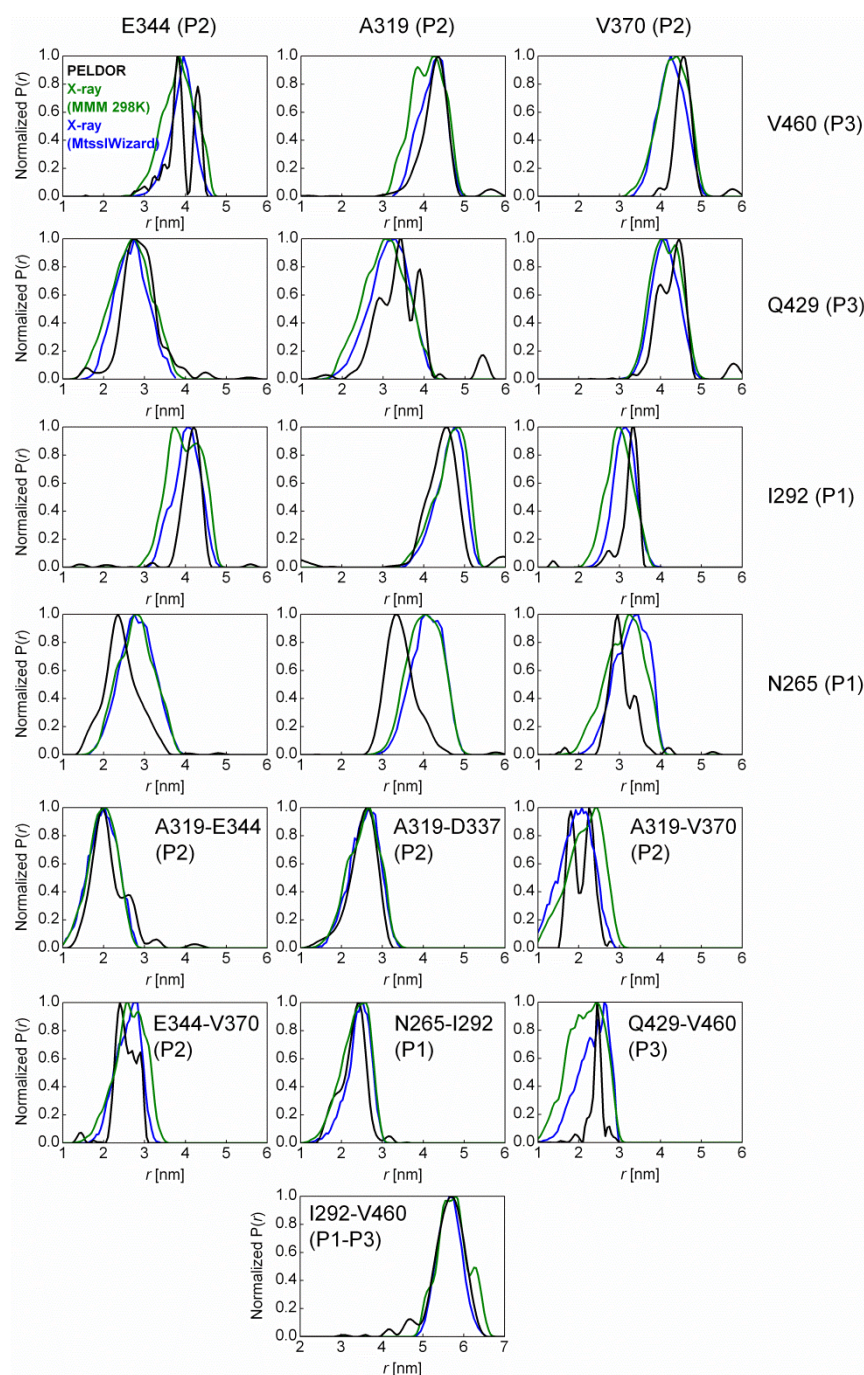
Figure 32. Obtained experimental distance distributions by Tikhonov regularization (black) compared with distance distributions generated on X-ray structure by MMM in 298 K mode (green), and mtsslWizard using a vdW cutoff of 1.5 Å, non-clashing normal search (blue).

3.4.4. Modeling the Relative Orientation of POTRA Domains Using Long-Distance Constraints

The X-ray structure of POTRA domains was refined in two iterations using a modified version of Modeller 9.10[93] which modified variables are included in and taken from MMM 2011.2 software package.[92] The rotamer ensemble was first calculated at 298K (or 175K) on the spin-labeled positions. A rotamer which best fits the mean N-O midpoint position of the whole ensemble was attached to the template structure that was supplied to Modeller. The X-ray structure was refined using the PELDOR peak distances (very similar to average distances) listed in Table 6. Individual POTRA domain structures were also considered as

Table 6. Comparison of PELDOR distance constraints with X-ray structure and the refined model

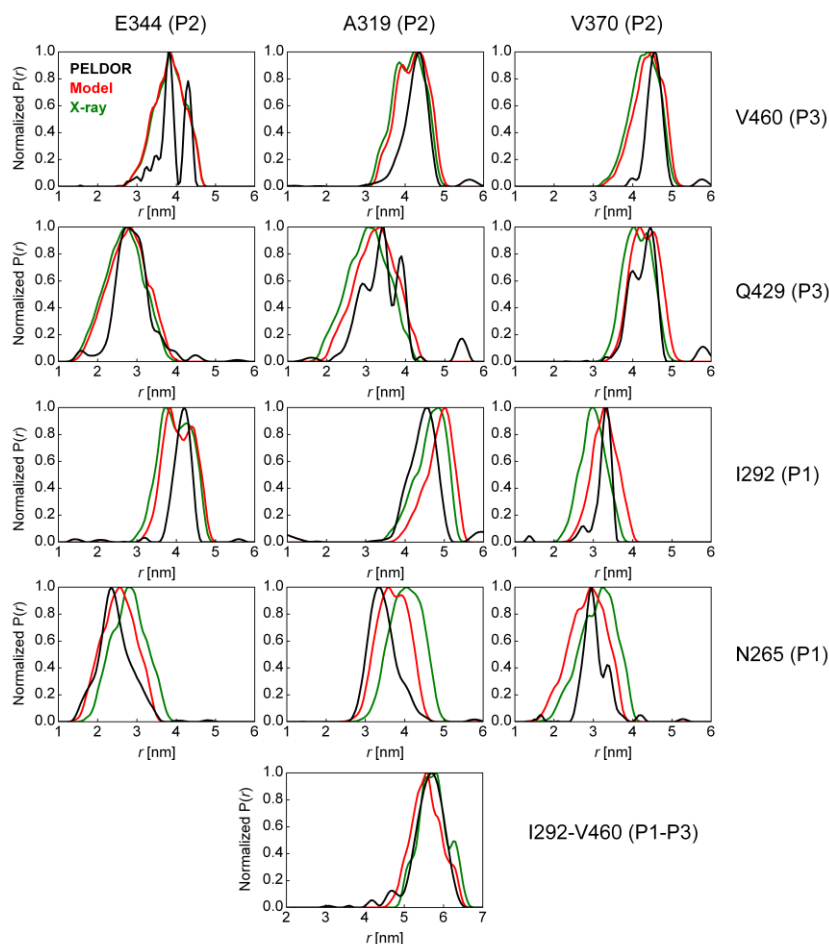| Pair	$<r>_{PELDOR}/r_{pk}$ [a,b]	$<r>_{X\text{-ray}}$ [a,c]	$<r>_{Modeller\text{-refined}}$ [a,c]
P1-P2			
I292-A319	4.5/4.6 (0.5)	4.6 (0.4)	4.9 (0.4)
I292-E344	4.2/4.2 (0.3)	4.0 (0.4)	4.1 (0.4)
I292-V370	3.3/3.4 (0.2)	3.0 (0.3)	3.3 (0.3)
N265-A319	3.5/3.4 (0.4)	4.0 (0.4)	3.7 (0.4)
N265-E344	2.3/2.4 (0.4)	2.8 (0.4)	2.5 (0.4)
N265-V370	3.0/3.0 (0.4)	3.1 (0.5)	2.8 (0.5)
P2-P3			
V460-A319	4.4/4.4 (0.3)	4.1 (0.4)	4.2 (0.4)
V460-E344	3.9/3.8,4.3 (0.5)	3.8 (0.4)	3.8 (0.4)
V460-V370	4.6/4.6 (0.2)	4.3 (0.4)	4.4 (0.4)
Q429-A319	3.4/3.4 (0.6)	3.1 (0.5)	3.2 (0.5)
Q429-E344	2.9/2.8 (0.5)	2.7 (0.5)	2.8 (0.5)
Q429-V370	4.3/4.5 (0.4)	4.1 (0.4)	4.3 (0.3)
P1-P3			
V460-I292	5.7/5.7 (0.6)	5.7 (0.4)	5.6 (0.4)
P1			
N265C-I292C	2.3/2.4 (0.3)	2.3 (0.4)	–
P2			
A319-E344	2.1/2.0 (0.5)	2.0 (0.3)	–
A319-D337	2.5/2.6 (0.4)	2.5 (0.4)	–
A319-V370	2.1/2.3(0.2),1.8(0.2)	2.1 (0.4)	–
E344-V370	2.5/2.4 (0.4)	2.6 (0.4)	–
P3			
Q429-V460	2.4/2.4 (0.1)	2.2 (0.4)	–

[a] Distances in nm; $<r>/r_{pk}$ are mean/peak distances; the standard deviations are given in parentheses.
[b] PELDOR distances are obtained by Tikhonov regularization.
[c] Distances are predicted by MMM in 298 K mode.

rigid body with flexible hinges between them (centered on V298 and G378); since the intradomain PELDOR measurements proved their well-defined structures. This assumption will help to overcome the scarcity of distance constraints.

For the majority of cases the predicted average distances on the refined structure are in good agreement with experimental ones (Figure 34; Table 6). To compare the relative orientation of adjacent POTRA domains from different structures, Euler angles and position displacements between domains are calculated (Table 7). In order to define the right-handed coordinate systems on individual POTRA domains, three C_α coordinates are selected (two residues at both ends of strand β_3 and the central residue of helix α_2):
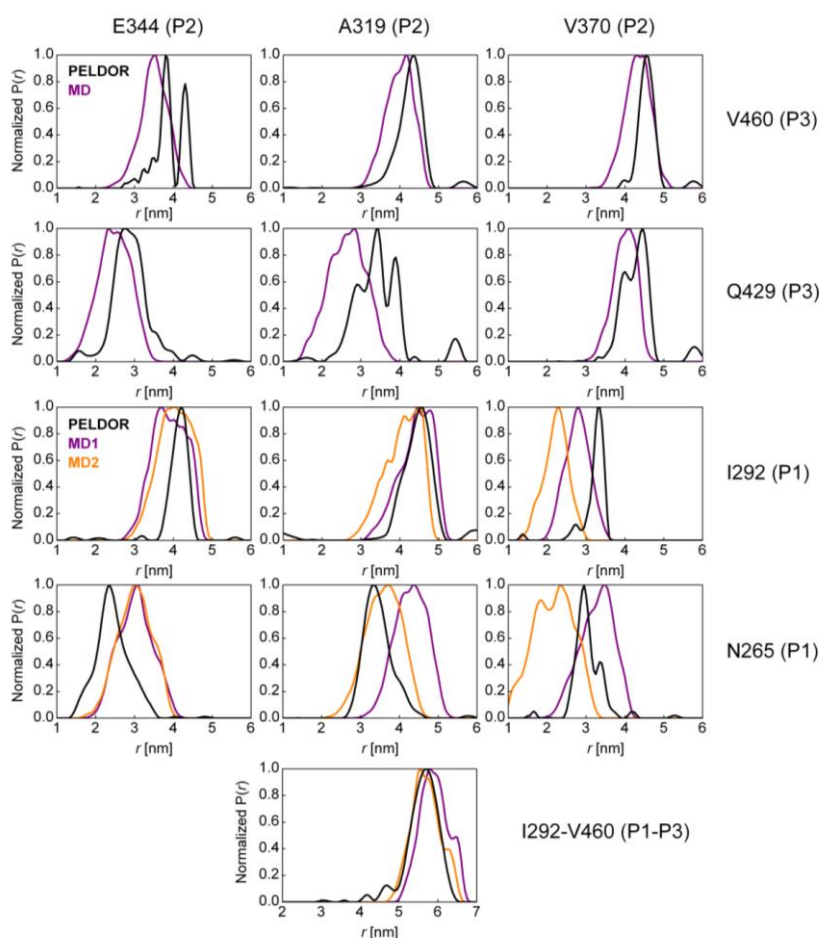
Figure 33. Obtained experimental distance distributions by Tikhonov regularization (black) compared with dominant structures from MD simulations. For MD structures, individual POTRA domains are superimposed and replaced with the respective POTRA domains from the X-ray before generation of distance distributions. Distance distributions are generated by MMM software package in 298 K mode.

POTRA1: G286 (β_3), P295 (β_3), E262 and D263 (α_2; midpoint of the C_α coordinates)

POTRA2: V370 (β_3), A376 (β_3), K343 (α_2)

POTRA3: V457 (β_3), E465 (β_3), K430 and D431 (α_2; midpoint of the C_α coordinates)

Figure 34. Obtained experimental distance distributions by Tikhonov regularization (black) compared with X-ray structure (green), and refined structure (red). Distance distributions are generated by MMM software package in 298 K mode.

For the MD and ENM-refined structures individual POTRA domains are superimposed and replaced with the respective POTRA domains from the X-ray. Then two orthogonal unit vectors are defined in the plain of these three C_α coordinates and taken as x and y directions (Figure 35). The 3×3 transformation matrix of the subsequent POTRA domain is derived in the coordinate system of the preceding one and the three Euler angles (α, β, γ) are calculated from that.

The r.m.s.d. of the refined structure from the X-ray for P1–P2 and P2–P3, is 2.2 and 0.7 Å, respectively. In the refined structure, P1 and P2 are more inclined towards each other compared with the X-ray structure (Figure 36A). The relative orientation of the P2-P3 is also slightly different but its amplitude is much smaller compared with P1-P2 (Figure 36A; Table 7). Consistently, two dominant conformations between P1-P2 predicted by MD studies[17]
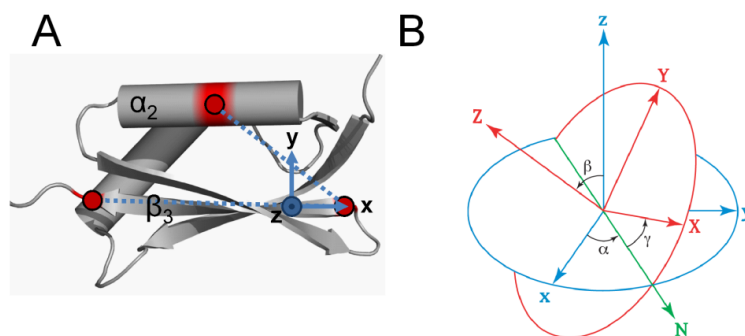
Figure 35. Right-handed coordinate system defined on individual POTRA domains (A), and Euler angles (B).
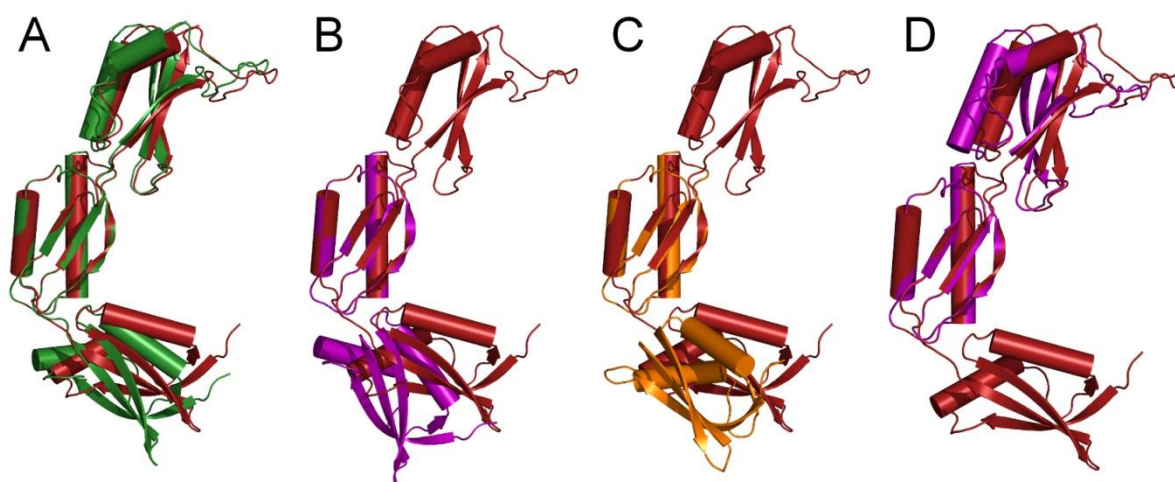
Figure 36. Superimposition at P2 of the Modeller-refined structure (dark red) and: (A) X-ray structure (r.m.s.d. for P1–P2 and P2–P3, 2.2 and 0.7 Å, respectively), (B) Dominant MD structure 1 for P1–P2 (MD1$_{P1-P2}$), (C) Dominant MD structure 2 for P1–P2 (MD2$_{P1-P2}$), (D) MD$_{P2-P3}$.

do not agree with PELDOR refined structure (Figure 36B,C; Table 7). Although for few distance constraints between P2 and P3 the deviation from the dominant conformation from MD is significant (Figure 33) but the PELDOR-refined structure of P2-P3 is in acceptable agreement with the MD structure (Table 7; Figure 36D).

Elastic Network Model (ENM)-[94, 95] and Modeller-based[155] models are rather similar (r.m.s.d. of 1.6 Å; Figure 37). Therefore different fitting approaches and parameters (rotamer ensemble predicted by MMM in 175 and 298 K modes) generate similar refined structures (Figure 37; Tables 8 and 9).

Table 7. Euler angles and displacements between POTRA domains from different cyano- and proteobacteria determined from structures

Structure	α	β	γ	ΔR_x [a]	ΔR_y [a]	ΔR_z [a]
*ana*Omp85 (P1-P2)						
X-ray (3mc8)	-71	-42	29	30.8	5.6	-27.7
Modeller-refined	-75	-40	112	30.9	-3.9	-28.8
MD1	-54	-36	-16	27.0	15.8	-26.8
MD2	-117	-39	-70	34.1	10.9	-3.9
*ana*Omp85 (P2-P3)						
X-ray (3mc8)	66	-5	-20	2.1	29.3	-4.7
Modeller-refined	68	-5	-23	1.9	30.1	-2.8
MD	77	-17	-20	3.2	28.2	-3.8
*Te*Omp85 (2x8x)						
P1-P2	-52	-35	2	–	–	–
P2-P3	55	4	-23	–	–	–
FhaC (2qdz)	48	-7	-18	–	–	–
BamA (3efc)						
P1-P2	-22	-19	-34	–	–	–
P2-P3	-105	-27	-47	–	–	–
P3-P4	-79	-19	118	–	–	–
P4-P5 (3og5)	-76	-32	111	–	–	–
BamA (2qdf)						
P1-P2	-14	-13	-31	–	–	–
P2-P3	-77	-28	128	–	–	–
P3-P4	-80	-19	117	–	–	–

[a] x,y,z components of the connecting vector of the coordinate systems on adjacent domains.

3.4.5. Implications of the PELDOR Results for the Functions of POTRA Domains

In this study the observation of restricted relative orientation of cyanobacterial POTRA domains might have significant implications for the possible binding of the POTRA domains to unfolded outer-membrane proteins. This is in line with previous structural and spectroscopic studies on POTRA domains of BamA from *E. coli* that revealed two rigid parts connected by a flexible linker[10,73,76] with the C-terminal one as the essential part for the

function.[77] Interestingly, comparison of relative orientation of cyano- and proteobacterial POTRA domains using Euler angles (Table 7) revealed that there is a small degree of freedom
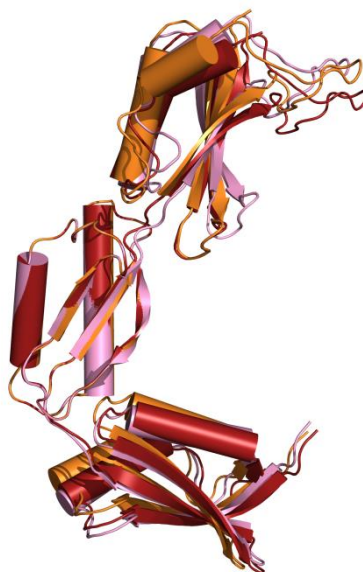
Figure 37. Alignment of structures refined by different approaches and fitting parameters: Modeller-refined structure (MMM 298 K, two iterations; dark red), Modeller-refined structure (MMM 175 K, three iterations; pink), ENM-refined structure (MMM 298K; orange). Structures are superimposed at P2.

in angle β that determines the twist between adjacent domains compared with other two angles. This might indicate that the unfolded protein could interact with adjacent POTRA domains simultaneously. Since the continuity of interaction sites on POTRA domains exerts a limitation on the possible twist angles but different α and γ angles can be tolerated. This is in agreement with previous substrate interaction studies on POTRA domains of FhaC[79] and BamA.[75] Thus the relative orientation of the structural elements involved in the interaction is important for the processive sliding of the substrate toward the membrane.[75]

The relative orientation of the refined *Anabaena* Omp85 P1-P2 is similar to that of the last three *E. coli* BamA POTRA domains (P3-P5) as well as P2-P3 orientation of the "bent" X-ray structure (PDB code 2qdf; Table 7). *Anabaena* P1 and P2 were proposed to be reminiscent of BamA P2 and P3 that are connected by a flexible linker.[17] However, the rigid architecture of the cyanobacterial POTRA domains revealed by PELDOR is reminiscent of the C-terminal proteobacterial POTRA domains P3-P5.[76] Therefore we would like to hypothesize that cyanobacterial POTRA domains P1-P3 might correspond to the proteobacterial rigid POTRA domains P3-P5.

73

Table 8. Comparison of distance information from structures refined by different approaches

Pair	$\langle r\rangle$_Modeller-refined [a,b]	$\langle r\rangle$_Modeller-refined [a,c]	$\langle r\rangle$_ENM-refined [a,d]
P1-P2			
I292-A319	4.9 (0.4)	4.9 (0.3)	4.7 (0.4)
I292-E344	4.1 (0.4)	4.0 (0.3)	3.9 (0.4)
I292-V370	3.3 (0.3)	3.2 (0.3)	3.2 (0.3)
N265-A319	3.7 (0.4)	3.6 (0.4)	3.7 (0.4)
N265-E344	2.5 (0.4)	2.3 (0.4)	2.4 (0.4)
N265-V370	2.8 (0.5)	2.6 (0.4)	3.0 (0.4)
P2-P3			
V460-A319	4.2 (0.4)	4.2 (0.4)	4.2 (0.4)
V460-E344	3.8 (0.4)	3.9 (0.3)	4.0 (0.4)
V460-V370	4.4 (0.4)	4.7 (0.4)	4.4 (0.4)
Q429-A319	3.2 (0.5)	2.9 (0.6)	3.3 (0.5)
Q429-E344	2.8 (0.5)	2.7 (0.4)	2.9 (0.5)
Q429-V370	4.3 (0.3)	4.3 (0.4)	4.3 (0.3)
P1-P3			
V460-I292	5.6 (0.4)	5.9 (0.3)	5.7 (0.4)

[a] Distances in nm; $\langle r\rangle$ is the mean distance; the standard deviations are given in parentheses.

[b] Distances are predicted by MMM in 298 K mode.

[c] Distances are predicted by MMM in 175 K mode.

[d] Elastic network model (ENM)-based refinement (MMM 298 K mode). For obtaining distance information, individual POTRA domains are superimposed and replaced with the respective POTRA domains from the X-ray.

Table 9. Euler angles and displacements[a] between *Anabaena* POTRA domains from structures refined by different approaches

Structure	α	β	γ	ΔR_x	ΔR_y	ΔR_z
*ana*Omp85 (P1-P2)						
Modeller-refined[b]	-75	-40	112	30.9	-3.9	-28.8
Modeller-refined[c]	-75	-39	116	29.6	-4.7	-30.6
ENM-refined[d]	-72	-40	104	27.9	-3.0	-31.8
*ana*Omp85 (P2-P3)						
Modeller-refined[b]	68	-5	-23	1.9	30.1	-2.8
Modeller-refined[c]	60	-11	-7	1.5	34.1	-3.2
ENM-refined[d]	68	3	-21	1.3	29.9	-5.1

[a] x,y,z components of the connecting vector of the coordinate systems on adjacent domains.

[b] Rotamer ensemble is predicted by MMM in 298 K mode.

[c] Rotamer ensemble is predicted by MMM in 175 K mode.

[d] Elastic network model (ENM)-based refinement (MMM 298 K mode). For obtaining Euler angles and displacements, individual POTRA domains are superimposed and replaced with the respective POTRA domains from the X-ray.

4. Conclusions and Perspectives

4.1. Optimization of T_m for PELDOR in Membranes

In this study, processes that are involved in echo dephasing of nitroxide spin labels in phospholipid membranes at 50 K were systematically investigated. In general, avoiding spin clustering and thus large instantaneous diffusion rates is the key step for the optimization of transversal relaxation of nitroxides in lipid membranes. By concentrating proteoliposomes, it is possible to recover the signal-to-noise sacrificed for low local concentrations, since T_m is virtually independent of spatial distribution of the vesicles. Only in these locally dilute samples is deuteration of lipids and buffer helpful. In addition, this study revealed that membrane composition and labeling position in the membrane can also affect T_m, either by promoting the segregation of spin-labeled species or by altering their exposure to matrix protons. Thus, if spin-labeled membrane proteins tend to segregate, then it seems that the optimization of the membrane composition, to decrease the introduced perturbation and subsequent segregation of spin-labeled species or by use of magnetically dilute samples,[105,109] is inevitable. Effects of other experimental parameters including temperature (<50 K), presence of oxygen, and cryoprotectant type are negligible under our conditions. By application of similar experiments to the proxyl-labeled membrane-incorporated peptide gramicidin A (in collaboration with the group of Prof. Harald Schwalbe), we further cross-validated the optimization procedure carried out for spin-labeled lipids and find that the optimization parameters are valid also for the membrane-embedded peptide gramicidin A. This finding further supports the usefulness of the investigation for the application to larger membrane proteins.

4.2. PELDOR Distance Measurements in Micelles

In this study, statistically partitioned spin-labeled molecules into detergent micelles have been investigated. The resulting PELDOR time-domain signals cannot be described with a stretched exponential decay function, as would be expected in homogeneous solutions or in lipid vesicle membranes, but could be quantitatively modeled based on the size of the micelles, their aggregation number, spin-label concentration and the spin-labeling degree. The

labeling degree p and aggregation number n showed a strong interdependence, thus, they could not be determined independently to high precision. On the other hand, the local concentration c and micelle diameter D could be determined rather accurately from the PELDOR data. A clear distinction between situations where the spin-labels are distributed homogeneously within the micelle or within a narrow spherical shell at the polar-apolar interface is not possible, as can be seen from our simulations with both models. Both models give satisfactory agreement with the experimental data, with slightly different best fit values for the micelle diameter D. In conclusion, we show very clear evidence that a PELDOR time-domain signal in detergent micelles differing form a stretched exponential is not sufficient to prove a specific interaction. This might obscure structural investigations on incorporated macromolecules or complexes. In such systems further evidence will have to be presented to ensure that the measured distance distribution is not related to such micellar size effects.

4.3. Dynamics of the Dimerizing GTPase Toc34

In this study, we suggest that the regulatory function of Toc34 is transmitted by substrate binding in contrast to *bona fide* G-proteins with conformational changes in direct response to their nucleotide loading state.[28] Consequently, the equilibrium between two conformational states could be interpreted as inherent flexibility of the GTP-binding motives in response to GTP's γ-phosphate as seen for other G-proteins of the TRAFAC class, like p21 Ras.[157] Structural analyses by NMR or EPR generally consider a more dynamic nature of the switch regions, e.g. as Ras proteins can occupy two different conformations in the GTP-bound state.[27] The considerable change from the closed to the open conformation of the Toc34 dimer was only observed in the presence of the substrate (Figure 26A). Interestingly, elongation factor G (a TRAFAC GTPase) shows no structural changes in the switch regions in the GTP[33] and GDP-bound state[158] unless it is bound to the ribosome,[159,160] indicating that its presence is required for the nucleotide-dependent switch of EF-G.[27] Thus, the structural dynamics of *bona fide* G-proteins induced by GTP hydrolysis is replaced by substrate-dependent dimer flexibility, which might present a general regulatory mode. This concept might even hold true for members of the SIMIBI superfamily. The cytoplasmic GTPase Xab1 is dimeric regardless of the bound nucleotide, and only small structural changes take place when the nucleotide is exchanged.[161] Thus, Xab1 might be regulated by a similar mechanism as the Toc34 homodimer, which is different from the dimerization-dependent

switch mechanism known from SRP/SR.[161] In turn, the dimerization-dependent switch mechanism known from SRP/SR might be relevant for the regulation of the Toc34/Toc159 heterodimer. Thus, within the TOC reaction cycle the regulatory mode described in here and the dimerization-dependent switch mechanism might act in concert.

One important issue concerning Toc34 homo/heterodimer is monitoring the potential switch movements in a protomer. As the first attempt, this issue will be investigated by labeling two positions in Toc34 (leucine zipper construct) and probing the possible intramolecular conformational changes upon binding to unlabeled Toc34 or Toc159, in the presence or absence of other factors like Toc75 POTRA domains and substrate. Some available positions are (Figure 38): D175–E99, D175–S66, D175–Q71, and Y102–S66.
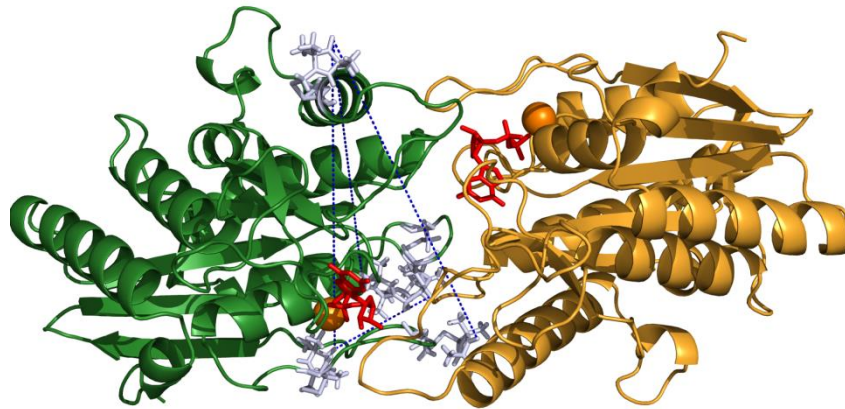
Figure 38. Dimeric G-domains of *ps*Toc34 (PDB code 1h65) indicating the positions of the cysteines introduced for intra-protomer PELDOR measurements. GDP (red), Mg^{2+} (orange).

In addition, by PELDOR distance constraints, the structure of *ps*Toc34-*ps*Toc159 G domain heterodimer will be probed in different nucleotide and peptide binding states.

4.4. Flexibility and Relative Orientation of POTRA Domains by PELDOR

The PELDOR distances measured between the P2 and P3 POTRA domains are in agreement with the structure determined by X-ray, and compatible with the MD simulations suggesting a fixed orientation between these domains. On the other hand, PELDOR constraints between the P1 and P2 POTRA domains implied a rather rigid structure with a different relative orientation of these domains compared with the X-ray and dominant conformations from MD. The difference from X-ray structure could be due to crystal packing

effects or effect of freezing on the PELDOR samples. The PELDOR results further highlight the restricted relative orientation of the POTRA domains of the Omp85-TpsB proteins as a conserved characteristic feature that might be important for the processive sliding of the unfolded substrate towards the membrane. The interactions of the *Anabaena* POTRA domains will be investigated in complexes with the potential chaperones (Tic22) and substrates and model membranes. This will help to probe the possibility of having distinct conformations of P1-P2 domains similar to the X-ray and PELDOR-refined structures.

5. Deutsche Zusammenfassung

Puls Elektron-Elektron Doppelresonanz (PELDOR)-Spektroskopie ist eine leistungsfähige Methode für die Messung Nanometer Distanzen an Spin-markierten Systemen, wie zum Beispiel Spin-markierten Membranproteinen. Jedoch weisen diese Spinsonden in Liposomaler Umgebung oft viel schnellere transversale Relaxationszeiten (T_m) auf als in Detergenz-Mizellen und begrenzt somit die Anwendung des Verfahrens in Lipiddoppelschichten. Im ersten Teil dieser Arbeit werden die wichtigsten Möglichkeiten zur Verlängerung der transversalen Relaxationszeit in Phospholipid Membranen durch die Verwendung von Spin-markierten Derivaten von Stearinsäure, Phosphatidylcholin und des kanalbildenden Peptids Gramicidin A, unter Bedingungen die typischerweise für PELDOR Abstandsmessungen eingesetzt werden, untersucht. Die Ergebnisse zeigen deutlich, dass eine Dephasierung aufgrund instantaner Diffusion, die von der dipolaren Wechselwirkung zwischen den Elektronen-Spins abhängt, ein wichtiger Faktor für den schnellen Echo Zerfall bei hohen lokalen Konzentrationen von Spinsonden in Membranen ist. Der wesentliche Unterschied zwischen Spinsonden in Detergenz-Mizellen und Membranen ist deren lokale Konzentration. Folglich ist die Vermeidung von Spin-Clustern und die Unterdrückung instantaner Diffusion der entscheidende Schritt zur Maximierung der PELDOR Empfindlichkeit in Lipidmembranen. Obwohl die Proton-Kernspin Diffusion ein wesentlicher Relaxationsmechanismus ist, verlängert sich T_m durch die Deuterierung der Akylketten und des Puffers nur in Proben mit niedriger lokaler Konzentrationen signifikant. In diesen Fällen wurden Werte von bis zu 7 μs erreicht. Außerdem ergab unsere Studie, dass sich die Zusammensetzung der Membran und Spin-Markierungs Position in der Membran sich auf T_m auswirkt, entweder durch eine stärkeren Trennung der Spin-markierten Spezies oder durch die Veränderung ihrer Exposition gegenüber Matrix Protonen. Wirkungen von anderen experimentellen Parameter wie Temperatur (<50 K), das Vorhandenseins von Sauerstoff und der Typ des Frostschutzes sind unter unseren experimentellen Bedingungen vernachlässigbar.

Im zweiten Teil der Arbeit wurden inhomogene Verteilung der Spin-Labels in Detergenz-Mizellen untersucht. Eine übliche Methode in PELDOR ist, die Nutzung von Makromolekülen mit zwei kovalent gebundenen Spin-Markern und die Messung des inter-Spin-Abstandes, oder die Verwendung von einzeln markierten Komponenten eines Systems,

79

welche Aggregate oder Oligomere ausbilden. Dies wird als Spin-Cluster bezeichnet. Das PELDOR Signal besteht nicht nur aus der gewünschten dipolaren Kopplung zwischen den Spin-Markern des Moleküls oder Clusters, sondern auch aus der dipolare Kopplung zwischen der gleichmäßig Spin-Markern über die Probe verteilten. In homogenen gefrorenen Lösungen oder Lipidvesikel Membranen ist dieser zweite Beitrag ein exponentieller oder gestreckt exponentieller Zerfall. In unserer Studie wird gezeigt, dass diese Annahme in Detergenz-Mizellen nicht gültig ist. Spin-markierte Fettsäuren, die gleichmäßig in verschiedenen Detergenz-Mizellen partitioniert sind ergeben PELDOR Zeit Spuren, die eindeutig von gestreckt exponentiellen Zerfällen abweichen. Eine wichtige Schlussfolgerung ist, ein PELDOR Signal das von einem gestreckt exponentiellen Zerfall abweicht beweist nicht notwendigerweise die Beobachtung von bestimmten Abständen an dem Molekül oder Cluster. Diese Ergebnisse sind für die Interpretation der PELDOR Experimente an Membranproteinen oder lipophiler-Peptide in Detergenz-Mizellen oder kleinen Bläschen, die oft keine ausgeprägten dipolare Periodizitäten in ihren Zeit Spuren zeigen wichtig.

In dem dritten Teil ist PELDOR verwendet worden, um die strukturelle Flexibilität des Toc34 GTPase Homodimer, ein Präprotein Rezeptor der Translocon an der äußeren Envelope-Membran der Chloroplasten (TOC) zu untersuchen. Toc34 gehört zur GAD Unterfamilie der G-Proteine, die durch Nukleotid-abhängige Dimerisierung geregelt und aktiviert wird. Jedoch ist die Funktion der Dimerisierung Toc34 noch nicht bekannt. Strukturelle Untersuchungen der Toc34 Dimere ergeben nur marginale Strukturänderungen in Reaktion auf verschiedene Nukleotid Beladung. Mit PELDOR konnte gezeigt werden eine Nukleotid-abhängige Übergang der Dimer Flexibilität aus festen GDP zu einem flexiblen GTP-beladenen Zustand. Substratbindung stabilisiert den Homodimer im durch induzierten Übergangszustand GDP-AlF$_x$, führt aber im GDP oder GTP Zustand zur Öffnung des Dimers. Somit wird die strukturelle Dynamik der gewöhnlichen GTPasen durch die substratabhängige Dimer Flexibilität, die den regulatorischen Modus zur Dimerisierung GTPasen darstellt ersetzt.

Im vierten Teil der Arbeit, wird die konformative Flexibilität und die relative Orientierung der POTRA Domänen von Cyanobakterien Omp85, ein wichtiger Bestandteil der äußeren Membran-Protein Assembly Maschinerie mit PELDOR Spektroskopie untersucht. Membranproteine der Omp85-TpsB Superfamilie bestehen aus einem C-terminalen β-barrel und einer unterschiedlichen Anzahl von N-terminalen POTRA Domänen, drei im Fall von Cyanobakterien Omp85 (P1 bis P3), zusammengesetzt. Molekulardynamik (MD)

Simulationen sagten eine feste Orientierung von P2 zu P3 und eine flexibles Scharnier zwischen P1 und P2 vorhaus. Die mit PELDOR gemessenen Abstände zwischen den POTRA Domänen P2 und P3 sind in guter Übereinstimmung mit der Röntgenstruktur sowie den MD-Simulationen, was auf eine feste Ausrichtung zwischen diesen Domänen schließen lässt. PELDOR Messungen zwischen den Domänen P1 und P2 zeigen dagegen eine eher starre Struktur mit leicht unterschiedlichen relativen Orientierung dieser Domänen verglichen mit der Röntgenstruktur. Außerdem wird die breite Orientierungsverteilung die von MD Simulationen vorhergesagten werden nicht an den Probe in gefrorener Lösung beobachtet.

Appendix

A. Sample Preparation (Membranes and Micelles)

Stock solutions of the phospholipids (25 mM), cholesterol (30 mM), and 16-SASL and SL-chol (13 mM) were prepared in chloroform, and for spin label solutions the concentrations have been calibrated against TEMPO by use of an Elexsys E500 9 GHz EPR spectrometer (Bruker). Samples with the desired spin label/phospholipid (SL/PL) molar ratio were transferred to a test tube, the solvent was evaporated with an argon gas stream, and residual traces were removed by drying under vacuum for at least 4 h before the vacuum was released by nitrogen. The dry lipids were dispersed in 10 mM phosphate-buffered saline (pH 7.4; Sigma) or in deuterium-exchanged buffer (by three times freeze-drying) at a concentration of ≤100 mg/mL, by vortex mixing at room temperature or 60 °C (for DPPC).[119,124] In these preparations, an identical total spin-label concentration of ~100 μM was prepared except for 16-SASL in POPC (1:1000) concentrated with a benchtop centrifuge to remove the excess supernatant. All the samples were deoxygenated by purging with argon (excluding the samples for the effect of oxygen that were purged with air) and were mixed in a glovebag (Aldrich AtmosBag) under nitrogen with 20% (v/v) deoxygenated ethylene glycol [except for 16-SASL in POPC (1:1000)] and transferred to standard 4 mm diameter quartz EPR tubes (Wilmod). The samples were shock-frozen in a mixture of methylcyclohexane/isopentane (1:4) that was immersed in liquid nitrogen.

In order to prepare micelle samples, 20 mM solutions of the detergents (above their critical micelle concentration (CMC) at 25 °C) were prepared in phosphate buffer, except for the SDS sample which was prepared in double-distilled water. Stock solutions of 5- and 16-SASL (2 and 27 mM, respectively) were prepared in chloroform and the concentrations have been calibrated against TEMPO as mentioned above. In order to prepare the samples of the spin-labeled stearic acids in different micelles with the desired spin-label to detergent molar ratio, the required amounts of the spin-labels in chloroform were transferred to test tubes, the solvent was evaporated with an argon gas stream, and residual traces were removed by drying under vacuum for at least 4 h before the vacuum was released by nitrogen. The prepared micelle solutions were added to the preformed films of the spin-labels. The samples were

shaken by vortex mixing at room temperature and kept overnight in a 4 °C fridge to equilibrate them.

Synthesis and reconstitution of spin-labeled gA into the vesicles and micelles has been done by Dr. Karuppiah Muruga Poopathi Raja in the group of Prof. Harald Schwalbe.

B. Pulse EPR Parameters

Pulsed EPR data were measured on an Elexsys E580 EPR spectrometer (Bruker) equipped with a Bruker PELDOR unit (E580-400U), a continuous-flow helium cryostat (CF935) and temperature control system (ITC 502), both from Oxford Instruments, at frequencies of 9.6 GHz (X-band) using a standard flex line probe head housing a dielectric ring resonator (MD5 W1, Bruker). Microwave pulses were amplified by a 1 kW TWT amplifier (ASE 117x). For Q-band PELDOR (psToc34$_{EC}$ M/C; section 3.3), the experiments were carried out at frequencies of 33.7 GHz with the Elexsys SuperQ-FT accessory unit and a Bruker AmpQ 10 W amplifier. The cavity is a Bruker EN5107D2. A custom made pulse shaping unit was implemented which is described elsewhere.[162] Temperature was kept at 50 K, if not mentioned otherwise. The shot repetition time was 1.5−3 ms (section 3.1), 2−3 ms (section 3.2), 4−4.5 ms (section 3.3), and 4−5 ms (section 3.3). EPR spectra were measured with field-swept, echo-detected EPR by use of a Hahn echo sequence, $^{2\pi}/_3$-τ-$^{2\pi}/_3$-τ-echo, and a 15 mT field sweep. The pulse separation time τ was set to 200 ns for protonated samples and 380 ns for deuterated samples with a length of the $^{2\pi}/_3$ pulses of 32 ns. Transversal relaxation data were acquired with a Hahn echo sequence $^{\pi}/_2$-τ-π-τ-echo. An initial τ of 120 ns and an increment of 4 ns were used. The integrated echo intensity was measured as a function of this increment, with an integration gate of 20−32 ns length centered at the echo maximum. The pulse lengths were 16 ns for the $^{\pi}/_2$ pulse and 32 ns for the π pulse. Instantaneous diffusion was probed by gradually changing the flip angle of the 32 ns pulse from π to $^{\pi}/_8$.

For PELDOR experiments the dead-time free four-pulse sequence was used.[4] Typical pulse lengths were 32 ns (π/2 and π) for the probe pulses and 12 ns (π) for the pump pulse (14 ns in sections 3.1 and 3.2). For the psToc34$_{EC}$ M/C mutant, a 80 MHz sech/tanh adiabatic pump pulse with a length of 360 ns was utilized.[153] The delay between the first and second probe pulses was varied between 136(200) and 192(256) ns in 8 ns steps (protonated samples; between 132 and 188 ns in section 3.1), between 456 and 848 ns in 56 ns steps for buffer deuterated sample in section 3.4 (I292R1A/V460R1A), and between 400 and 792 ns in 56 ns

steps for deuterated samples in section 3.1. This averaging reduces the contributions from nuclear modulations.[163] For the buffer-deuterated sample in section 3.3 (psToc34$_{EC}$ M/C) a constant delay of 356 ns was used. The pulse separation between the second and third probe pulses was between 1.2 and 8.5 µs, depending on the probed distances and transversal relaxation time (T_m) of the samples. For X-band PELDOR, the frequency of the pump pulse was set to center of the over-coupled resonator (Q ~50) and the magnetic field was adjusted, such that the excitation coincides with the central peak of the nitroxide powder spectrum to obtain maximum pumping efficiency. The probe frequency was chosen 70 MHz higher (80 MHz for the A319R1A/E344R1A sample in section 3.4). For the Q-band PELDOR, the pump pulse was placed on the maximum of the nitroxide absorption spectrum and the the probe frequency was chosen 70 MHz lower. In case of samples in section 3.4 the orientation selection of nitroxide labels with respect to each other was probed by 40 MHz frequency offset and no changes in average distances were observed compared with the former offset (not shown).[105]

C. Modeling of PELDOR time traces (section 3.2)

Modeling of PELDOR time traces in section 3.2 has been done by Dr. Bela Bode, a former postdoc in our group.

Owing to their amphipathic nature, spin-labeled fatty acids are expected to be confined inside the micelles. To model the observed PELDOR decays we used two limiting models for the description of the distribution of spin-labels inside the micelles. In both models the micelles are assumed to be spherical. In the first model the nitroxyl groups of the spin-labels are assumed to be close to the surface of the micelle (*surface* model). This might be induced by either steric repulsion inside the micelle or by strong attraction between the polar nitroxide moiety and the polar detergent head-groups.[164] The other limiting model assumes a homogeneous distribution of the nitroxides inside the micelle (*bulk* model). These simplified models are chosen because analytical expressions for the statistical distance distribution functions are easily available for both models. The probability density distribution for the distance between two points on the surface of a sphere is:[165]

$$P_{surf}(r) = \frac{2r}{D^2} \qquad \text{(eq. 37)}$$

where r is the distance between the points and D the diameter of the sphere.

The probability density distribution for the distance between two points inside a sphere is:[166]

$$P_{bulk}(r) = \frac{3r^2}{(D/2)^3} - \frac{9r^3}{4(D/2)^4} + \frac{3r^5}{16(D/2)^6}$$

(eq. 38)

The real situation is most probably best reflected by the spin-labeled fatty acids occupying a sphere shell with a certain width. In this case, the two models represent two limiting approximations of the actual distribution which will depend on the specific spin-label.[151] Both limiting models allow simulating the experimentally observed non-exponential PELDOR decay curves; therefore the actual distribution function is dispensable for our analysis.

The probability of finding a micelle with k spin-labeled fatty acid molecules is estimated by the binomial distribution:

$$P_{label}(k) = \binom{n}{k} p^k (1-p)^{n-k}$$

(eq. 39)

with n being the number of detergent molecules per micelle (aggregation number) and p the probability of a detergent being spin-labeled (labeling degree). The binomial coefficients for the case $n = 100$ and $p = 0.01$ are depicted as a histogram in Figure 39.
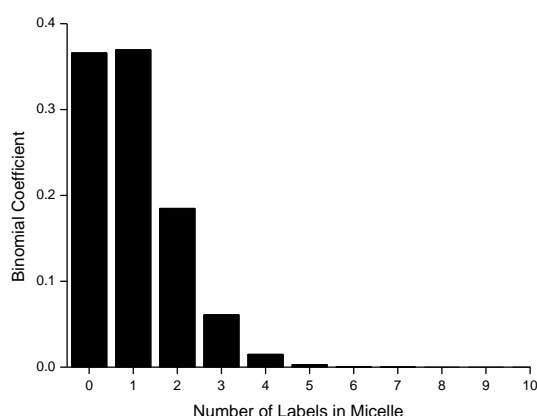
Figure 39. Binomial coefficients for statistic labeling. The data displayed corresponds to the case of $n = 100$ and $p = 0.01$.

The distance dependent dipolar coupling between the spin-labels is calculated according to eq. 15:

$$v(r,x) = dip(r)(1-3x^2)$$
$$dip(r) = \frac{g_A g_B \mu_0 \beta_e^2}{4\pi\hbar}\frac{1}{r^3}$$

(eq. 40)

where ($x = \cos\theta$).

In both models short spin-spin distances are present. This will give rise to large dipolar couplings, which exceed the excitation bandwidths of the microwave pulses. A correction for the suppression of these large spin-spin interactions can be estimated according to:

$$\lambda(r) = \lambda_0 \int_0^1 \exp\left(-\left(\frac{v(r,x)t_{p1}}{\pi}\right)^2\right)\exp\left(-\left(\frac{v(r,x)t_{p2}}{\pi}\right)^2\right)dx$$

(eq. 41)

where the integral describes the dipolar frequency (v)-dependent suppression of intensities as a function of the lengths of the pumping and detection pulses, t_{p1} and t_{p2} respectively.[90,167] λ_0 is the modulation depth parameter. Eq. 41 is a good approximation to rescale the modulation depth for strong dipolar couplings, which effectively diminishes contributions to the PELDOR signal arising from spin-pairs with very short distances.

Assuming the orientations of the two spin-labels to be uncorrelated, the PELDOR time trace for a doubly-labeled micelle can be calculated similar to eq. 28:

$$V_{surf}^{pair}(t,D,\lambda_0) = \int_0^r P_{surf}(r)(1-\lambda(r))\int_0^1 (1-\cos(2\pi v(r,x)t))dxdr$$
$$V_{bulk}^{pair}(t,D,\lambda_0) = \int_0^r P_{bulk}(r)(1-\lambda(r))\int_0^1 (1-\cos(2\pi v(r,x)t))dxdr$$

(eq. 42)

It is obvious from eq. 42 that both the distance distribution function $P(r)$ and micelle radius r directly influence the PELDOR signal. The overall signal of the statistically labeled micelle is the weighted sum of the 1-fold to n-fold labeled micelle:[87,89,147]

$$V_{surf}(t, D, \lambda_0, p, n) = \frac{\sum_{k=1}^{n} P_{label}(k)\left(V_{surf}^{pair}(t)\right)^{k-1}}{\sum_{k=1}^{n} P_{label}(k)}$$

$$V_{bulk}(t, D, \lambda_0, p, n) = \frac{\sum_{k=1}^{n} P_{label}(k)\left(V_{bulk}^{pair}(t)\right)^{k-1}}{\sum_{k=1}^{n} P_{label}(k)}$$

(eq. 43)

The normalization is necessary since there is a possibility of zero labels in a micelle ($k = 0$), which does not contribute to the PELDOR signal.

Until here, we have considered only the dipolar interactions between spin labels in one micelle, however; also interactions between spin labels in different micelles might contribute to the PELDOR signal. This background contribution is assumed to be caused by a homogeneous distribution of micelles in three dimensions. For dilute two- to fourfold labeled model compounds an exponential background function (eq. 23) has shown excellent agreement with the experimental data:[89]

$$V_{total}(t, D, \lambda_0, p, n, c) = V(t, D, \lambda_0, p, n)\exp(-bc\lambda_0 t)$$

$$b = \frac{2\pi\mu_0 g_A g_B \beta_e^2}{9\sqrt{3}\hbar}$$

(eq. 44)

where c is the spin-label concentration in m^{-3}.

The PELDOR time traces in micelles can be simulated according to eq. 44. *Vice versa* the micelle parameters can be verified by a fit of D, p, n, and c to the experimental time traces. To obtain the micelle parameters the root mean square deviation between experimental data and calculated V_{total} (eq. 44) has been minimized for both models individually using the Matlab® function fminsearch. D, p, n and c have been optimized simultaneously. The integrations in eq. 42 have been performed numerically in steps of 0.01 nm and 10^{-3} respectively. Distributions of micelle sizes and aggregation numbers have not been considered. Multiple labeled micelles (k) with a statistical weight smaller than 10^{-4} have been neglected. To explore the effects of the strong interdependence of p and n, which both mainly scale the modulation depth, a second optimization has been performed. Here, p has been set to the nominal labeling degree while D, n and c being simultaneously optimized.

D. cw EPR Parameters and Measurements

Room and low temperature X-band (9.54 GHz) cw EPR spectra were recorded on a Bruker E500 spectrometer equipped with a TE102 cavity. Experimental parameters which were used for concentration determination include 100 kHz modulation frequency, 1.5 G modulation amplitude, 2 mW microwave power, 40.96 ms time constant, 40.96 ms conversion time, 512 points, 120 G sweep width, 75 dB receiver gain, typically 40-50 scans.

The low temperature X-band cw EPR spectra were recorded under the following experimental conditions: 100 kHz modulation frequency, 2 G modulation amplitude, 0.01 mW microwave power, 40.96 ms time constant, 40.96 ms conversion time, 1024 points, 120 G sweep width, at $T = 70$ K.
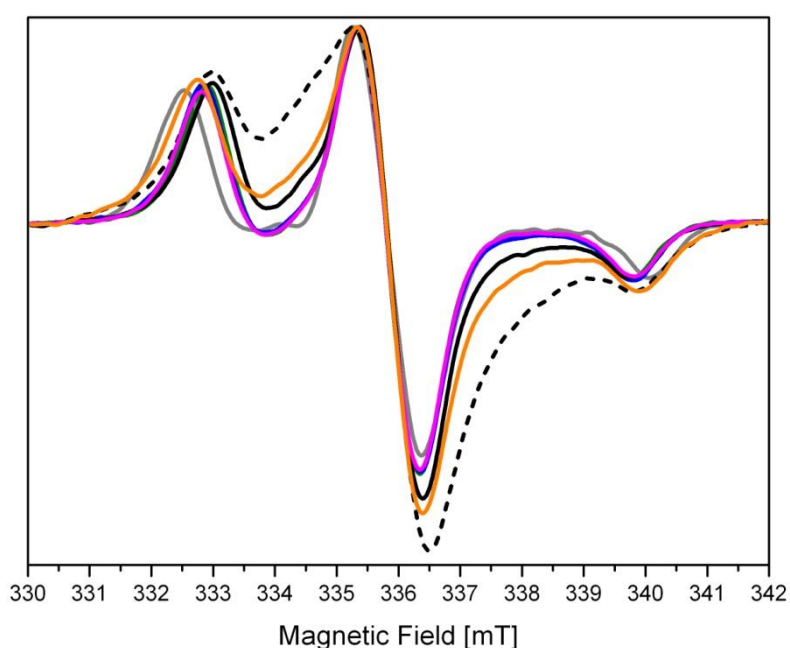
Figure 40. X-band cw EPR spectra of the spin-labeled fatty acids incorporated into micelles at $T = 70$ K (related to Table 3). TEMPOL in water (gray), 1% 16-SASL/DDM (solid black), 3% 16-SASL/DDM (dashed black), 1% 5-SASL/DDM (magenta), 1% 16-SASL/Triton (green), 1% 16-SASL/$C_{12}E_8$ (blue), 1% 16-SASL/SDS (orange).
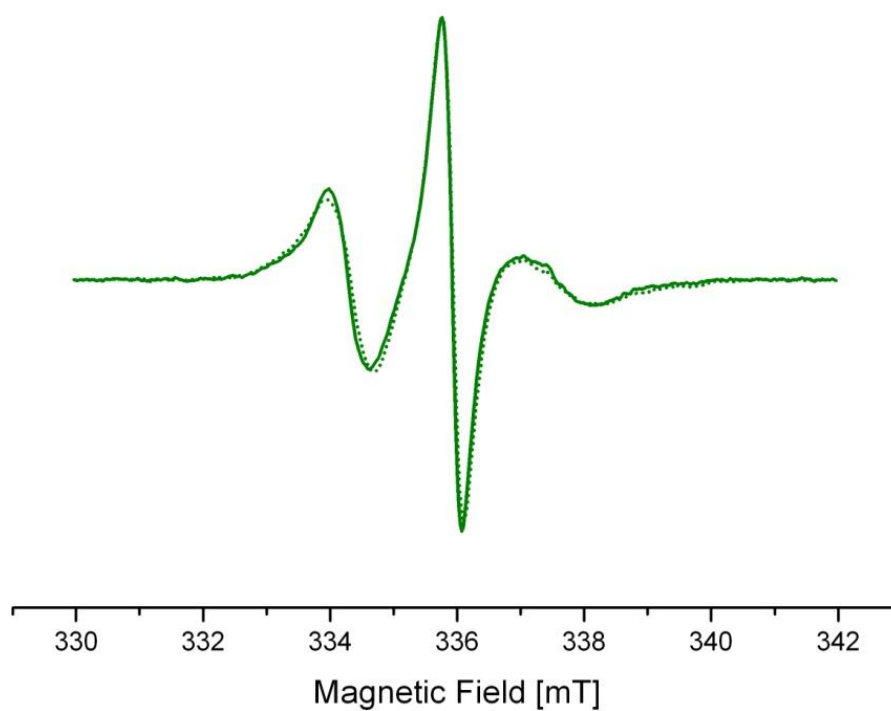
Figure 41. X-band cw EPR spectra of the *ps*Toc34 K143C loaded with GDP at room temperature. Without (dotted line) or with (solid line) of 1 mM transit peptide.
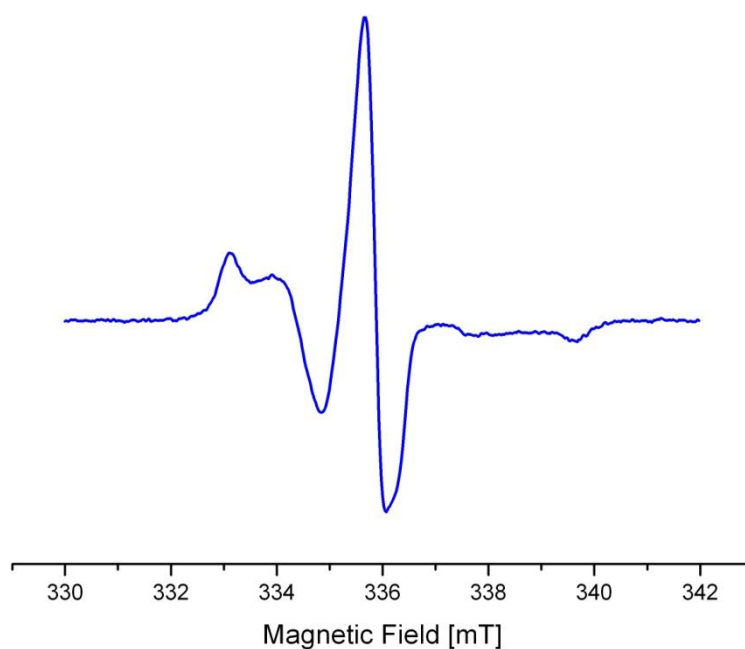
Figure 42. X-band spectrum of the *ps*Toc34 M79C loaded with GDP at room temperature. Spin labeling efficiency ~ 68%.

89
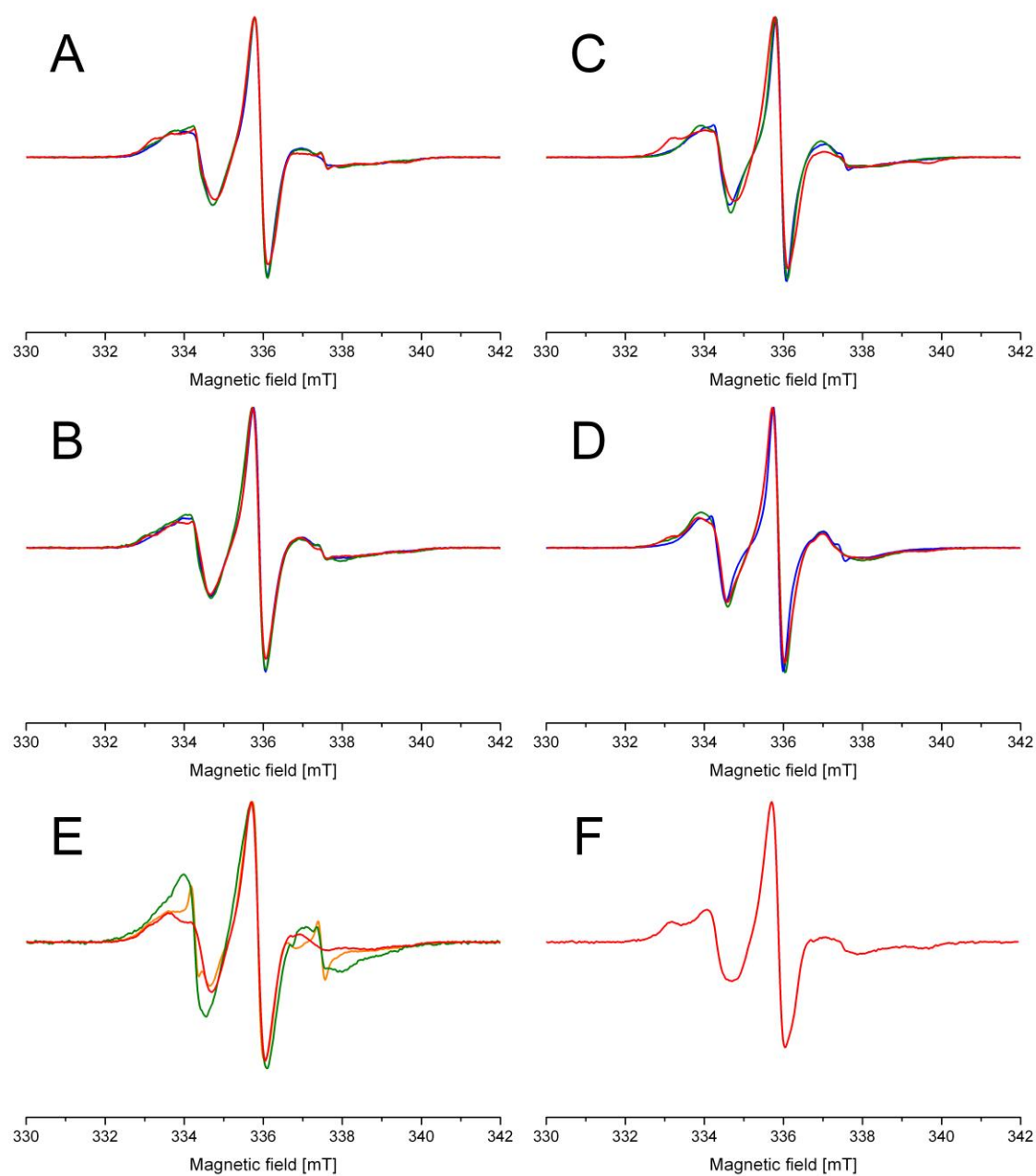
Figure 43. X-band cw EPR spectra of the POTRA double- (A-E) and single-Cys (F) mutants at room temperature. (A) V460-V370 (red), V460-E344 (green), V460-A319 (blue); (B) Q429-V370 (red), Q429-E344 (green), Q429-A319 (blue); (C) I292-V370 (red), Q429-E344 (green), Q429-A319 (blue); (D) N265-V370 (red), N265-E344 (green), N265-A319 (blue); (E) I292-V460 (red), A319-E344 (green), Q429-V460 (orange); (F) V370.

E. GTPase Activity Measurement on Toc34 Cysteine Mutants

These measurements are done by the group of Prof. Enrico Schleiff.
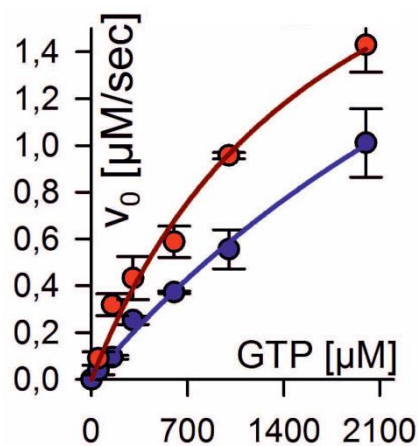
Figure 44. The Michaelis-Menten kinetics for GTP hydrolysis of the mutants: (red) *ps*Toc34 K143C, (blue) *ps*Toc34 M79C; values are listed in table 10.

Table 10. Multiple turnover GTP hydrolysis.

Protein[a]	V_{max} $[\mu M\ s^{-1}]$	K_M [mM]	k_{cat} $[s^{-1}]$
*ps*Toc34ΔTM	0.6±0.1	0.7±0.1	0.2
*ps*Toc34$_{zipper}$	1.2±0.2	0.7±0.1	0.4
*ps*Toc34$_{zipper}$ M79C	3.1±0.4	4.2±0.7	1.0
*ps*Toc34$_{zipper}$ K143C	2.5±0.2	1.5±0.3	0.8

[a] 3 μM receptor concentration.

List of Figures

List of Tables

Bibliography

[1]   Jeschke, G. *Annu Rev Phys Chem*, **2012**, *63*, 419.

[2]   Schiemann, O.; Prisner, T. F. *Q Rev Biophys*, **2007**, *40*, 1.

[3]   Milov, A. D.; Salikhov, K. M.; Shirov, M. D. *Fiz Tverd Tela*, **1981**, *23*, 975.

[4]   Pannier, M.; et al. *J Magn Reson*, **2000**, *142*, 331.

[5]   Altenbach, C.; et al. *Proc Natl Acad Sci U S A*, **2008**, *105*, 7439.

[6]   Grote, M.; et al. *J Biol Chem*, **2009**, *284*, 17521.

[7]   Bhatnagar, J.; Freed, J. H.; Crane, B. R. *Method Enzymol*, **2007**, *423*, 117.

[8]   Hilger, D.; et al. *Biophys J*, **2007**, *93*, 3675.

[9]   Jao, C. C.; et al. *Proc Natl Acad Sci U S A*, **2008**, *105*, 19666.

[10]   Ward, R.; et al. *Structure*, **2009**, *17*, 1187.

[11]   Hilger, D.; et al. *Biophys J*, **2009**, *96*, 217.

[12]   Yang, Y.; et al. *J Am Chem Soc*, **2010**, *132*, 11910.

[13]   Lillington, J. E.; et al. *J Mol Biol*, **2011**, *405*, 427.

[14]   Hirst, S. J.; et al. *J Struct Biol*, **2011**, *173*, 506.

[15]   Sun, Y. J.; et al. *Nat Struct Biol*, **2002**, *9*, 95.

[16]   Koenig, P.; et al. *Structure*, **2008**, *16*, 585.

[17]   Koenig, P.; et al. *J Biol Chem*, **2010**, *285*, 18016.

[18]   Sandelius, A. S.; Aronsson, H. *The chloroplast: interactions with the environment.* Vol. 13., Springer-Verlag, Heidelberg, Germany, **2009**.

[19]   Kessler, F.; Schnell, D. J. *Traffic*, **2006**, *7*, 248.

[20]   Oreb, M.; Tews, I.; Schleiff, E. *Trends Cell Biol*, **2008**, *18*, 19.

[21]   Andres, C.; Agne, B.; Kessler, F. *Biochim Biophys Acta*, **2010**, *1803*, 715.

[22]   Schleiff, E.; Becker, T. *Nat Rev Mol Cell Biol*, **2011**, *12*, 48.

[23]   Reumann, S.; Inoue, K.; Keegstra, K. *Mol Membr Biol*, **2005**, *22*, 73.

[24]   Reumann, S.; Davila-Aponte, J.; Keegstra, K. *Proc Natl Acad Sci U S A*, **1999**, *96*, 784.

[25]   Bruce, B. D. *Trends Cell Biol*, **2000**, *10*, 440.

[26]   Hiltbrunner, A.; et al. *J Cell Biol*, **2001**, *154*, 309.

[27]   Wittinghofer, A.; Vetter, I. R. *Annu Rev Biochem*, **2011**, *80*, 943.

[28]   Gasper, R.; et al. *Nat Rev Mol Cell Biol*, **2009**, *10*, 423.

[29]   Scheffzek, K.; Ahmadian, M. R. *Cell Mol Life Sci*, **2005**, *62*, 3014.

[30]   Vetter, I. R.; Wittinghofer, A. *Science*, **2001**, *294*, 1299.

[31]   DerMardirossian, C.; Bokoch, G. M. *Trends Cell Biol*, **2005**, *15*, 356.

[32]   Bos, J. L.; Rehmann, H.; Wittinghofer, A. *Cell*, **2007**, *129*, 865.

[33]   Focia, P. J.; et al. *Science*, **2004**, *303*, 373.

[34]   Leipe, D. D.; et al. *J Mol Biol*, **2002**, *317*, 41.

[35]   Weirich, C. S.; Erzberger, J. P.; Barral, Y. *Nat Rev Mol Cell Biol*, **2008**, *9*, 478.

[36]   Kouranov, A.; Schnell, D. J. *J Cell Biol*, **1997**, *139*, 1677.

[37]   Sveshnikova, N.; Soll, J.; Schleiff, E. *Proc Natl Acad Sci U S A*, **2000**, *97*, 4973.

[38]   Aronsson, H.; et al. *Plant J*, **2010**, *63*, 297.

[39]   Koenig, P.; et al. *J Biol Chem*, **2008**, *283*, 23104.

[40]   Lee, J. H.; Wang, F.; Schnell, D. J. *J Biol Chem*, **2009**, *284*, 31130.

[41]   Yeh, Y. H.; et al. *J Biol Chem*, **2007**, *282*, 13845.

[42]   Scheffzek, K.; Ahmadian; M. R.; Wittinghofer, A. *Trends Biochem Sci*, **1998**, *23*, 257.

[43]   Bauer, J.; et al. *J Cell Biol*, **2002**, *159*, 845.

[44]   Becker, T.; et al. *Embo J*, **2004**, *23*, 520.

[45]   Weibel, P.; et al. *J Biol Chem*, **2003**, *278*, 37321.
[46]   Kessler, F.; Schnell, D. J. *Nat Struct Biol*, **2002**, *9*, 81.
[47]   Wallas, T. R.; et al. *J Biol Chem*, **2003**, *278*, 44289.
[48]   Sommer, M. S.; Schleiff, E. *Biol Chem*, **2009**, *390*, 739.
[49]   Aronsson, H.; Combe, J.; Jarvis, P. *Febs Lett*, **2003**, *544*, 79.
[50]   Oreb, M.; et al. *J Exp Bot*, **2008**, *59*, 2309.
[51]   Jelic, M.; et al. *Biol Chem*, **2002**, *383*, 1875.
[52]   Becker, T.; et al. *Mol Biol Cell*, **2004**, *15*, 5130.
[53]   Reddick, L. E.; et al. *J Biol Chem*, **2007**, *282*, 11410.
[54]   Schleiff, E.; et al. *J Cell Biol*, **2003**, *160*, 541.
[55]   Schleiff, E.; Jelic, M.; Soll, J. *Proc Natl Acad Sci U S A*, **2003**, *100*, 4604.
[56]   Bauer, J.; et al. *Nature*, **2000**, *403*, 203.
[57]   Voigt, A.; et al. *Febs Lett*, **2005**, *579*, 1343.
[58]   Hirsch, S.; et al. *Science*, **1994**, *266*, 1989.
[59]   Schnell, D. J.; Kessler, F.; Blobel, G. *Science*, **1994**, *266*, 1007.
[60]   Kessler, F.; et al. *Science*, **1994**, *266*, 1035.
[61]   Hiltbrunner, A.; et al. *Biochem Cell Biol*, **2001**, *79*, 629.
[62]   Torres, J. H.; Maldonado, M. A. A.; Chomilier, J. *Biochem Biophys Res Commun*, **2007**, *364*, 325.
[63]   Oreb, M.; et al. *Biochem J*, **2011**, *436*, 313.
[64]   Ruprecht, M.; et al. *Mol Plant*, **2010**, *3*, 499.
[65]   Eckart, K.; et al. *Embo Rep*, **2002**, *3*, 557.
[66]   Inoue, K.; Potter, D. *Plant J*, **2004**, *39*, 354.
[67]   Sommer, M. S.; et al. *Proc Natl Acad Sci U S A*, **2011**, *108***, 13841.
[68]   Ertel, F.; et al. *J Biol Chem*, **2005**, *280*, 28281.
[69]   Lee, K. H.; et al. *J Biol Chem*, **2003**, *278*, 36794.
[70]   Clantin, B.; et al. *Science*, **2007**, *317*, 957.
[71]   Arnold, T.; Zeth, K.; Linke, D. *J Biol Chem*, **2010**, *285*, 18003.
[72]   Schleiff, E.; Maier, U. G.; Becker, T. *Biol Chem*, **2011**, *392*, 21.
[73]   Kim, S.; et al. *Science*, **2007**, *317*, 961.
[74]   Gatzeva-Topalova, P. Z.; Walton, T. A.; Sousa, M. C. *Structure*, **2008**, *16*, 1873.
[75]   Knowles, T. J.; et al. *Mol Microbiol*, **2008**, *68*, 1216.
[76]   Gatzeva-Topalova, P. Z.; et al. *Structure*, **2010**, *18***, 1492.
[77]   Ricci, D. P.; Silhavy, T. J. *BBA-Biomembranes*, **2012**, *1818*, 1067.
[78]   Hodak, H.; et al. *Mol Microbiol*, **2006**, *61*, 368.
[79]   Delattre, A. S.; et al. *Mol Microbiol*, **2011**, *81*, 99.
[80]   Bredemeier, R.; et al. *J Biol Chem*, **2007**, *282*, 1882.
[81]   Schweiger, A.; Jeschke, G. *Principles of Pulse Electron Paramagnetic Resonance*. Oxford University Press, USA, **2001**.
[82]   Weil, J. A.; Bolton, J. R. *Electron paramagnetic resonance: elementary theory and practical applications*. 2nd ed., Wiley-Interscience: Hoboken, N. J., **2007**.
[83]   Jeschke, G.; Polyhach, Y. *Phys Chem Chem Phys*, **2007**, *9*, 1895.
[84]   Stoll, S.; Schweiger, A. *J Magn Reson*, **2006**, *178*, 42.
[85]   Eaton, S. S.; Eaton, G. R. In *Biological Magnetic Resonance, Vol. 19, Distance Measurements in Biological Systems by EPR*; Berliner, L. J.; Eaton, S. S.; Eaton, G. R. Eds., Kluwer Academics/Plenum Publishers: New York, **2000**, pp 29-71.
[86]   Zecevic, A.; et al. *Mol Phys*, **1998**, *95*, 1255.
[87]   Milov, A. D.; Ponomarev, A. B.; Tsvetkov, Y. D. *Chem Phys Lett*, **1984**, *110*, 67.
[88]   Milov, A. D.; Maryasov, A. G.; Tsvetkov, Y. D. *Appl Magn Reson*, **1998**, *15*, 107.

[89]   Bode, B. E.; et al. *J Am Chem Soc*, **2007**, *129*, 6736.

[90]   Jeschke, G.; et al. *Appl Magn Reson*, **2006**, *30*, 473.

[91]   Borbat, P. P.; Mchaourab, H. S.; Freed, J. H. *J Am Chem Soc*, **2002**, *124*, 5304.

[92]   Polyhach, Y.; Bordignon, E.; Jeschke, G. *Phys Chem Chem Phys*, **2011**, *13*, 2356.

[93]   Sali, A.; Blundell, T. L. *J Mol Biol*, **1993**, *234*, 779.

[94]   Zheng, W.; Brooks, B. R. *Biophys J*, **2006**, *90*, 4327.

[95]   Jeschke, G. *J Chem Theory Comput*, **2012**, 10.1021/ct300113z.

[96]   Krogh, A.; et al. *J Mol Biol*, **2001**, *305*, 567.

[97]   Seddon, A. M.; Curnow, P.; Booth, P. J. *Biochim Biophys Acta*, **2004**, *1666*, 105.

[98]   Overington, J. P.; Al-Lazikani, B.; Hopkins, A. L. *Nat Rev Drug Discovery*, **2006**, *5*, 993.

[99]   Gustot, A.; et al. *J Biol Chem*, **2010**, *285*, 14144.

[100] Äänismaa, P.; Gatlik-Landwojtowicz, E.; Seelig, A. *Biochemistry*, **2008**, *47*, 10197.

[101] Rigaud, J. L. *Braz J Med Biol Res*, **2002**, *35*, 753.

[102] Perozo, E.; Cortes, D. M.; Cuello, L. G. *Nat Struct Biol*, **1998**, *5*, 459.

[103] Hubbell, W. L.; Cafiso, D. S.; Altenbach, C. *Nat Struct Biol*, **2000**, *7*, 735.

[104] Schiemann, O.; et al. *Angew Chem Int Edit*, **2009**, *48*, 2392.

[105] Endeward, B.; et al. *J Am Chem Soc*, **2009**, *131*, 15246.

[106] Marko, A.; et al. *Phys Rev E*, **2010**, *81*, 021911.

[107] Jeschke, G.; et al. *Biophys J*, **2004**, *86*, 2551.

[108] Hilger, D.; et al. *Biophys J*, **2005**, *89*, 1328.

[109] Xu, Q.; et al. *Biochemistry*, **2006**, *45*, 10847.

[110] Milov, A. D.; et al. *J Am Chem Soc*, **2007**, *129*, 9260.

[111] Zou, P.; Bortolus, M.; Mchaourab, H. S. *J Mol Biol*, **2009**, *393*, 586.

[112] Borbat, P. P.; et al. *PLoS Biol*, **2007**, *5*, e271.

[113] Upadhyay, A. K.; et al. *Biochemistry*, **2008**, *47*, 1554.

[114] Zou, P.; Mchaourab, H. S. *Biophys J*, **2010**, *98*, L18.

[115] Georgieva, E. R.; et al. *J Am Chem Soc*, **2008**, *130*, 12856.

[116] Meirovitch, E.; Nayeem, A.; Freed, J. H. *J Phys Chem*, **1984**, *88*, 3454.

[117] Bonosi, F.; et al. *Langmuir*, **1990**, *6*, 1769.

[118] Bratt, J. P.; Kevan, L. *J Phys Chem*, **1993**, *97*, 7371.

[119] Lee, D. K.; et al. *Langmuir*, **1998**, *14*, 5184.

[120] Isaev, N. P.; Dzuba, S. A. *J Phys Chem B*, **2008**, *112*, 13285.

[121] Fajer, P.; Watts, A.; Marsh, D. *Biophys J*, **1992**, *61*, 879.

[122] Earle, K. A.; et al. *Biophys J*, **1994**, *66*, 1213.

[123] Dzikovski, B. G.; Livshits, V. A.; Marsh, D. *Biophys J*, **2003**, *85*, 1005.

[124] Bartucci, R.; et al. *Biophys J*, **2003**, *84*, 1025.

[125] Bartucci, R.; et al. *J Magn Reson*, **2003**, *162*, 371.

[126] Ge, M.; Freed, J. H. *Biophys J*, **1999**, *76*, 264.

[127] Dzikovski, B. G.; Borbat, P. P.; Freed, J. H. *Biophys J*, **2004**, *87*, 3504.

[128] Sato, H.; et al. *J Phys Chem B*, **2008**, *112*, 2818.

[129] Volkov, A.; et al. *Biophys J*, **2009**, *96*, 1124.

[130] Milov, A. D.; et al. *Appl Magn Reson*, **2005**, *29*, 703.

[131] Milov, A. D.; et al. *Phys Chem Chem Phys*, **2005**, *7*, 1794.

[132] Ollila, S.; Hyvönen, M. T.; Vattulainen, I. *J Phys Chem B*, **2007**, *111*, 3139.

[133] Vogel, A.; Scheidt, H. A.; Huster, D. *Biophys J*, **2003**, *85*, 1691.

[134] Dastvan, R.; et al. *J Phys Chem B*, **2010**, *114*, 13507.

[135] Garay, A. S.; Rodrigues, D. E. *J Phys Chem B*, **2008**, *112*, 1657.

[136] van den Brink-van der Laan, E.; Killian, J. A.; de Kruijff, B. Biochim Biophys Acta, **2004**, *1666*, 275.

[137] Pfannebecker, V.; et al. *J Phys Chem*, **1996**, *100*, 13428.
[138] Weber, A.; et al. *J Magn Reson*, **2002**, *157*, 277.
[139] Zhou, Z.; et al. *Biochemistry*, **2005**, *44*, 15115.
[140] Banham, J. E.; et al. *Angew Chem Int Ed Engl*, **2006**, *45*, 1058.
[141] Ruthstein, S.; et al. *J Phys Chem B*, **2005**, *109*, 22843.
[142] Ruthstein, S.; Goldfarb, D. *J Phys Chem C*, **2008**, *112*, 7102.
[143] Mao, Q.; et al. *Phys Chem Chem Phys*, **2008**, *10*, 1156.
[144] Ionita, P.; et al. *Anal Chem*, **2008**, *80*, 95.
[145] Moller, J. V.; Lemaire, M. *J Biol Chem*, **1993**, *268*, 18659.
[146] Steinhoff, H.; et al. *Biochim Biophys Acta*, **2000**, *1457*, 253.
[147] Jeschke, G.; et al. *Phys Chem Chem Phys*, **2009**, *11*, 6580.
[148] Lipfert, J.; et al. *J Phys Chem B*, **2007**, *111*, 12427.
[149] Turro, N. J.; Yekta, A. *J Am Chem Soc*, **1978**, *100*, 5951.
[150] Duplatre, G.; Ferreira Marques, M. F.; daGracaMiguel, M. *J Phys Chem*, **1996**, *100*, 16608.
[151] Brown, L. R.; Bosch, C.; Wuthrich, K. *Biochim Biophys Acta*, **1981**, *642*, 296.
[152] Schiemann, O. *Method Enzymol*, **2009**, *469*, 329.
[153] Spindler, P. E.; et al. *Angew Chem Int Ed Engl*, under revision.
[154] Schleiff, E.; et al. *Biochemistry*, **2002**, *41*, 1934.
[155] Eswar, N.; et al. *Curr Protoc Bioinformatics*, **2006**. *Chapter 5*, Unit 5 6.
[156] Hagelueken, G.; et al. *Appl Magn Reson*, **2012**, *42*, 377.
[157] Halkides, C. J.; et al. *Biochemistry*, **1994**, *33*, 4019.
[158] Hansson, S.; et al. *Febs Lett*, **2005**, *579*, 4492.
[159] Gao, Y. G.; et al. *Science*, **2009**, *326*, 694.
[160] Stark, H.; et al. *Cell*, **2000**, *100*, 301.
[161] Gras, S.; et al. *EMBO Rep*, **2007**, *8*, 569.
[162] Spindler, P. E.; et al. *J Magn Reson*, **2012**, *218*, 49.
[163] Jeschke, G.; et al. *Appl Magn Reson*, **2004**, *26*, 223.
[164] Baglioni, P.; et al. *J Am Chem Soc*, **1993**, *115*, 4286.
[165] Lord, R. D. *Ann Math Stat*, **1954**, *25*, 794.
[166] Parry, M.; Fischbach, E. *J Math Phys*, **2000**, *41*, 2417.
[167] Bode, B. E.; et al. *J Phys Chem A*, **2008**, *112*, 5064.

Acknowledgements

Firstly, I wish to express my gratitude to Prof. Dr. Thomas F. Prisner for inviting me to Frankfurt and for the privilege to work in his group and under his supervision. He provided excellent working conditions, constant support and interest, suggestions and guidance. He always encouraged me to work independently. His engaging arguments and strong feedback contributed greatly to this dissertation and his in depth knowledge of EPR was always inspiring.

I am indebted to Dr. Bela E. Bode for introducing me into the experimental details of EPR spectroscopy specially the PELDOR method, and for the nice collaboration on the projects on transversal relaxation in membranes and PELDOR distance measurements in micelles that resulted in two publications. I admire his in-depth experience in the field, from which I was benefited during my PhD studies.

I am thankful to Dr. Sevdalina Lyubenova for providing me with her expertise on the application of EPR spectroscopy on biological macromolecules as well as starting the projects on Toc-core complex and cyanobacterial POTRA domains.

I thank Dr. Andriy Marko for the quantitative analysis of the experimental data on transversal relaxation in membranes that significantly improved the value of that study.

I am thankful to Dr. Burkhard Endeward for his commitment to work, to maintain the computer network and the pulsed EPR spectrometer. He translated the German summary in this thesis.

Prof. Dr. Enrico Schleiff is acknowledged for the supportive collaboration and scientific discussions concerning the projects on TOC complex and cyanobacterial POTRA domains.

Prof. Dr. Harald Schwalbe and Dr. Karuppiah Muruga Poopathi Raja are acknowledged for providing me with samples of gramicidin A.

Eva-Maria Brouwer is thanked for providing samples of POTRA domains. I always admire her dedication, cooperation, and motivation. I am thankful to Dr. Maik S. Sommer for coordinating our collaborations on Toc-core complex and cyanobacterial POTRA domains. Dr. Oliver Mirus is thanked for providing me with MD simulations data on *Anabaena*

POTRA domains. I am thankful to Hasret Altan, Jens Kretschmer, and Manuela Dehmer for the preparation of Toc34 homodimer samples.

I am thankful to Dr. Deniz Sezer for his constructive suggestions. I enjoyed his challenging style of questioning ideas and results, which led to a more progressive environment, beneficial for the whole group.

I thank Denise Schütz for measuring some of the POTRA control samples and Dr. Alexey Cherepanov for the help in freezing of a control sample by freeze-quench technique. Ahmadreza Mehdipour is thanked for introducing me to structural refinement using Modeller.

My officemate Dr. Ivan Krstić is thanked for lots of small talks and scientific discussions. We shared a lot of great moments together during our studies and I really appreciate his thoughtful attitude towards me.

In addition to the group members mentioned before, I would like to thank Philipp Spindler, Dr. Adrian Cernescu, Dr. Dominik Margraf, Dr. Jörn Plackmeyer, Dr. Jan Krummenacker, Dr. Petr Neugebauer, Dr. Vasyl Denysenkov, Dr. Mark Prandolini, Dr. Marat Gafurov, Dr. Haleh Hashemi Haeri, Claudia Grytz, Bisera Krstić, Sigrid Kämmerer, Charlotte Börner and Bernhard Thiem for the pleasant working environment.

I thank my parents for their love, endless support and encouragement.

I am deeply indebted to my wife Khadijeh; without her love, sacrifices, and devotion neither life nor work would be fulfilling.

Last, but not least I am indebted to Mr. Koorosh Bizhani, Mr. Behnam Daghoghi, Dr. Saeid Kazemi Ashtiani (1961-2006), Dr. Hossein Baharvand, Prof. Hamid Mobasheri, Prof. Mohammad N. Sarbolouki (1944-2009), and Prof. Mehriar Amininasab who significantly helped me in my scientific career and achievements.

Curriculum Vitae

Reza Dastvan

PERSONAL DATA

Date of Birth: January 5th 1982
Place of Birth: Bandar-Abbas, IRAN
Citizenship: Iranian
Current Address: Am Dorfgarten 1
                      60435 Frankfurt am Main
                      Germany
Tel.:   +49 (0) 69 57809408
E-Mail: dastvan@epr.uni-frankfurt.de

EDUCATION

07/2008 – 10/2012	PhD Student in the research group of Prof. Dr. Thomas F. Prisner, Institute of Physical and Theoretical Chemistry, Johann Wolfgang Goethe University, Frankfurt am Main, Germany • PhD thesis: Pulsed EPR Characterization of Membrane Transport Protein Complexes
2004 – 09/2007	M.Sc. in Molecular Biotechnology, Department of Biotechnology, University College of Science, University of Tehran, Iran • Master thesis: "Analysis of the effects of membrane phospholipid composition and dynamics on membrane surface tension and cellular processes". Lab. of Membrane Biophysics, Institute of Biochemistry and Biophysics, University of Tehran • Final grade: *excellent*
2000 – 2004	B.Sc. in Biotechnology, Department of Biotechnology, University College of Science, University of Tehran, Iran
1999 – 2000	Pre-university education, Shahid-Haghani Pre-University Institute, Total GPA: 17.71/20.0.
1996 – 1999	High school, Shahid-Haghani Institute (under the supervision of NODET-National Organization for Developing Exceptional Talents), Total GPA: 19.01/20.0.

ACADEMIC TEACHERS

T. Prisner, B. Bode, C. Glaubitz, R. Tampé, E. Schleiff, L. Forrest, T. Meier, H. Mobasheri, M. N. Sarbolouki, M. Amininasab

PUBLICATIONS

1. **Reza Dastvan**, Bela E. Bode, Karuppiah Muruga Poopathi Raja, Andriy Marko, Sevdalina Lyubenova, Harald Schwalbe, Thomas F. Prisner
"Optimization of transversal relaxation of nitroxides for PELDOR spectroscopy in phospholipid membranes"
The Journal of Physical Chemistry B, 114, 13507–13516 (**2010**)

2. Bela E. Bode, **Reza Dastvan**, Thomas F. Prisner
"Pulsed electron–electron double resonance (PELDOR) distance measurements in detergent micelles"
Journal of Magnetic Resonance, 211, 11–17 (**2011**)

3. Christina Lumme[*], Hasret Altan[*], **Reza Dastvan**[*], Maik S. Sommer, Mislav Oreb, Sevdalina Lyubenova, Björn Hellenkamp, Oliver Mirus, Jens Kretschmer, Wolfgang Kügel, Jan P. Medelnik, Manuela Dehmer, Jens Michaelis, Thomas F. Prisner, Thorsten Hugel, Enrico Schleiff
"Nucleotides and substrates trigger the dynamics of the Toc34 GTPase homodimer"
Manuscript submitted. [*]Equal Contribution.

4. **Reza Dastvan**, Eva-Maria Brouwer, Sevdalina Lyubenova, Oliver Mirus, Maik S. Sommer, Enrico Schleiff, Thomas F. Prisner
"Architecture of the POTRA Domains from Cyanobacterial Omp85 Revealed by Pulsed EPR Spectroscopy"
Manuscript in preparation.

CONFERENCE CONTRIBUTIONS

1. International Symposium on Integrating Advanced Spectroscopic Tools for Structure and Dynamics of Biological Macromolecular Complexes *in vitro* and *in vivo*, Kreuth, Germany, **2012** (Talk & Poster).

2. GDCh FGMR 34th Annual Discussion Meeting, "Advanced Magnetic Resonance for the Study of Dynamics in Biomolecules and Materials", Halle(Saale), Germany, **2012** (Poster).

3. American Biophysical Society 56th Annual Meeting, **2012**, San Diego, US (Poster).

4. EUROMAR **2011**, Frankfurt am Main, Germany (Poster).

5. 44th Annual International Meeting of the ESR Spectroscopy Group of the Royal Society of Chemistry, York, UK, **2011** (Poster).

6. Research in Molecular & Cell Biological Sciences, 2nd Annual TRAM Symposium, Frankfurt am Main, Germany, **2011** (Talk).

7. Research in Molecular and Cell Biological Sciences, 1st Internal Junior Scientists' Symposium, Frankfurt am Main, Germany, **2010** (Poster).

8. 32nd Discussion Meeting and Joint Benelux/German MR Conference, "Development and Application of Modern Techniques in Chemistry, Life Sciences and Material Research", Münster, Germany, **2010** (Poster).

9. Joint Youngster Meeting of the SFB 807 (TRAM) and SFB 35, Transmembrane Transporters in Health and Disease, Vienna, Austria, **2010** (Talk).

10. International Conference on Evolution of Protein Translocation Systems, Frankfurt am Main, Germany, **2010** (Poster).

11. Joint EUROMAR **2010** and 17th ISMAR Conference, Florence, Italy (Poster).

12. 13th European Conference on the Spectroscopy of Biological Molecules (ECSBM) - Palermo, Italy, **2009** (Poster).

13. 10th Symposium on Calcium-Binding Proteins in Normal and Transformed Cells, Leuven, Belgium, **2008** (Poster).

14. Leopoldina Symposium on Lipid Signalling, Frankfurt am Main, Germany, **2008**.

AWARDS AND HONORS

2012	Conference travel award from the "Association of Friends and Supporters of the Goethe University"
2011 – 2012	Member of the guest speaker committee of GRACE-MC
2010	Member of the guest speaker committee of SFB 807
2009	Travel grant from the European Cooperation in Science and Technology (EU COST Action P15 'Advanced Paramagnetic Resonance Methods in Molecular Biophysics')
2009 – 2012	Four travel grants from Hermann Willkomm-Foundation
2007	Achieved an excellent grade for the MSc thesis
2002 – 2007	Ministry of Science, Research and Technology stipend for exceptional talents
2000 – 2007	University of Tehran scholarship for highly-ranked students
1999	National winner of 12th Khwarizmi International Award* (student section) in Tehran, Iran, Feb 1999 by a project entitled: "Effect of

Salinity on Mortality and Survival of the Edible Oyster *Saccostrea cucullata*"

1998   Chosen as the promising youngster of the year by national TV3

1998   Ranked 1st in the international section of the 11th Khwarizmi International Award* (student section) in Tehran, Iran, Feb 1998 by a project entitled: "Studies on the Evolution of the Persian Gulf and Hormozgan Zone Invertebrates"

* The Khwarizmi International Award (KIA) is given annually by the Iranian Research Organization for Science and Technology to individuals who have made outstanding achievements in research, innovation and invention, in fields related to science and technology. The KIA laureates receive their prizes from the hands of the President of the Islamic Republic of Iran. The main sponsors are UNESCO, WIPO (World Intellectual Property Organization), ISESCO, and TWAS.